Doctoral Dissertation

Low-Frequency Noise Analysis of Suspended Graphene Nanoribbon for Gas Molecule Identification

Alexandro de Moraes Nogueira

Supervisor : Hiroshi Mizuta

Graduate School of Advanced Science and Technology
Japan Advanced Institute of Science and Technology
Materials Science

March 2024

Abstract

The human body naturally expels many different gases through respiration and skin. These gases can be monitored and used as a noninvasive diagnosis tool for many diseases. With this application in mind, there have been many studies on high-sensitive gas sensors. Usually, a large number of different compounds have to be monitored at the same time for an accurate diagnosis. In order to achieve this, it is common practice to use an array of different sensors along with machine learning techniques. Another possibility, still not well explored, is to use the electronic noise of only one device to differentiate the compounds.

In this work, the possibility of using the low-frequency noise of suspended graphene nanoribbons (GNR) fabricated through chemical vapor deposition (CVD) for gas identification is explored. Commercially available CVD graphene (Graphenea) on a 300 nm SiO_2 and Si substrate was used. The metal contacts (Cr + Au) were patterned with electron beam lithography and deposited through physical vapor deposition, followed by a lift-off process. The GNR was defined with electron beam lithography, and the graphene was suspended by etching the SiO_2 with buffered hydrofluoric acid (BHF). The noise measurement was performed by monitoring the current of the device using a lock-in technique. Experiments with oxygen show that oxygen causes an increase in the low-frequency noise of the GNR by the appearance of a random telegraph signal (RTS). The RTS observed is anomalous (it only appears at some time periods), with an average dwell time in the high-resistance state of 2.9 ms, and an average dwell time in the low-resistance state of 2 ms for one device with GNR width and length of 200 nm. In another device (same dimensions) it was noticed that the average dwell time increased from around 6 ms to 35 ms during the measurement period. A possible explanation for the observed RTS is that it is caused by oxygen molecules' movements (vibration, rotation, and diffusion) before they can finally find an energetically more stable configuration. Once this configuration is found, the molecules chemisorb on the graphene and the RTS stop.

The initial experiments with oxygen are promising. However, part of the metal contacts is also suspended because the BHF diffuses rapidly under the graphene. As a result, the metal areas that have graphene underneath are also suspended. Two main issues are present because of this. The first one is that there is a higher possibility of device collapse. The second issue is that the RTS may be caused by the adsorption of oxygen on the graphene underneath the contacts. Devices with metal-graphene-metal (MGM) contacts were fabricated to solve these issues. In this new structure, the SiO_2 in the contact region is etched with CF_4 reactive ion etching. Metal was deposited on the open regions,

and only after it, the graphene was transferred to the sample. Therefore, the graphene in the contact region is on a metal layer, avoiding the over-etching under it. The top metal layer is used to ensure good resistance contact and to leave only the channel area exposed.

A new sample was fabricated using the MGM contact structure. 1 nm of tin was deposited in half of the sample's devices to verify if it could act as an adsorption site and increase sensitivity. Experiments with ethanol, acetone, benzene, and oxygen were performed. Changes in the low-frequency noise were observed only for oxygen (appearance of RTS). No conclusive difference was observed between the devices with and without tin. Likely, the tin formed a film covering the graphene (instead of nanoparticles). As a result, the number of adsorption sites (and device sensitivity) could not be increased. Lastly, from the results with oxygen, there is good evidence that the width of the GNR must be considered. Therefore, the effect of gases on the graphene's low-frequency noise may be increased with further device optimization.

Keywords: Suspended graphene, Random telegraph signal, Low-frequency noise, Oxygen adsorption, Gas sensor.

Contents

Publications

Journals:

1. A. De Moraes Nogueira, A. Kareekunnan, M. Akabori, H. Mizuta, and M. Muruganathan, “Anomalous Random Telegraph Signal in Suspended Graphene with Oxygen Adsorption: Implications for Gas Sensing,” *ACS Appl. Nano Mater.*, vol. 6, no. 18, pp. 17140–17148, Sep. 2023, doi: 10.1021/acsanm.3c03348.

2. A. de M. Nogueira *et al.*, “Nonlinearity and temperature dependence of CVD graphene nanoelectromechanical resonator,” *Jpn. J. Appl. Phys.*, Oct. 2023, doi: 10.35848/1347-4065/ad0505.

Conferences:

1. A. de M. Nogueira, S. Enomoto, M. Muruganathan, A. Kareekunnan, M. Akabori, and H. Mizuta, "Nonlinearity and temperature dependence of graphene nanoelectromechanical resonator" in *The 9th International Symposium on Organic and Inorganic Electronic Materials and Related Nanotechnology (EM-NANO)*, Kanazawa, 2023.

2. A. de M. Nogueira, S. Enomoto, M. Muruganathan, A. Kareekunnan, M. Akabori, and H. Mizuta, " Temperature dependence of CVD graphene nanomechanical resonator " in *The 83rd Japan Society of Applied Physics Autumn Meeting (JSAP)*, Sendai, 2022.

3. A. de M. Nogueira, M. Muruganathan, and H. Mizuta, "Windowed histogram for RTS analysis in graphene gaseous sensors" in *The 69th Japan Society of Applied Physics Spring Meeting (JSAP)*, Tokyo - Online, 2022.

Acknowledgements

Firstly, I would like to thank Professor Dr. Hiroshi Mizuta for agreeing to advise me on this project, for his teachings and support. I would also like to thank Dr. Manoharan Muruganathan for his support. I will always be grateful for the many fruitful discussions, teachings, and for his immensurable help in designing experiments and interpreting results. I am also especially grateful to Dr. Sankar Ganesh Ramaraj and Dr. Osazuwa Gabriel Agbonlahor for teaching me how to operate the equipment in the clean room, how to fabricate graphene devices, and how to perform measurements with gas. I am also grateful to Professor Dr. Afsal Kareekunnan for his help on bureaucratic issues, for his hard work in supporting everyone in the laboratory, and for providing advice and discussions related to research and academic life. I would also like to thank Professor Masashi Akabori for his fruitful discussions during the group meetings. Finally, I would like to thank all the integrands (past and present) of the Mizuta laboratory: Mrs. Reiko Seki, Mr. Akira Uchiyama, Dr. Liu Fayong, Dr. Md Zahidul Islam, Dr. Pradeep Kumar Badiya, Dr. Mohammad Razzakul Islam, MSc. Mikiya Ishi, MSc. Shohei Enomoto, MSc. Kota Nakamura, MSc. Shogo Hamasaka, MSc. Guo Jiayu, MSc. Keisuke Emoto, MSc. Teppei Shintaku, MSc. Yoshiki Ozono, MSc. Yoshinobu Kikuchi, MSc. Katsuki Imakita, MSc. Akihiro Kuki, Mr. Jingxuan Xu, Mr. Yuta Onodera, Mr. Liu Yongzheng, Ms. Hu Jiali, Mr, Kaito Honda, and Mr. Kazuaki Yoshino.

Lastly, I would like to thank the Ministry of Ministry of Education, Culture, Sports, Science and Technology (MEXT) from the Government of Japan for financial support through scholarship. Without it, I would not be able to perform this project.

List of Figures

List of Tables

List of Abbreviations

Abbreviation	Description
AC	Alternate current
ADC	Analog-to-Digital Converter
AFM	Atomic Force Microscope
BHF	Buffered Hydrofluoric Acid
BW	Bandwidth
CNP	Charge Neutrality Point
CVD	Chemical Vapor Deposition
CWT	Continuous Wavelet Transform
DIW	Deionized Water
DWT	Discrete Wavelet Transform
EBL	Electron Beam Lithography
E-nose	Electronic nose
FET	Field Effect Transistor
GNR	Graphene nanoribbon
HPF	High-pass Filter
IPA	Isopropyl alcohol
JAIST	Japan Advanced Institute of Science and Technology
LIA	Lock-in Amplifier
LPF	Low-pass Filter
MGM	Metal-Graphene-Metal
MMA	Methyl methacrylate
MOSFET	Metal-Oxide-Semiconductor Field Effect Transistor
PC	Personal Computer
PCA	Principal Component Analysis
PMMA	polymethyl methacrylate
ppb	Parts per billion
ppm	Parts per million
ppt	Parts per trillion
PSD	Power Spectral Density

PVD	Physical Vapor Deposition
RF	Radio Frequency
RIE	Reactive Ion Etching
RMS	Root Mean Square
RPM	Rotations per minute
RTN	Random Telegraph Noise
RTS	Random Telegraph Signal
SCCM	Standard cubic centimeters per minute
SEM	Scanning Electron Microscope
VOCs	Volatile Organic Compounds

List of Symbols

Symbol	Description	Units
$\tilde{v}_d$	Sinusoidal drain voltage	[V]
v_d	RMS value of the sinusoidal drain voltage	[V]
$\bar{x}$	Mean of a probability density function	
$\widehat{\boldsymbol{X}}(f)$	Fourier transform of $\mathbf{X}(t)$	
$\widehat{\boldsymbol{Y}}(f)$	Fourier transform of $\mathbf{Y}(t)$	
μ	Mobility	[$cm^2V^{-1}s^{-1}$]
μ_e	Electron mobility	[$cm^2V^{-1}s^{-1}$]
μ_h	Hole mobility	[$cm^2V^{-1}s^{-1}$]
a	Distance to nearest neighbor	[m]
A	Transimpedance amplifier gain	[V/A]
a_0	Hooge's parameter	[1]
C_G	Gate capacitance	[F/cm^2]
$\mathrm{E}(\boldsymbol{k})$	Energy eigenvalue in the reciprocal space	[eV]
E_F	Fermi energy	[eV]
f	Frequency	[Hz]
F	Cumulative distribution function	
f_c	Characteristic frequency	[Hz]
f_m	Modulation frequency	[Hz]
G	Amplifier gain	
h	Nearest neighbor hopping energy	[eV]
h'	Next nearest-neighbor hopping energy	[eV]
I	Average electrical current	[A]
I_D	DC drain current	[A]
$i_d(t)$	Drain current at time t	[A]
I_{rms}	rms value of the electrical current	[A]
$\boldsymbol{k}$	Momentum vector in the reciprocal space	[m^{-1}]
k_x	y component of vector $\boldsymbol{k}$	[m^{-1}]
k_y	x component of vector $\boldsymbol{k}$	[m^{-1}]
L	Channel length	[m]

L_{mask}	EBL mask channel length	[m]
n	Charge carrier density	[cm^{-2}]
N	Number of molecules	
n_0	Residual charge carrier density	[cm^{-2}]
$N_{e,h}$	Charge carrier number	[1]
N_s	Number of samples	
n_{tot}	Total charge carrier density	[cm^{-2}]
P	Pressure	[Pa]
p_{2d}	2-dimensional hole density	[cm^{-2}]
P_{down}	Probability that a sample is in the down-state	
$p_{gs}(x)$	Gaussian probability density function	
$p_r(x)$	Probability density function	
$P_r(x)$	Probability	
P_{up}	Probability that a sample is in the up-state	
q	Momentum relative to the Dirac point	[m^{-1}]
R	Resistance	Ω
R_D	Differential Resistance	Ω
s	Wavelet parameter scaling	
$S(f)$	Power Spectral Density	
$S_I(f)$	Current Power Spectral Density	[A^2/Hz]
$S_I(f)/I^2$	Normalized Current Power Spectral Density	[Hz^{-1}]
S_I^0	Power spectral density of the background noise	[A^2/Hz]
S_{Id}	Power Spectral Density of the device alone	[A^2/Hz]
S_k	Log-likelihood ration cumulative sum	
$S_R(f)$	Resistance Power Spectral Density	[$Ω^2$/Hz]
$S_R(f)/R_d^2$	Normalized Resistance Power Spectral Density	[Hz^{-1}]
$S_v(f)$	Voltage Power Spectral Density	[V^2/Hz]
$S_v(f)/V^2$	Normalized Voltage Power Spectral Density	[Hz^{-1}]
t	time	[s]
T	Temperature	[K]
t_{down}	Dwell time in the down state	[s]
T_{hr}	Threshold	
t_{ox}	Isolator thickness	[cm]

T_r	Transfer rate from the LIA to the computer	[Hz]
t_{up}	Dwell time in the up state	[s]
V	Average voltage	[V]
V	Volume	[m^3]
V_D	Drain Voltage	[V]
v_F	Fermi velocity	[m/s]
V_G	Gate voltage	[V]
W	Channel width	[m]
W_{mask}	EBL mask channel width	[m]
$\boldsymbol{X}(t)$	In-phase component	
$\boldsymbol{Y}(t)$	Quadrature component	
ΔI	Current difference between two RTS states	[A]
ε	Dielectric permittivity	[F/cm]
θ	Phase angle	[rad]
ρ	resistivity	[kΩ/□]
$\sigma(t)$	Time-dependent electrical conductance	[S]
σ_{std}	Standard deviation	
τ	Wavelet parameter translation	
τ_c	Average dwell for a trap to capture an electron	[s]
τ_{down}	Average dwell time in the down state	[s]
τ_e	Average dwell for a trap to emit an electron	[s]
τ_{up}	Average dwell time in the up state	[s]
$\Phi(f)$	Wiener filter	
$\Psi(t)$	Wavelet mother	
ω	Frequency	[rad/s]
ω_m	Modulation Frequency	[rad/s]
φ	Demodulation phase angle	[rad]

List of Constants

Symbol	Description	Value
e	Elementary charge	1.6×10^{-19} C
i	Imaginary number	$\sqrt{-1}$
k_B	Boltzmann's constant	1.380649×10^{23} J/K
$\hbar$	Reduced Planck's constant	$1.054571817 \times 10^{-34}$ J·s

Chapter 1
Introduction

1.1 Overview of Research

Recently, there has been great interest in research and development of high-sensitive gas sensors for medical diagnostics, agriculture, indoor gas monitoring, *etc*. The human body naturally exhales volatile organic compounds (VOCs) through respiration and skin. Alterations in the composition of these compounds can be used to diagnose many diseases [1]. For example, changes in the concentrations of compounds like acetone, ammonia, and ethanol are linked to gastric cancer, diabetes, liver disorder, mental and physical stress, and kidney diseases [2-6].

The sensitivity necessary for these applications is in the range of parts per billion (ppb) [7]. Thus, there is intense research on developing high-sensitive gas sensors. Graphene is a two-dimensional material made of a sheet of carbon atoms arranged in a hexagonal manner [8]. Because of its electrical and mechanical properties, it has gained a lot of attention since the fabrication of single-layer graphene was demonstrated in 2004 [9].Thanks to its high surface area (2630 m^2/g) and electron mobility (2.5 x 10^5 $cm^2V^{-1}s^{-1}$), graphene is a promising candidate to be used in gas sensing [10]. As a matter of fact, graphene is sensitive enough to detect adsorption/desorption events of single molecules [11] [12].

VOCs exhaled by the human body are a complex mix of many gases. Thus, usually, it isn't enough to monitor just one compound for a precise medical diagnosis [13]. Therefore, an electronic nose (E-nose) capable of differentiating the composition and the proportion of the compounds is necessary. E-noses usually are made from an array of sensors. Each sensor of the array has selectivity to different gases, and the smell patterns can be identified and differentiated with machine learning techniques like principal component analysis (PCA) and neuron networks [14]. Since graphene lacks selectivity, it is common to functionalize it with different materials to obtain selectivity to a specific gas. A compost of graphene and NO nanosheet has demonstrated selectivity towards NO_2 [15]. Graphene-nanopored activated carbon was used for ammonia sensing [16], while carbon molecular sieve/graphene and ZnO/graphene were used for ethanol [17] [18]. Many other examples of graphene-based gas sensors can be found in the literature [19-24].

Another interesting strategy to create an E-nose is to take advantage of changes

in the electronic noise to identify and discriminate different gases/smells. This would be advantageous because a single sensor could be used as an E-nose instead of an array of sensors. A single-sensor E-nose would simplify the fabrication processes and reduce the size and overall cost. It has already demonstrated that the electronic noise spectrum of commercial gas sensors can be used to differentiate the smell of senna tea leaves, potato chips, and white pepper [25]. The low-frequency noise of pristine graphene can be used to differentiate gases like ethanol, methanol, tetrahydrofuran, chloroform, and acetonitrile [26]. Setiad et al. demonstrated that Protoporphyrin, Zn-Protoporphyrin, and Phosphomolybdic acid cause random telegraph signal (RTS) in a carbon nanotube and that it can be used to discriminate these substances [27].

1.2 Motivation and Contribution

To use electronic noise as a tool to identify different substances and eventually use it as a single-device E-nose, the material utilized must be highly sensitive to adsorption of gas molecules. Also, it is of interest that the material has low intrinsic noise. Graphene possesses both characteristics. Rumyantsev et al. used the noise spectrum of exfoliated graphene on SiO_2 substrate to identify some gas vapors [26]. Lorentzian bulges appear on the low-frequency spectrum of the graphene device at a characteristic frequency. The characteristic frequency depends on the gas to which the graphene is being exposed. Therefore, it can be used for gas identification. However, the bulges aren't present for every gas vapor tested, even though resistance changes were observed. Though it was argued that the bulges may be caused by charge traps, the mechanism behind the appearance of the bulges is not well understood yet.

The work by Rumyantsev et al. is an impressive proof of concept. However, they concentrated only on organic vapors, and exfoliated graphene cannot be fabricated on a large scale. To verify if this method is viable for practical applications, it is of interest to investigate if lighter molecules can have a similar effect on graphene obtained by chemical vapor deposition (CVD). In this work, commercially available CVD graphene (Graphenea) was used. Graphene nanoribbons (GNR) were fabricated following a usual top-down lithography process. It is known that CVD graphene is more defective than exfoliated graphene, which increases its intrinsic noise. This issue can be overcome by suspending the GNR since suspended graphene has lower noise than graphene supported on a substrate [28].

Another point is that the bulges in the spectrum can be an indication of RTS. Therefore, it seems advantageous to perform measurements on the time domain. The

frequency response can be analyzed by calculating the spectrum from the measured time series. In this work, measurements in the time domain were performed through an alternate current (AC) lock-in technique [29] [30]. The advantage of this method is that an analysis in both domains could give more information on the physical mechanism. Lastly, the possibility of using tin nanoparticles as adsorption sites to enhance the response of the GNR is investigated.

1.3 Document Organization

This document is organized as follows:

Chapter 1 presents the motivation and background of this work and summarizes the organization of this document.

Chapter 2 gives the background necessary to comprehend the main results of this research. An introduction to the electronic properties of graphene is provided, as well as the main mechanisms used in gas sensors based on graphene. The fundamentals of noise and the physical mechanisms behind electronic noise are presented. A review of the intrinsic noise of graphene is also provided.

Chapter 3 discusses in detail the fabrication process of the suspended GNR. Two different structures were considered: suspended contact structure and metal-graphene-metal structure. Unintentionally, part of the metal contacts is also suspended as an unavoidable consequence of the fabrication process used for the first structure. Since the effect of the suspension of metal contacts is unclear, a second structure, where the metal contacts aren't suspended, was fabricated. Lastly, the measurement setup used to measure low-frequency noise is described.

Chapter 4 describes the effect of oxygen on devices with suspended contacts, where it was noticed that oxygen can cause RTS on suspended graphene.

Chapter 5 presents the results obtained under exposure of suspended graphene (pristine and functionalized with tin) on ethanol, acetone, benzene, and oxygen.

Chapter 6 summarizes the conclusions obtained from this work and outlines possible future works on the subject.

Chapter 2
Research Background

2.1 Basics of Graphene Electronic Transport

The band structure of a single layer of graphite was already studied in 1947 [31]. Each carbon is organized in a hexagonal lattice, and the distance from the three nearest neighbors (a) is 1.42 Å (Figure 2.1). Three of the electrons form strong, hybridized sp^2 bonds (σ-bond). The fourth electron forms the $2p_z$ orbital (π-bonds), perpendicular to the lattice plane. The electron conduction occurs mainly through the π-bond. Considering the π-bond and using a tight-binding model, the eigenvalues $E(\boldsymbol{k})$ as a function of the reciprocal space vector ($\boldsymbol{k}$) is given by [8]

$$E_{\pm}(\boldsymbol{k}) = \pm h\sqrt{3 + w(\boldsymbol{k})} - h'w(\boldsymbol{k}), \tag{2.1}$$

$$w(\boldsymbol{k}) = 2\cos\left(\sqrt{3}\,k_y a\right) + 4\cos\left(\frac{\sqrt{3}}{2}\,k_y a\right)\cos\left(\frac{3}{2}\,k_x a\right), \tag{2.2}$$

where h is the nearest hopping energy (~2.8 eV), and h' is the next nearest-neighbor hopping energy. Figure 2.2 shows the electronic dispersion given by Equation 2.1 and Equation 2.2.

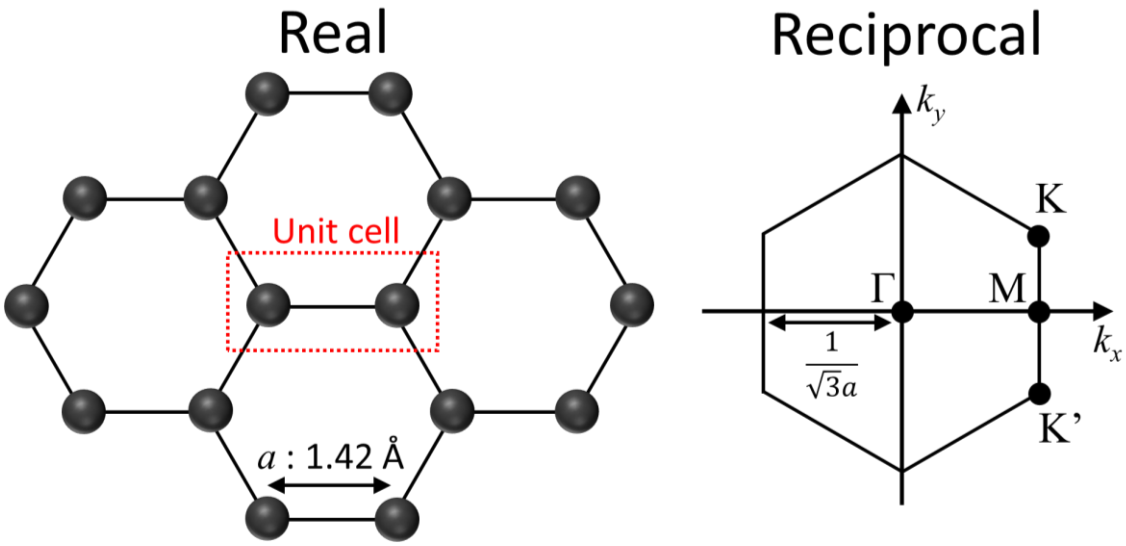

Figure 2.1 Graphene lattice in real and reciprocal spaces.

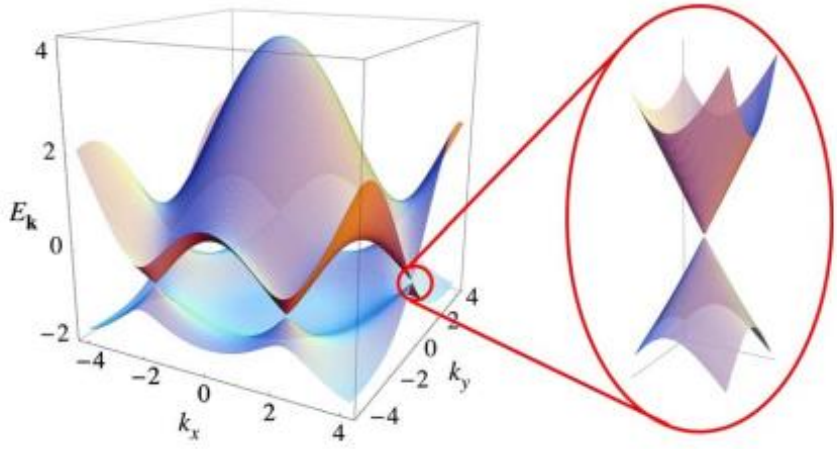

Figure 2.2 Graphene's electronic dispersion [8].

Near the K and K' points (Dirac points) in the reciprocal lattice, the electronic energy dispersion can be approximated by a linear dispersion: $E_{\pm}(\boldsymbol{q}) \approx \pm\hbar v_F|\boldsymbol{q}|$ [32], where $\hbar$ is the reduced Planck's constant (1.0545781 x 10^{-34} J·s), $\boldsymbol{q}$ is the momentum relative to the Dirac points, and v_F is the Fermi velocity of π electrons ($v_F \approx 1$ x 10^6 m/s) [31]. The K and K' points are called Dirac points because the linear dispersion near them is similar to the one obtained from the Dirac equation for relativistic particles. It is interesting to note that graphene has no band gap between the conduction and valence bands. Because of this, graphene is considered a semi-metal.

An important characteristic of graphene is that the charge carrier density (n) can be modulated with gate voltage (V_G). A metal electrode is used to apply a gate voltage to the graphene through an isolator with thickness t_{ox} and dielectric permittivity ε. By doing so the graphene resistance can be modulated. If a drain voltage (V_D) is applied to one of the remaining terminals, the graphene can be used as a field effect transistor (FET). Figure 2.3 shows a schematic of the bias applied in such cases.

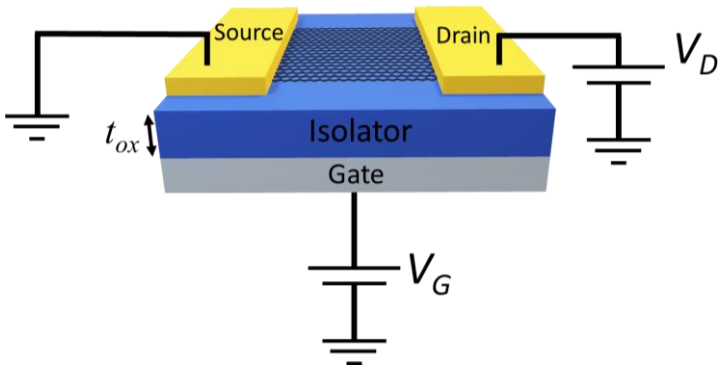

Figure 2.3 Graphene field effect transistor Configuration.

The induced carrier density is given by:

$$n = \frac{C_G V_G}{e}, \tag{2.3}$$

$$C_G = \frac{\varepsilon}{t_{ox}}, \tag{2.4}$$

where C_G is the gate capacitance in F/cm^2, and e is the elementary charge (1.6 x 10^{-16} C). Another important characteristic of graphene is that it can induce electrons and holes, depending on the polarization of V_G. Ideally, at V_G = 0 V, the Fermi energy (E_F) is at the Dirac point, between the valence and conduction bands (at the point of encounter between the upper and lower energy cones). In this situation, the density of holes and electrons are the same, and the transfer characteristic of the graphene FET (drain current (I_D) vs V_G curve) is at its minimum. If positive gate voltage is applied, the E_F moves upwards, and electrons are induced in the graphene channel. As a result, the current increases. If negative gate voltages are applied, holes are induced (E_F moves downwards) and the current increases again. In short, the transfer characteristic presents ambipolar behavior, as illustrated in Figure 2.4

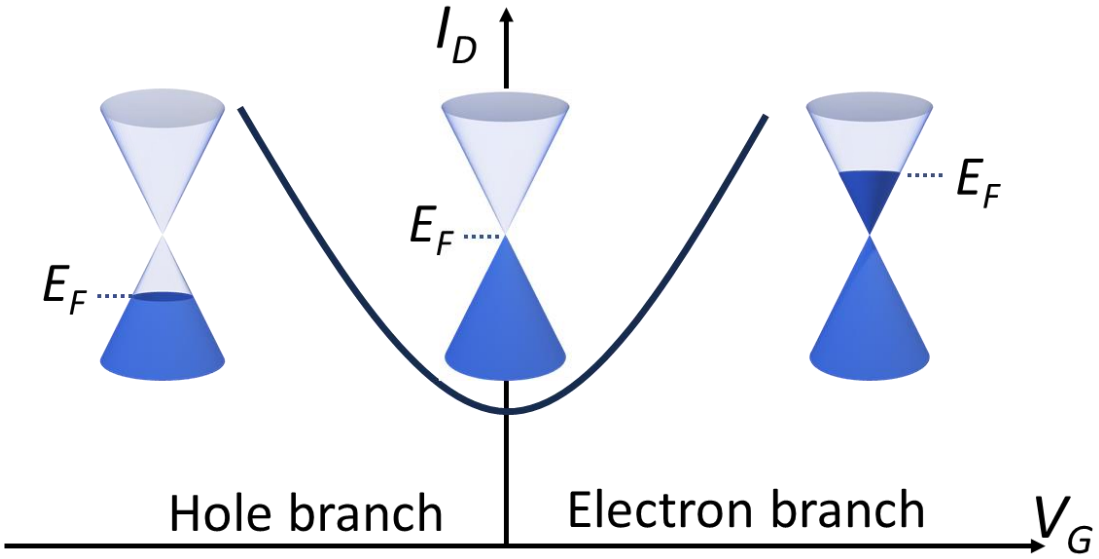

Figure 2.4 Transfer characteristics of undoped Graphene FET, and the energy band diagram illustration on each branch.

Figure 2.4 illustrates a specific situation, where the graphene is not doped by impurities and/or substrate. In real cases, it is very common for graphene to have some doping due to interactions with the substrate, metal contacts, resist leftovers, *etc*. In that case, the minimum of the transfer curve will not be at V_G = 0 V. The gate voltage in which the minimum of the curve happens is an indicator of graphene doping, and it is called the

charge neutrality point (CNP). In the case of n-type doping, there will already be electrons in the conduction band induced by the doping when $V_G = 0$ V. Thus, negative V_G must be applied to reach the CNP. In other words, the CNP shifts to the left of the graph. In a similar way, the CNP shifts to the right in the case of p-type doping (Figure 2.5). Taking this into consideration, the total carrier density (n_{tot}) in the graphene channel can be approximated by [33]:

$$n_{tot} = \sqrt{{n_0}^2 + n(V_G - CNP)^2}, \qquad 2.5$$

where n_0 is the residual carrier concentration at V_G = CNP.

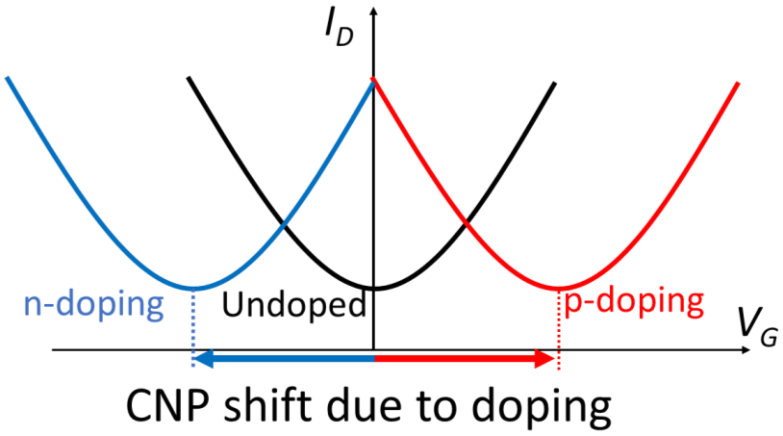

Figure 2.5 Effect of doping on the charge neutrality point of graphene.

2.2 Graphene Gas Sensors

As a two-dimensional material, every effect on graphene can be considered a surface effect. Therefore, it is expected that it will be very sensitive to changes in its environment, which makes graphene a promising material to be used in sensors. The sensing is usually performed by monitoring the graphene current and/or resistance changes under exposition to different gases. Under absorption, there are two main effects from the gas molecules. One is the increase in the Coulomb scattering, which increases the graphene resistance. Single CO_2 molecule physisorption was detected by this method, where it was noted that single adsorption/desorption events increased/decreased the resistance of a GNR by about 60 Ω (Figure 2.6) [12]. Another effect is the doping caused by electron transference to/from the graphene sheet. In that case, the influence on the graphene resistance depends on the intrinsic doping of the device. If the graphene was

originally n-doped and a donor molecule is adsorbed to its surface, the resistance will decrease because there will be more free electrons available for electrical conduction. If an acceptor molecule is adsorbed, there will be fewer electrons, and the resistance will increase. Either way, it is very common to monitor the resistance changes under exposure to the target gas. Figure 2.7 shows the effect of NO_2 at a concentration of 100 particles per million (ppm) on the graphene current [34].

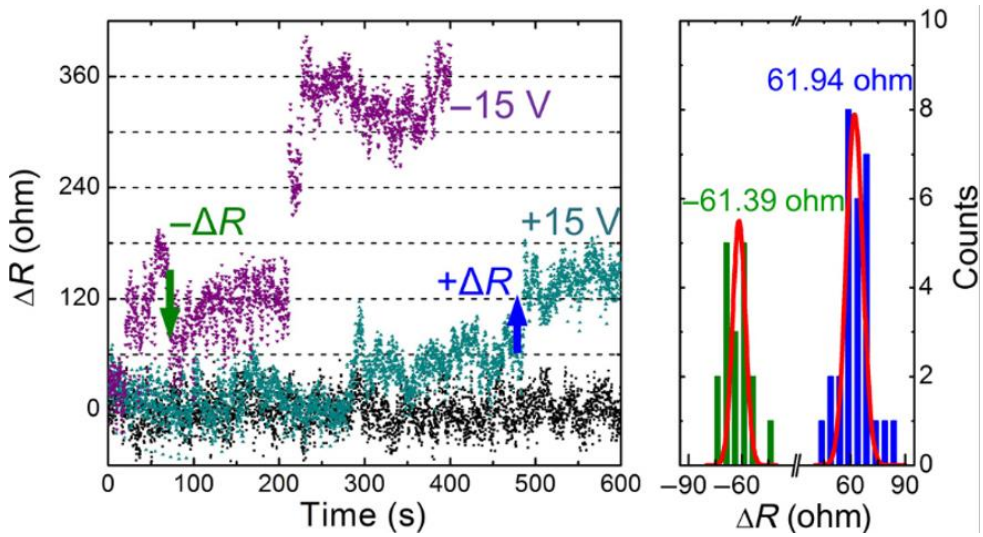

Figure 2.6 Detection of adsorption/desorption of single CO_2 molecule in suspended graphene. Adsorption causes an increase in resistance of around 60 Ω, while desorption causes a reduction of around 60 Ω [12].

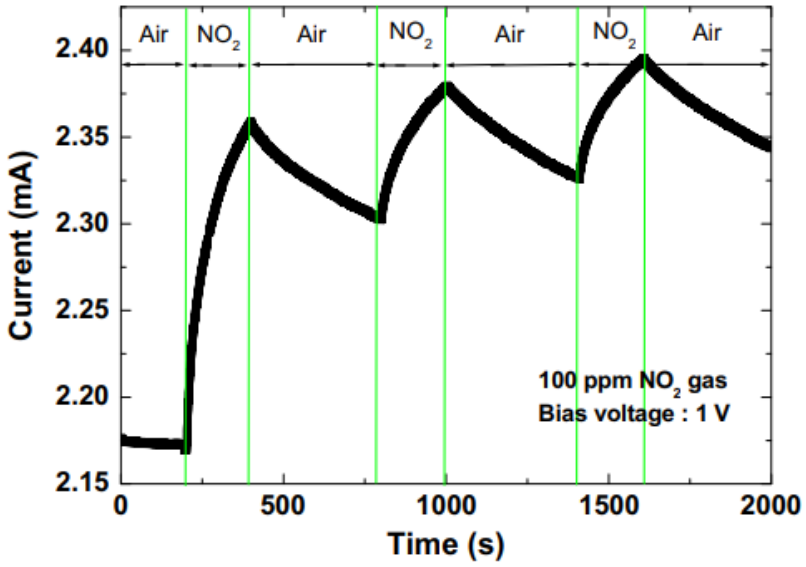

Figure 2.7 Current response of graphene under exposure to 100 ppm NO_2 gas [34].

A disadvantage of graphene is that it is still difficult to control the doping level during fabrication. The substrate, left-over lithography resist, and humidity influence the doping level of graphene [35] [36]. Under exposition to a gas, the electrical current level of graphene will depend on the Coulomb scattering, and on the intrinsic doping level. Therefore, it is difficult to consistently obtain a relationship between resistance changes and gas concentration for different devices. Especially when the intrinsic doping level can have a large variation from device to device. Another way to use graphene as a gas sensor is to monitor its CNP. As illustrated in Figure 2.5, doping causes a shift in the CNP of the device. If the target gas is a donor, the CNP shift will be negative (graphene will be more n-doped). In the case that the gas is an acceptor, the CNP shift will be positive. By using this method, the sensing of ammonia at 500 parts per trillion (ppt) has been demonstrated (Figure 2.8) [16].

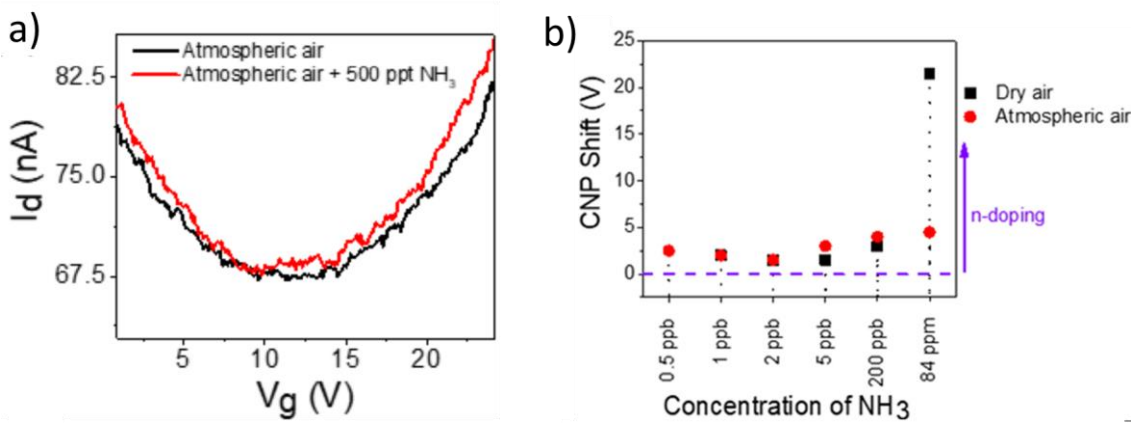

Figure 2.8 Graphene-based sensor for ammonia. (a) Transfer characteristics at atmospheric air and at 500 ppt of NH_3 diluted in atmospheric air. (b) CNP shift at different NH_3 concentrations [16].

Another disadvantage of graphene is its lack of selectivity. It is difficult to say only from the CNP shift, for example, if a large shift is due to a low concentration of a gas with large doping, or a large concentration of a gas with low doping. NH_3, for example, is a strong donor (charger transfer of 0.018 electrons per molecule), while CO is a weak donor (charger transfer of 0.001 electrons per molecule) [37]. To overcome this issue is very common to functionalize graphene with different materials. In that case, the material used in the functionalization will provide selectivity (possibly through some chemical reaction with the target gas), while the graphene still provides high sensitivity [38]. With an array of sensors with different selectivity, it is possible to correctly identify different gases. Along with CNP shift, other parameters, like electron and hole mobility, can be

extracted and used along with machine learning techniques to discriminate some gases (Figure (2.9)) [39]. Another option that needs more investigation is to use electronic noise as a parameter to sense and identify gas molecules.

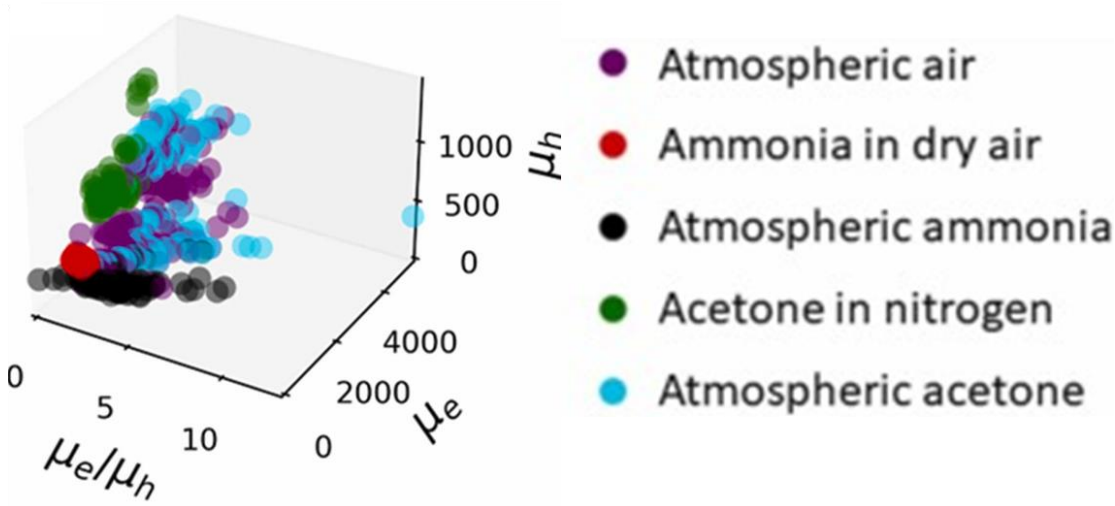

Figure 2.9 3D plot in different gas environments for electron mobility (μ_e), hole mobility (μ_h) and their ratio (μ_e/μ_h). Adapted from [39].

2.3 Basics of Electronic Noise

Noise is caused by random (stochastic) variations and must be analyzed from a statistical point of view. In this section, the basics of mathematics used in noise studies, along with a brief review of the physical origin of electronic noise in solid-state materials are presented.

2.3.1. Mathematical Modeling of Noise

As a stochastic process, noise can be characterized by a probability density function $p_r(x)$. It gives the probability that the outcome of a measurement (denoted here by x) will fall in a determined interval. The probability that a measurement will fall inside an interval between x_1 and x_2 is given by:

$$P_r(x_1 < x \leq x_2) = \int_{x1}^{x2} p_r(x)dx\,. \qquad 2.6$$

In other words, the probability is given by the area under the curve described by $p_r(x)$, limited by the interval ($x1$, $x2$] (Figure 2.10). Naturally, the entire curve area is normalized and equal to 1:

$$\int_{-\infty}^{\infty} p_r(x)dx = 1. \quad 2.7$$

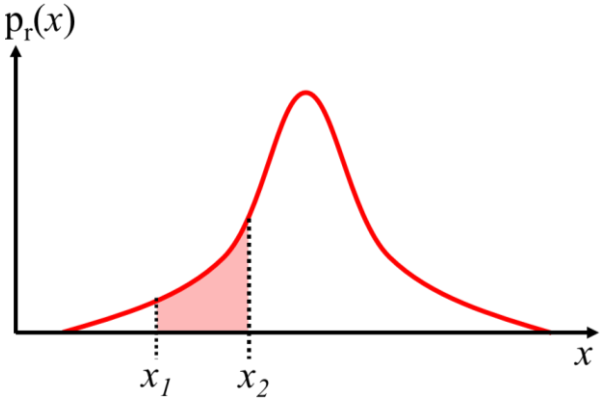

Figure 2.10 Illustration of a probability density function.

Other important parameters are the mean ($\bar{x}$) and the standard deviation (σ_{std}) of the distribution:

$$\bar{x} = \int_{-\infty}^{\infty} x p_r(x)dx, \quad 2.8$$

$$\sigma_{std} = \sqrt{\int_{-\infty}^{\infty} (x-\bar{x})^2 p_r(x)dx}. \quad 2.9$$

A very common distribution is the Gaussian distribution, given by

$$p_{gs}(x) = \frac{1}{\sigma_{std}\sqrt{2\pi}} exp\left[-\frac{1}{2}\left(\frac{x-\bar{x}}{\sigma_{std}}\right)^2\right]. \quad 2.10$$

This distribution is important because the fluctuations caused by a large number of random events (like the thermal noise of solid-state materials) tend to have a Gaussian distribution.

Often, it is useful to obtain the frequency spectrum of the noise. The noise is random; therefore, it will have different values for different times. However, given that the signal is ergodic (a process where the statistics don't change with the time and can be determined from a single sample), the spectrum of any sample will be the same [40].

Usually, the power of the noise under a determined band is the main figure of interest, and the power spectral density (PSD) is used to calculate it. Be *f*, the frequency in Hz, and a function $\xi(t)$, where *t* is the time, the Fourier transform is given by

$$\hat{\xi}(f) = \mathcal{F}[\xi(t)] = \int_{-\infty}^{\infty} \xi(t) e^{-i2\pi f t} dt, \tag{2.11}$$

and the inverse transform is

$$\xi(t) = \mathcal{F}^{-1}\left[\hat{\xi}(f)\right] = \int_{-\infty}^{\infty} \hat{\xi}(f) e^{i2\pi f t} df. \tag{2.12}$$

From the Parseval's theorem we have that the Fourier transform of the energy of the signal in an interval [0.T] is given by [41]

$$\int_0^T |\xi(t)|^2 dt = \int_{-\infty}^{\infty} \left|\hat{\xi}(T,f)\right|^2 df. \tag{2.13}$$

Scaling both sides by *T* results in the power of the signal, that is given by

$$\frac{1}{T}\int_0^T |\xi(t)|^2 dt = \int_{-\infty}^{\infty} \frac{\left|\hat{\xi}(T,f)\right|^2}{\mathrm{T}} df = \int_{-\infty}^{\infty} S(T,f) df, \tag{2.14}$$

where $S(T,f)$ is the power spectral density function, and is given by:

$$S(T,f) = \frac{\left|\hat{\xi}(T,f)\right|^2}{\mathrm{T}}. \tag{2.15}$$

It can be noticed from Equation 2.14 that by integrating the $S(T,f)$ in a certain frequency band, the power in that band is obtained. By integrating $S(T, f)$ for all frequencies, the total power of the signal is obtained.

Usually, colors are used as an analogy to describe the noise's frequency content. A PSD with a constant value, for example, is usually called white noise. A parallel to the white light, that has all the colors. Other examples of colored noise and their frequency content are shown in Table [42]. In this work, the main object of study was the $1/f$ noise (pink noise).

Color	Frequency content
Purple	f^2
Blue	f
White	1
Pink	$1/f$
Red/Brown	$1/f^2$

Table 2.1 Colored noise and their frequency content [42].

2.3.2. Electronic Noise in Solid State Materials

Electronic noise can be divided into two main categories: intrinsic and extrinsic [43]. Extrinsic noise is caused by the influence of electromagnetic waves, mechanical vibration, electromagnetic fields emitted by motors and transformers, *etc*. Intrinsic noise (focus of this work) is generated inside the devices and is caused by the random variations of charge carriers.

One kind of noise present in any conductor is the thermal noise, also known as Johnson-Nyquist [44] [45]. It originates from the thermal random movement of electrons and has a Gaussian distribution. The voltage PSD ($S_v(f)$) in this case is constant for all frequencies and is given by $4k_BTR$, where k_B is the Boltzmann's constant (1.380649 x 10^{-23} J/K), T is the temperature in Kelvin, and R is the resistance of the conductor.

Another type of noise that presents a constant PSD is the shot noise. It originates from the random passage of electrons over a potential barrier [46]. The current PSD (S_I) in this case is given by

$$S_I(f) = 2eI_{DC}, \tag{2.16}$$

where I_{DC} is the mean of the current, and e is the elementary charge (1.6 x 10^{-19} C).

Besides the white noise described above, semiconductors, metals, and resistors usually present low-frequency noise with a $1/f$ spectrum. The origin of the $1/f$ noise was and is the subject of much debate, and different systems have different causes. Hooge uses a semi-empirical model based on mobility fluctuations to describe the $1/f$ noise [47]. Be μ the mobility, a_0 the Hooge's parameter, and $N_{e,h}$ the number of charge carriers, the PSD is modeled as

$$S(f) = \frac{\mu^2 a_0}{f N_{e,h}}. \tag{2.17}$$

In the case of semiconductors, McWhorter showed that $1/f$ spectrum in semiconductors can be caused by trapping/de-trapping of charge carriers [48]. Given that $1/\tau_e$ is the probability per unit of time that an electron will be emitted from a trap, and that $1/\tau_c$ is the probability that the electron will be captured. The capture and emission of one electron by one trap is a two-state Markov process with a PSD given by

$$S(f) = \frac{1}{\tau_e + \tau_c} \frac{4}{\left(\frac{1}{\tau_e} + \frac{1}{\tau_c}\right)^2 + (2\pi f)^2}. \qquad 2.18$$

The PSD of equation 2.18 has a Lorentzian form and follows a f^{-2} behavior, not the $1/f$ that is more commonly observed. For many individual traps, McWhorter showed that if the traps have a $1/\tau_c$ distribution, and that τ_e and τ_c are inversely proportional to the effective capture cross-section, the $1/f$ spectrum is the result of the summation of each trap's contribution, as schematically shown in Figure 2.11 (axes in logarithmic scale).

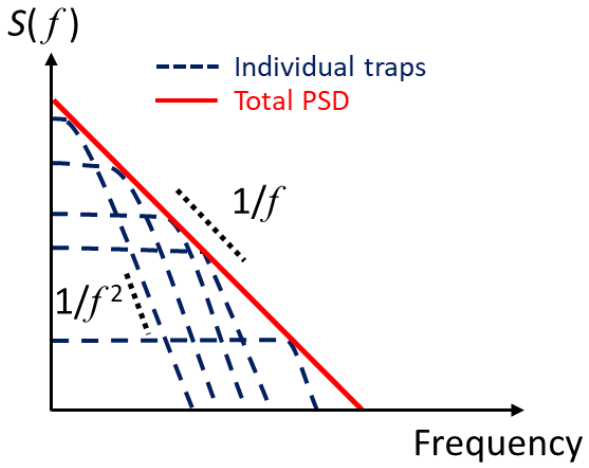

Figure 2.11 Illustration of $1/f$ noise originated from the sum of PSD of a trap distribution.

It is important to note that the origin of $1/f$ noise will depend on the material and device, and there isn't a single general theory for every situation.

Another type of noise of interest is the random telegraph signal (RTS), also called random telegraph noise (RTN), popcorn noise, or burst noise. It is characterized by random changes of current between two or more well-defined states, and usually, it is attributed to the trapping/de-trapping of carriers. As the transistors' size reduced, the total number of charge carriers involved in the flow of electrical current also reduced. As a result, trapping/de-trapping of just one or a few carriers has a large effect on the total

electrical current. In metal-oxide-semiconductor field effect transistors (MOSFET) specifically, the study of RTS and low-frequency noise is of great interest, because it can be used to investigate the oxide quality by determining the traps density and their energy levels [49]. Figure 2.12 shows an example of drain current variations in a MOSFET with a channel width of 1.2 μm, and a channel length of 0.35 μm [50].

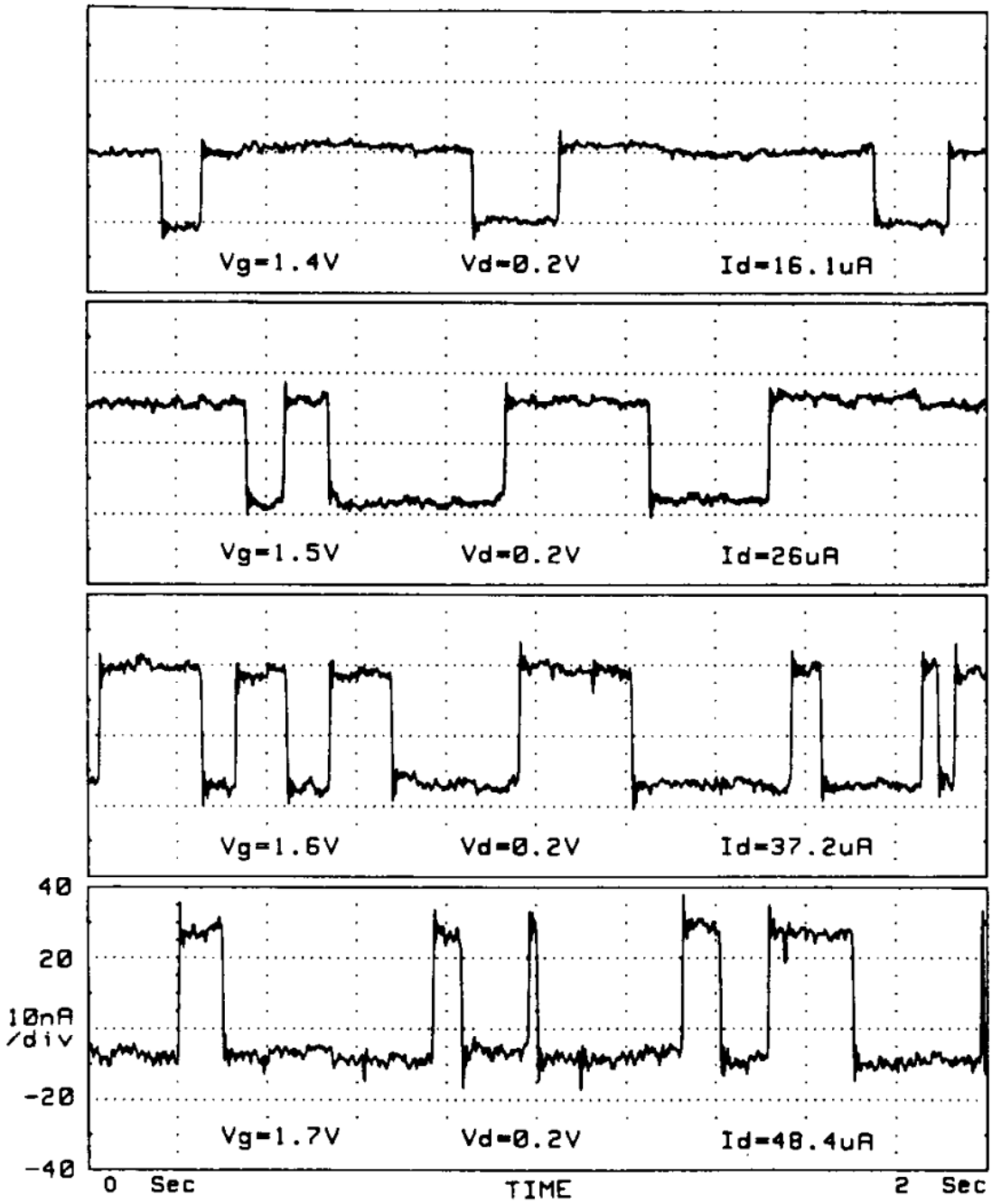

Figure 2.12 Random telegraph signal in a MOSFET for different gate voltages [50].

A two-state RTS is characterized by the dwell time in each state. Be the state with a higher value (electrical current or resistance, for example) the "up state", and the state with a lower value, the "down state", t_{up} is the dwell time in the up state before a transition, t_{down} is the dwell time in the down state, and ΔI is the difference between the two states, as illustrated in Figure 2.13.

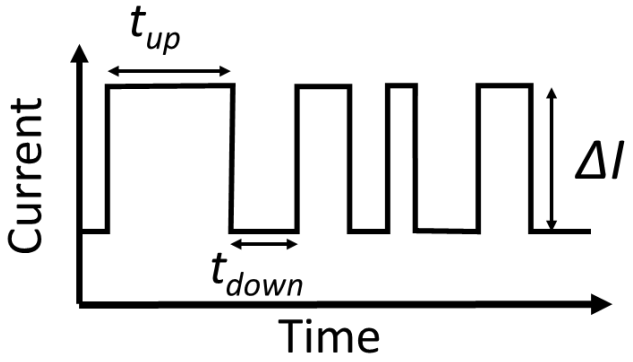

Figure 2.13 Illustration of a RTS, showing the dwell time in the up state (t_{up}) and in the down-state (t_{down}).

As the name implies, the transitions to each state in an RTS occur at random times. Therefore, the dwell times are also random. However, modeling of the RTS can be done by considering $1/\tau_{up}$ as the probability per unit of time that the system will change from the up state to the down state, and $1/\tau_{down}$ as the probability per unit of time that the system will go from the down state to the up state. In that case, t_{up} and t_{down} have the following probability distributions [51]:

$$\mathrm{p_r}(t_{up}) = \frac{1}{\tau_{up}} exp\left(-\frac{t_{up}}{\tau_{up}}\right), \tag{2.19}$$

$$\mathrm{p_r}(t_{down}) = \frac{1}{\tau_{down}} exp\left(-\frac{t_{down}}{\tau_{down}}\right). \tag{2.20}$$

Equation 2.19 and Equation 2.20 show that t_{up} and t_{down} are exponentially distributed, with mean and standard deviation equal to τ_{up} and τ_{down}, respectively. The cumulative distribution function (F) of the t_{up} distribution shown in Equation 2.19 is given by $F = 1 - \exp(-t_{up}/\tau_{up})$. By rewriting it as $-\ln(1-F) = t_{up}/\tau_{up}$, and plotting it as a function of t_{up}, the slope of the resulting line will be $1/\tau_{up}$. The same can be done for t_{down} by taking $F = 1 - \exp(-t_{down}/\tau_{down})$. Therefore, by plotting $-\ln(1-F)$ of the percentiles of the dwell times, one can estimate the average dwell times from the linear regression and use it to characterize the RTS. It is also a useful test to verify if the measured RTS is a Poisson process.

Naturally, the spectrum of the RTS is also of interest. In an analog way to equation 2.18, the PSD of an RTS is a Lorentzian curve and is given by [51]:

$$S(f) = \frac{1}{\tau_{up} + \tau_{down}} \frac{4(\Delta I)^2}{\left(\frac{1}{\tau_{up}} + \frac{1}{\tau_{down}}\right)^2 + (2\pi f)^2}. \qquad 2.21$$

Usually, along with RTS $1/f$ noise and thermal noise are also present. Since the total PSD will be the result of their superimposition, the RTS shows in the spectrum as a bulge in the background $1/f$ noise at a characteristic frequency f_c as shown in the schematic in Figure 2.14. Also, the characteristic frequency is related to the mean dwell times by

$$2\pi f_c = \frac{1}{\tau_{up}} + \frac{1}{\tau_{down}}. \qquad 2.22$$

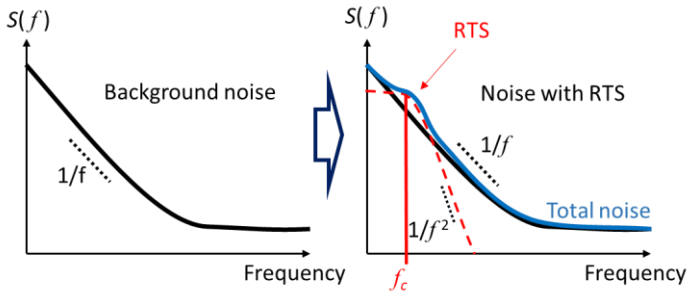

Figure 2.14 Schematic of bulge in the $1/f$ noise caused by the RTS.

To better localize the bulge and determine the characteristic frequency of an RTS, it is common to plot the product of PSD and frequency. In this plot, the $1/f$ becomes a constant line, and the bulge appears as a peak at f_c (Figure 2.15)

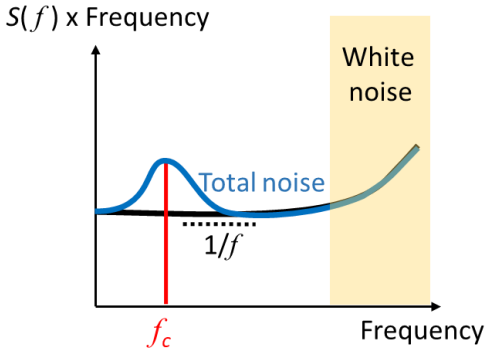

Figure 2.15 Representation of a plot of the product of $S(f)$ by the frequency with a peak due to RTS.

Lastly, it is important to point out that measurement of noise usually is done by measuring the current PSD at a fixed voltage, or the voltage PSD at a fixed electrical current. Given that the noise is caused by the variations in the resistance of the sample, and by following the Kirchhoff law, the PSDs are related in the below manner: [52]

$$\left(\frac{S_I(f)}{I^2}\right)_{V=constant} = \left(\frac{S_V(f)}{V^2}\right)_{I=constant} = \frac{S_R(f)}{{R_d}^2}, \qquad 2.23$$

where I is the average current, V is the average voltage, S_R is the resistance noise PSD, and R_d is the differential resistance. In summary, the normalized PSD is the same regardless of which electrical signal is being measured.

2.4 Low-Frequency Noise in Graphene

It is widely accepted that 1/f noise can have many different origins, depending on the material and the system under study. Since 1/f noise was first demonstrated in graphene in 2008 [53] [54], there have been many studies on this subject. The PSD is proportional to I^2 in graphene, which means that the noise is simply modulated by changes in the graphene conductance [55]. Values for the normalized PSD are usually in the range of 10^{-9} to 10^{-7} Hz^{-1} at 10 Hz [56]. These values are relatively low, making graphene an attractive option to be used in applications where low noise is required.

The gate voltage also influences the noise of graphene. Noises amplitude with a V-shape with the minimum near the Dirac point [57], and M-shape [58] [59] have already been demonstrated (Figure 2.16). With larger V_G, there are more charge carriers. Since the noise amplitude in Hooge's model (mobility variation) is inversely proportional to the number of carriers (Equation 2.17), mobility variations alone cannot explain this behavior. Therefore, it is believed that charge trapping/de-trapping in the substrate interface is responsible for the M and V-shapes [60]. However, by removing the influence of the substrate, there is evidence that the intrinsic 1/f noise of graphene is caused by mobility variations [61] [62].

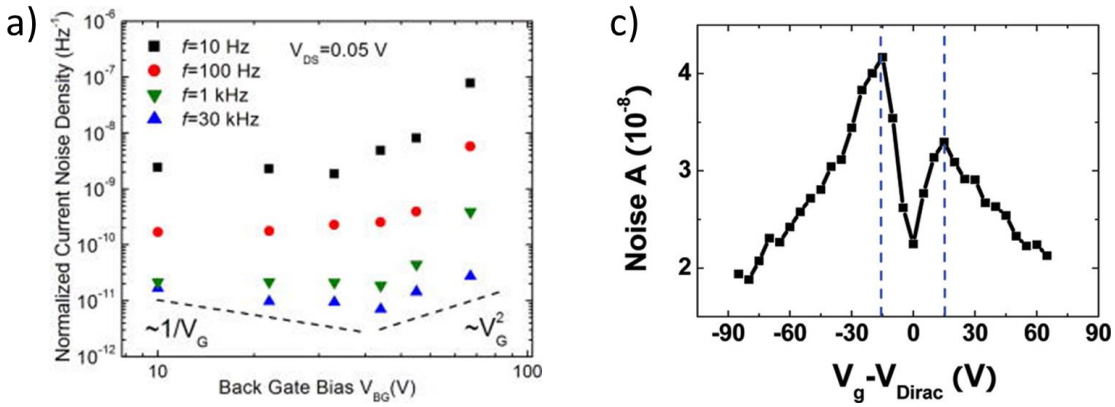

Figure 2.16 Graphene electronic noise dependence on gate voltage. (a) Normalized PSD as function of gate voltage for different frequencies, showing a V-shape [57]. (b) Electrical current noise as a function of the gate voltage, showing a M-shape [58].

While noise is undesirable, it can be useful for some applications. Rumyantsev et al. used the noise spectrum to differentiate some gas vapors [26]. They used exfoliated graphene on a SiO_2 substrate and noticed that a bulge in the PSD appears when exposed to different gas vapors (Figure 2.17). The f_c can be used as an individual signature of each gas vapor, and reproducibility among different devices was demonstrated. Table 2.2 summarizes the relationship between the vapor gas and the f_c obtained in reference [26].

Vapor	f_c **(Hz)**
Ethanol	400-500
Methanol	250-400
Tetrahydrofuran	10-20
Chloroform	7-9 and 1300-1600
acetonitrile	500-700
toluene	NA
Methylene chloride	NA

Table 2.2 Characteristic frequency of supported graphene for different vapors [26].

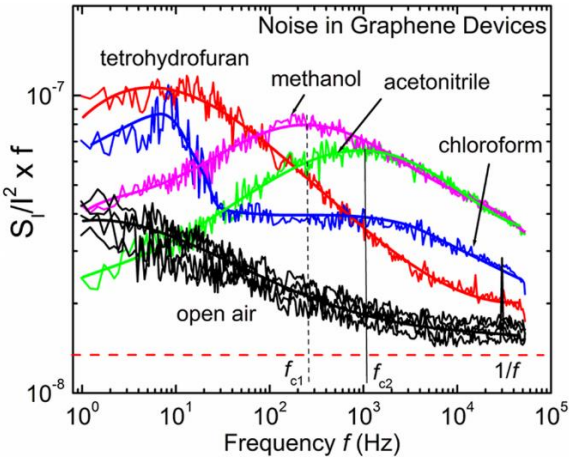

Figure 2.17 Product of the Power Spectral Density and the frequency under exposition to different vapor gases [26].

Noise was also used to study the diffusion of neon atoms on the graphene surface at cryogenic temperatures [63]. It was shown that the at temperatures lower than 10 K, diffusion and clustering of neon atoms are the main responsible for the low-frequency noise in a ultra-clean suspended graphene. Another possible application is to use noise as a parameter to increase the response time of gas sensors. Usually, the recovery time is very long in graphene gas sensors based on resistance changes. However, the response time to the noise caused by the gas is much faster. Therefore, the response time can be vastly improved by using the resistance along with noise as parameters [64] (Figure 2.18).

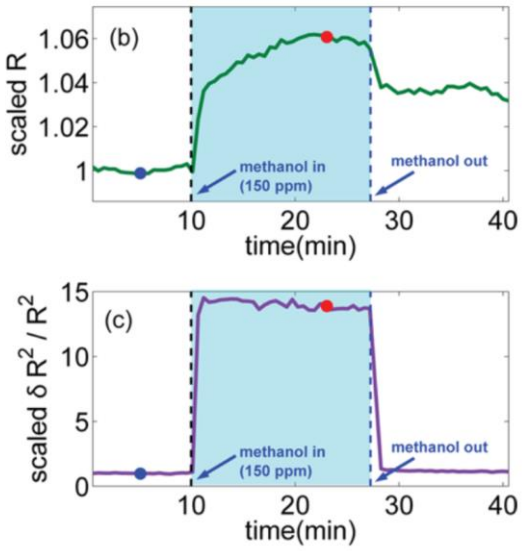

Figure 2.18 Graphene's resistance (R) and relative resistance variance ($\delta R^2/R^2$) response to methanol [64].

Chapter 3
Suspended Graphene Nanoribbon Fabrication and Noise Measurement

3.1 Suspended Metal Contact Structure

Devices with suspended GNR were fabricated in a clean room localized at Japan Advanced Institute of Science and Technology (JAIST) and maintained by the Center for Nanomaterials and Technology. As will be commented on later, besides the GNR, a portion of the metal contacts are also suspended in this first design. The samples were fabricated from 4" wafers obtained from the company Graphenea. The wafer consists of a silicon substrate, a 300 nm thick SiO_2 layer on both sides and a monolayer of CVD graphene on top (Figure 3.1(a)). To cut the wafer into 15 x 20 mm samples, the graphene side was spin-coated with polymethyl methacrylate (PMMA) at 4000 rotations per minute (RPM) for 60 seconds (estimated thickness of 0.18 μm), followed by baking on a hot plate at 180 °C for 5 minutes. The PMMA layer is necessary to protect the graphene during the dicing. The wafer was cut into different samples by the A-WD-10B dicing machine from Tokyo Seimitsu Co., Ltd (Figure 3.1 (b)).

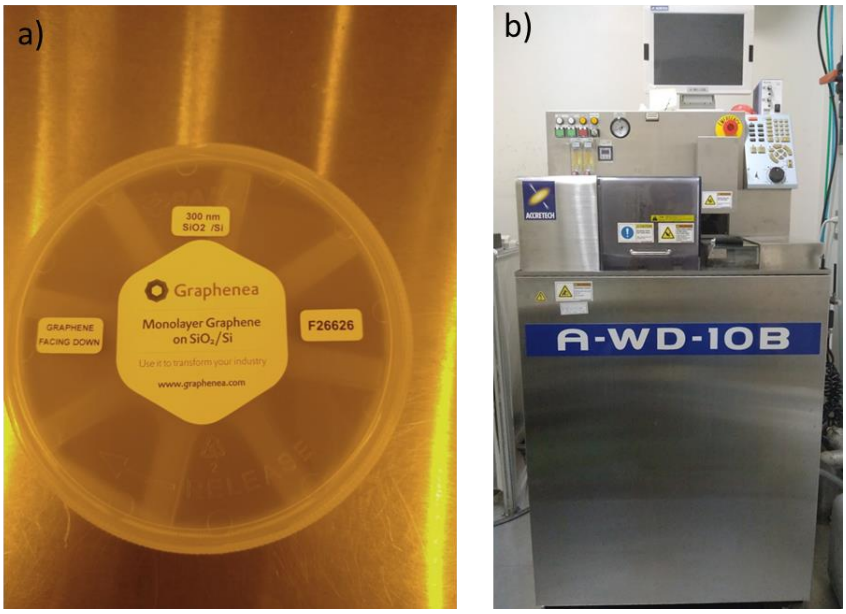

Figure 3.1 a) Picture of monolayer graphene wafer on SiO_2/Si substrate. b) A-WD-10B dicing machine.

Reactive Ion Etching (RIE) with CF_4 gas (Figure 3.2 (a)) was used to etch the backside SiO_2. The etching was performed for 9 minutes at a pressure of 4 Pa, gas flux of 20 standard cubic centimeters per minute (SCCM), and radio frequency (RF) power of 100 W. A picture of the RIE machine is shown in Figure 3.2 (a). After the RIE, the PMMA was removed in hot acetone (60º C) for 30 minutes, followed by rinse in isopropyl alcohol (IPA) for 5 minutes. For further cleaning, the sample was annealed using an infrared furnace (Figure 3.2(b)). The annealing was performed in an $Ar+H_2$ (10%) environment at a flow rate of 0.5 L/min at 300 ºC for three hours.

Figure 3.2 (a) Reactive Ion Etching machine. (b) Infrared furnace used during annealing.

After the annealing, the first electron beam lithography (EBL) was performed. All the EBL steps in this work were performed using an ELS-700 Electron beam lithography system (Elionix) (Figure 3.3). The masks were created using the AutoCAD software from Autodesk. The first EBL was used to define the metal PADs that will be used during the measurements and register markers necessary for alignment in subsequent EBL steps. Figure 3.4(a) shows the marks of the metal PADs and the circular register marks R3. Figure 3.4(b) shows the cross-format register mark R2. R2 is used to align the position and rotation of the entire sample, while the R3 marks are used to align each chip individually. Before each EBL, the sample was cleaned in acetone for 5 minutes, followed by IPA for 5 minutes.

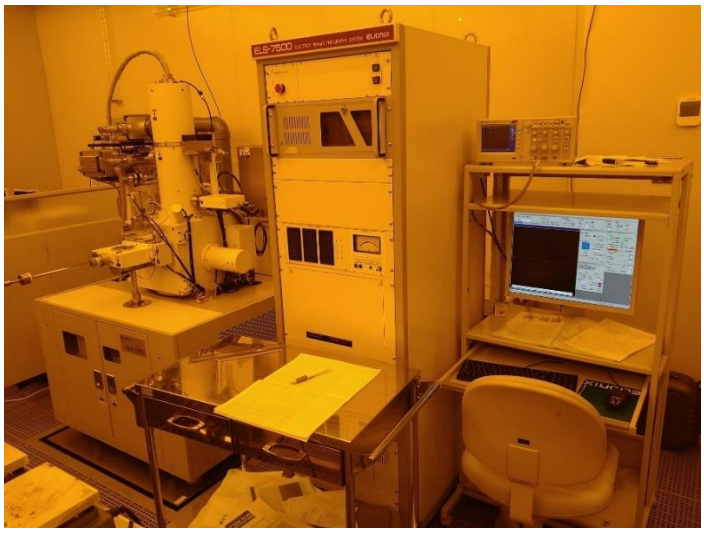

Figure 3.3 ELS-7500 Electron Beam Lithography System (Elionix).

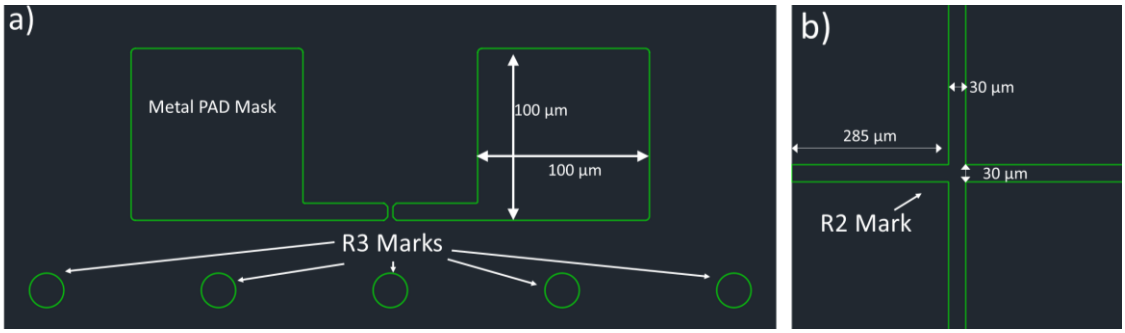

Figure 3.4 AutoCAD masks. (a) Metal PAD and R3 register marks. (b) R2 register marks.

A bilayer of methyl methacrylate (MMA) and PMMA was used as electron-beam resist. The MMA was spin-coated at 2000 RPM for 60 seconds, followed by soft baking in a hot plate for 5 minutes at 180 ºC. The estimated thickness of the resist is around 0.3 µm. Next, the PMMA was spin-coated at 4000 RPM for 60 seconds, followed by baking on a hot plate at 180 ºC for 5 minutes. The PMM layer has an estimated thickness of 0.18 µm. The electron beam current was set to 1 nA, with a dose time of 0.21 µs (dose of 130 $\mu C/cm^2$). The development was performed with MIBK:PIA 1:1 (Kayaku Advanced Materials) for 40 seconds, followed by rinse in IPA for 30 seconds.

Before metal deposition, the exposed graphene was removed using oxygen RIE at a pressure of 4 pa, RF power of 30 W, and a gas flow of 10 SCCM for 10 seconds. The metal was deposited through physical vapor deposition (PVD) using an electron beam thermal evaporator (Figure 3.5). 5 nm thickness of chromium was deposited to ensure adhesion to the SiO_2, followed by 75 nm of gold. The lift-off process was performed in hot acetone (60 ºC) for 30 minutes.

Figure 3.5 Electron beam thermal evaporator used during physical vapor deposition.

The next step was to define the metal contacts with graphene. Instead of MMA and/or PMMA, AR-P 6200.09 resist was used to obtain better resolution. The sample was spin-coated with the electron beam resist at 4000 rpm for 60 seconds, followed by soft-bake at 150 ºC for 1 minute. The final resist thickness is estimated to be 0.3 µm. The EBL was performed with an electrical current of 250 pA and dose time of 0.52 µs per dot (total dose of 130 µC/cm^2). The development was performed with developer AR 600-546. 5 nm of chromium, followed by 25 nm of gold were deposited by electron beam PVD. The lift-off process was performed with the remover AR 600-71 at 80 ºC for 5 minutes. A screenshot of the metal contact mask of one of the devices is shown in Figure 3.6

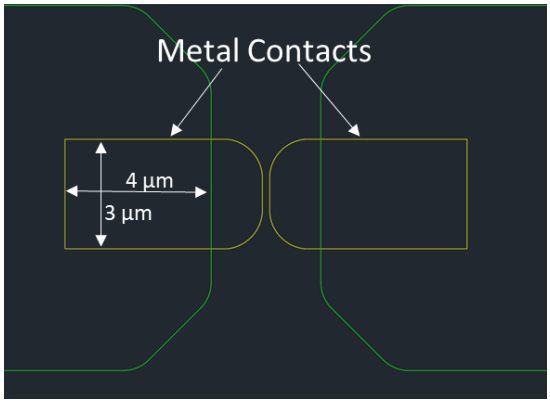

Figure 3.6 Metal contacts mask shown in yellow.

A bilayer of PMMA and negative electron-beam resist AR-N 7520.07 was used to define the nanoribbon regions. The function of the negative resist is to protect the graphene in the desired area, while the unprotected graphene will be removed through RIE. The function of PMMA is to facilitate the lift-off process since it is much easier to remove PMMA with acetone than to remove the AR-N resist with the AR 300-76 remover. The sample was spin-coated with PMMA at 4000 rpm for 60 seconds and baked on a hot plate for 5 minutes at a temperature of 150 ºC. AR-N 7520.07 was spin-coated at 4000 rpm for 60 seconds and baked at 85 ºC for one minute. The EBL was performed with an electron beam current of 250 pA and a dose time of 0.4 µs. The AR resist was developed with developer AR 300-47 (50 seconds), followed by rinse in deionized water (DIW) for 30 seconds. After development, the sample was baked once more on a hot plate at 85ºC for 1 minute to increase the resistance of the AR-N 7520.07 to RIE. Figure 3.7 shows the screenshot of the GNR mask (magenta rectangle).

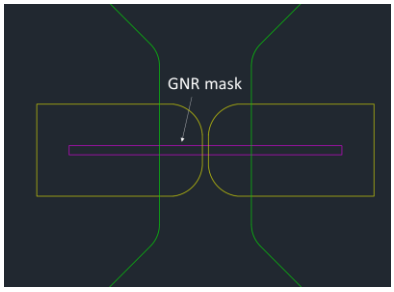

Figure 3.7 GNR mask of a device with 300 nm width and 200 nm length.

Finally, oxygen RIE (gas flow of 10 SCCM, pressure of 4 Pa, and RF power of 35 W) was performed for 2 minutes and 20 seconds to remove the exposed PMMA and the graphene under it, while the graphene remains in the regions where the AR resist is present. The sample was cleaned by annealing it in an Ar+H_2 environment at 300 ºC for three hours.

The GNR was suspended by etching the SiO_2 in buffered hydrofluoric acid (BHF) for 45 seconds, followed by rinsing in DIW for 20 seconds three times (Figure 3.8(a)). Approximately 70 nm of SiO_2 were etched at an estimated rate of 90 nm/min. After dipping in DIW, the sample is kept in IPA. Finally, supercritical drying is performed with CO_2 gas at a pressure of 14 MPa for 50 minutes with the desktop type supercritical rinser and dryer SCRD 4 (Figure 3.8 (b)). A simplified schematic of the entire fabrication process is shown in Figure 3.9. A Runsheet with the summarized fabrication steps and parameters is present in Appendix A.

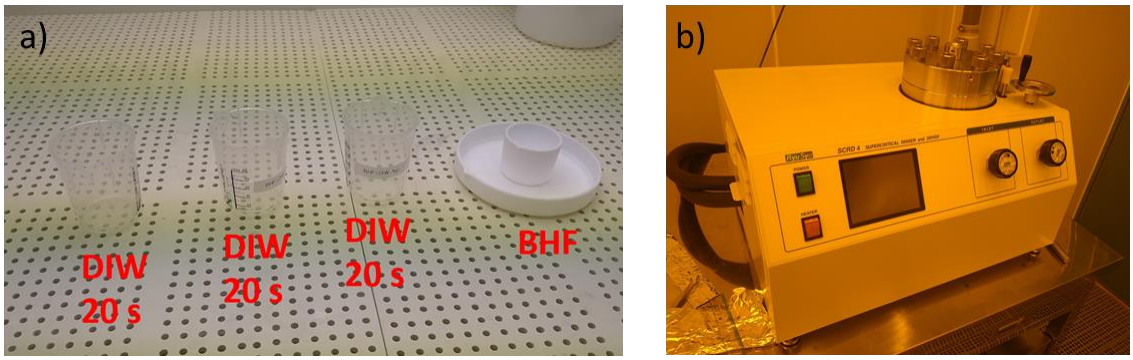

Figure 3.8 GNR suspension. a) set-up for wet etching of SiO_2 with BHF. b) Supercritical rinser and dryer SCRD 4.

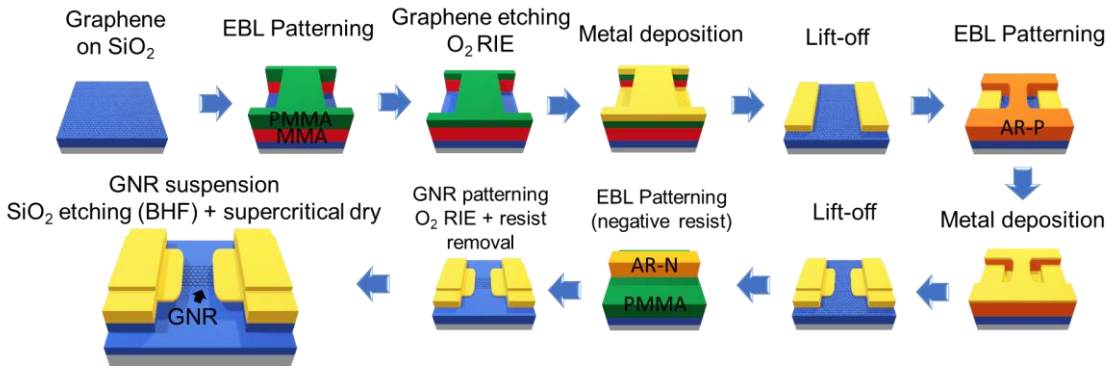

Figure 3.9 Schematic of the fabrication process of suspended graphene with suspended contacts.

Figure 3.10(a) shows the scanning electron microscope (SEM) image of a suspended GNR with channel width (W) and channel length (L) equal to 200 nm successfully fabricated by this method. It is important to notice that the metal contacts are also suspended, as indicated in Figure 3.10(b). This happens because the BHF can diffuse very quickly underneath the graphene [65], and the SiO_2 of regions where the metal is on top of the graphene is also etched. Consequently, many devices collapsed on the substrate (Figure 3.10(c)). These devices are still working; however, they are not suspended anymore and weren't used in this study. In the devices that remained suspended, the graphene underneath the metal contacts is exposed, and the gas molecules can adsorb on these regions. Therefore, it is not clear if any effect on the device's resistance is caused by adsorption on the channel or on the contact region. To solve this problem, a new design was considered, and samples with a metal-graphene-metal (MGM) contact structure were fabricated.

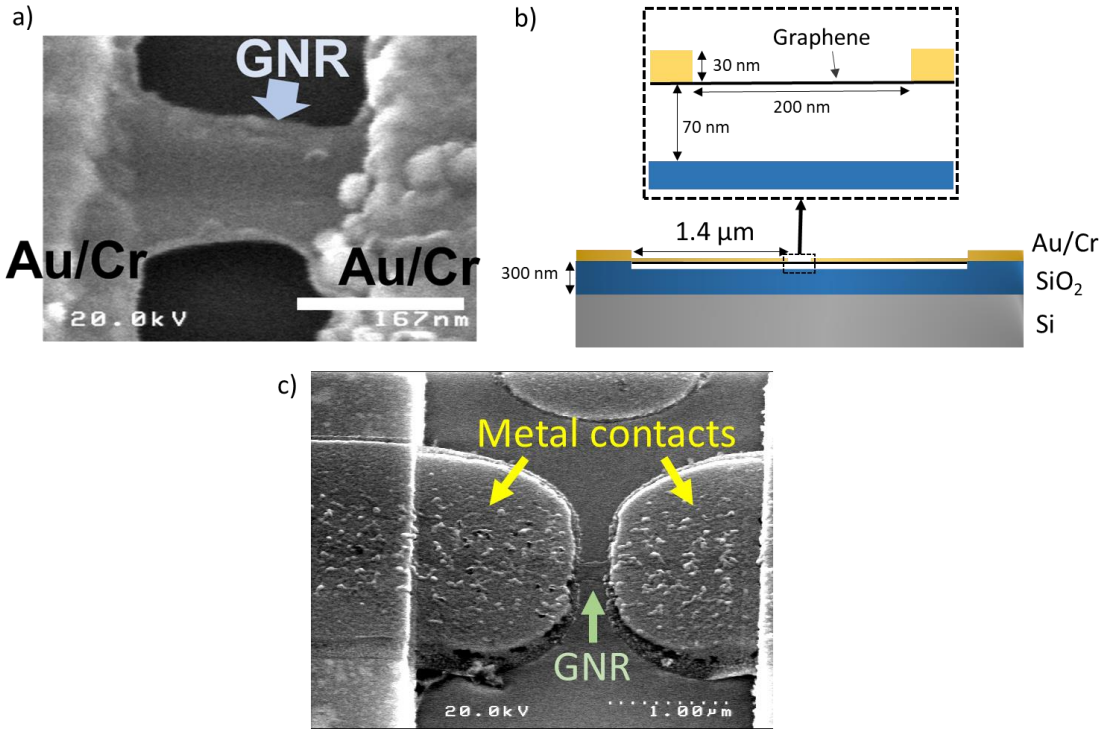

Figure 3.10 a) Scanning Electron Microscope of one of the devices ($W = L = 200$ nm). b) Cross-section schematic in scale of a device with $W = L = 200$ nm. c) SEM image of a collapsed device.

3.2 Metal-Graphene-Metal Contacts Structure

To avoid the suspension of metal contacts, devices with a new structure were fabricated. In this new design, the GNR contacts will have a bottom layer of metal, a layer of graphene, and another layer of metal on top, forming a metal-graphene-metal contact structure. The metal below the graphene will avoid over-etching by the BHF, while the metal above the graphene will ensure that any observed effect will be in the graphene channel. Also, tin was deposited in some devices of the final sample to verify if nanoparticles can act as adsorption sites and enhance the effect of gas on the electronic noise.

In this process, a 4" Si wafer with 300 nm of SiO_2 was used (no graphene on it). The dicing was performed the same way as it was done with the samples with suspended contact. The bottom oxide was etched with CF_4 RIE, at a gas flow of 20 SCCM, a pressure of 4 Pa, and an RF power of 100 W for 9 minutes. Since there is no graphene on the sample yet, piranha cleaning was used to remove any organic contaminants from the substrate. 50 ml of H_2O_2 was poured into a beaker and mixed with 50 ml of H_2SO_4. After

waiting for 3 minutes for the solution reaction to stabilize, the samples were rinsed in the piranha solution for 15 minutes. After the cleaning, the samples were moved to a beaker with DIW (two times) and dried with a nitrogen air gun.

After the piranha cleaning, the first EBL step was performed. It is important to highlight that the first metal layer must be entrenched in the SiO_2 substrate. This is necessary to avoid etching the oxide below the metal. Therefore, after EBL the exposed SiO_2 area must be etched before the metal deposition and the resist used must be thick enough to not be completely etched away. Another point is that the metal PADs, register marks, and contacts are patterned at the same time, thus the resist AR-P was chosen. The SiO_4 is etched with CF_4 RIE, at a flow of 20 SCCM, pressure of 4 Pa, and an RF power of 100 W for 96 seconds, resulting in the etching of 80 nm of SiO_2. In the datasheet of AR-P 6200.09, it is stated that the CF_4 plasma etching rate at 5 Pa is 45 nm/min. Since the estimated thickness of the resist at 4000 RPM is 200 nm, only one layer could be enough since the total etching during the 96 seconds would be 72 nm. However, our RIE setup is not the same as the one used by the company to create the datasheet, and there might be some thickness variation in the sample. Therefore, two sample tests were prepared to verify if the AR-P thickness is enough.

To save time, only four devices were patterned in both sample tests. The first sample test was spin-coated with AR-P 6200.09 at 4000 RPM for 60 seconds and baked on a hot plate at 150 ºC for 1 minute. The second sample test was spin-coated two times with AR-P with the same parameters, with 1 minute of cooling at room temperature between each coating. Both samples-test were patterned with EBL at an electric current of 250 pA and dose time of 0.52 μS. The samples were developed with Developer AR 600-546 developer for 90 seconds, followed by dipping in the stopper AR 600-60 for 30 seconds and DIW for 30 seconds. Post-baking on a hot plate was performed at 130 ºC to increase resistance to RIE. The oxide etching was done with CF_4 RIE for 96 seconds, and the metal was deposited with electron beam PVD. 5 nm of chromium at a rate of 1 Å/s was deposited, followed by 75 nm of gold at an average of 2.5 Å/s. The lift-off was performed with remover AR 600-71 at 80 ºC for 5 minutes. The lift-off wasn't successful in the case of the first sample test (Figure 3.11(a)). For the second sample test, the entire process was a success (Figure 3.11(b)), and the SEM image confirms that there wasn't considerable overdevelopment, with a gap of approximately 180 nm between the two metal layers (Figure 3.11(c)).

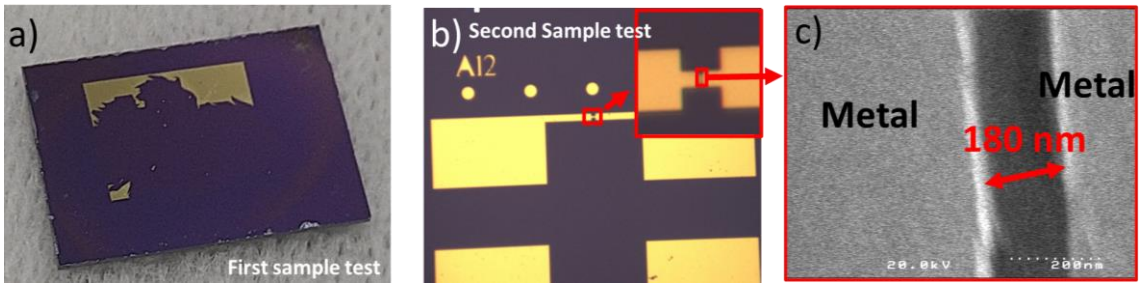

Figure 3.11 Sample tests' results. a) First sample test showing that the lift-off wasn't successful. b) Optical microscope picture of the second sample showing that the lift-off process was a success. c) SEM image of the second sample showing the two metal contacts, separated by a gap of 180 nm.

Figure 3.12 shows the Atomic Force Microscope (AFM) image of the second sample test. It shows that in reality, the metal layer is 10 nm above the SiO_2. It also shows that there is some roughness in the metal with variations of around 5 nm. It is important to point out that the main objective of this sample was to verify if the etching followed by metal deposition would be successful. In the main sample, a lower metal deposition rate (maximum of 2 Å/s) was used, and the thickness deposited was more carefully controlled, such that Figure 3.12 can be taken as a worst-case scenario.

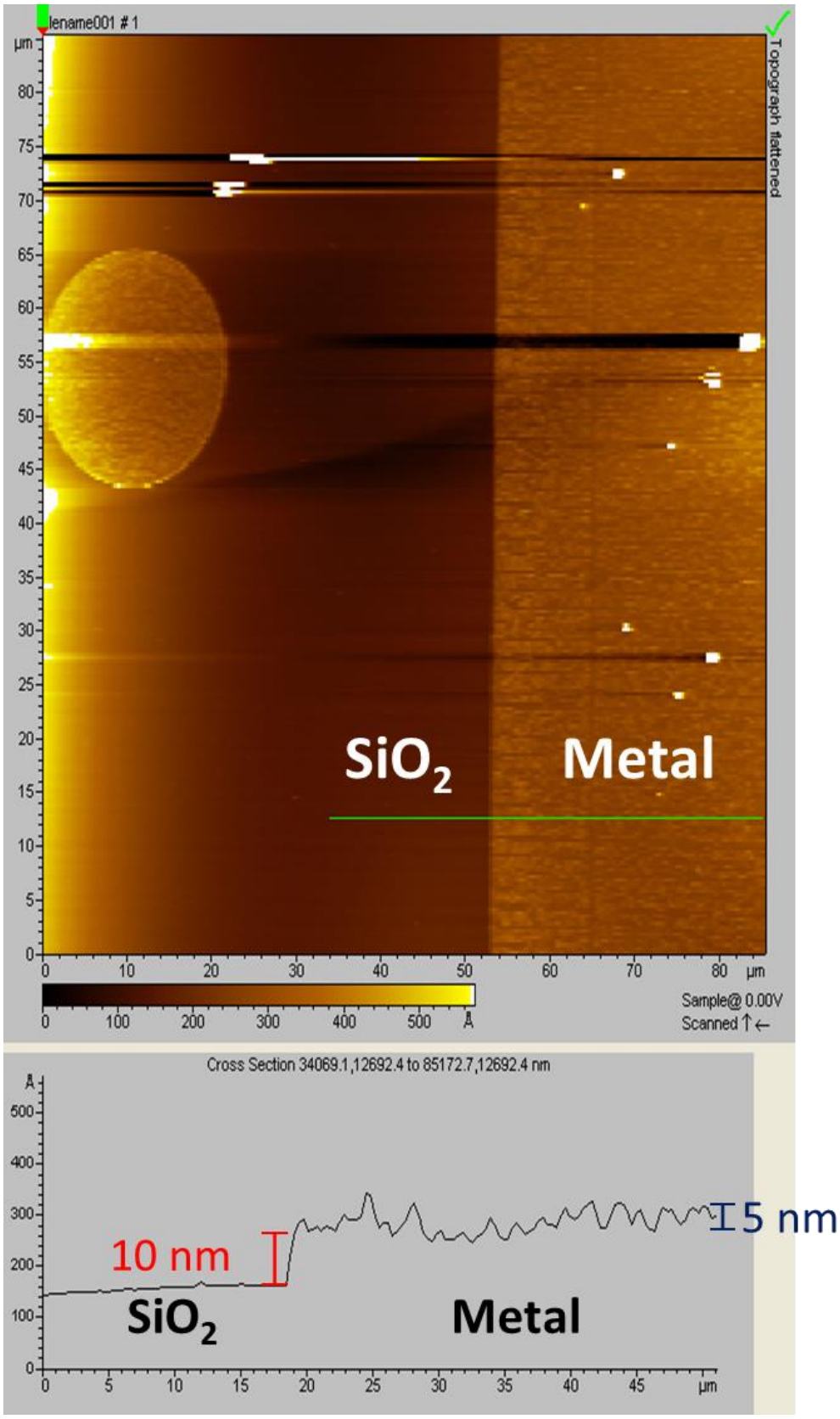

Figure 3.12 Atomic force microscope image of the second sample test.

Since the first sample test showed problems during the lift-off process, the recipe of the second sample test 2 was used during the fabrication of the main sample. Thus, AR-P was spin-coated twice, and all the EBL parameters, CF_4 RIE, and metal deposition are the same as commented previously. O_2 RIE was used to remove any AR-P leftover (10 SCCM, 4 Pa, 30 W, 25 seconds) after the lift-off process. Figure 3.13 shows optical microscope images of the sample just after EBL (Figure 3.13(a)), after CF_4 RIE (Figure 3.13(b)), and after the lift-off process (Figure 3.13(c)).

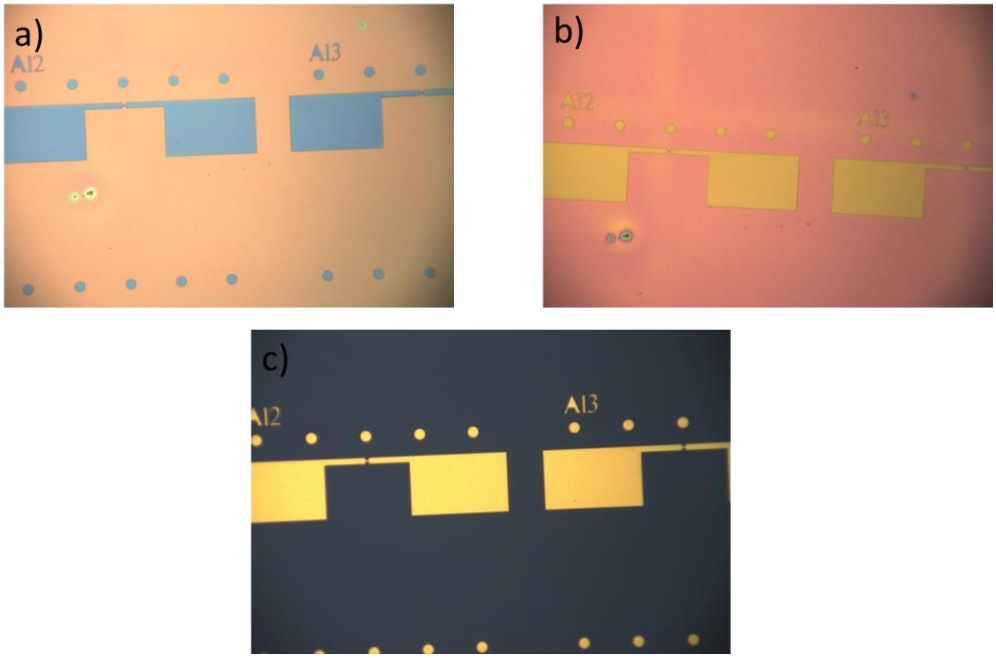

Figure 3.13 Optical microscope of the first contact layer deposition process. a) After EBL. b) After CF4 RIE. c) After lift-off process

The second main step is to transfer the graphene onto the sample. For this step, commercially available CVD graphene on a copper foil (Graphenea) was used. The graphene side of the copper foil was spin-coated with PMMA at 4000 RPM for 60 seconds and baked on a hot plate at 150 ºC for 2 minutes. O_2 RIE at a flow of 10 SCCM, pressure of 4 Pa, and RF power of 30 W was performed for 25 seconds on the backside of the foil to remove graphene from it. The copper with graphene and PMMA was left on ammonium persulfate (APS) overnight to etch the copper. Only a foil of graphene/PMMA remained on the next morning. The graphene/PMMA was transferred to beakers with DIW 3 times, while the Si/SiO_2 substrate was cleaned in acetone (5 minutes) and IPA (5 minutes). Finally, the graphene/PMMA foil was transferred from DIW to the Si/SiO_2 substrate. Figure 3.14 shows a schematic of the graphene transfer process.

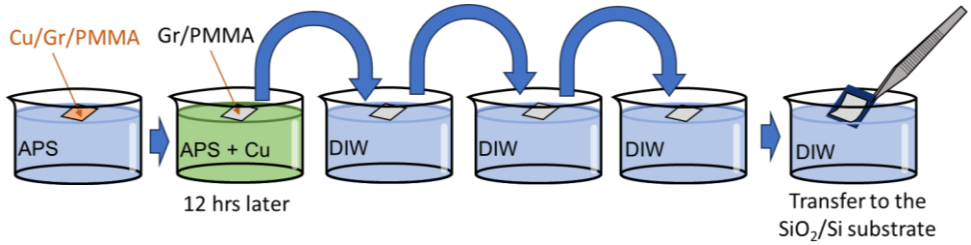

Figure 3.14 Schematic of the graphene transfer from a copper foil to the Si/SiO_2 substrate

After the graphene transfer, the sample was left to dry at room temperature for 3 hours to avoid the formation of water bubbles. Then, the sample was baked on a hot plate for 2 minutes at 200 ºC. After cooling down, the sample was left in acetone overnight. Annealing was performed in an infrared furnace for 3 hours at 300 ºC in an Ar + H_2(10%) atmosphere at a flow rate of 0.5 l/min.

The next step is to deposit the top metal contact layer. EBL was performed using AR-P and the same parameters as before (the spin-coating was performed just one time). 5 nm of chromium (rate: 1 Å/s) + 25 nm of gold (rate: 2.5 Å/s) were deposited by electron beam PVD, and lift-off was performed with remover AR 600-71 at 80 ºC for 5 minutes. Figure 3.15 shows the optical microscope images of one device after EBL and the lift-off process.

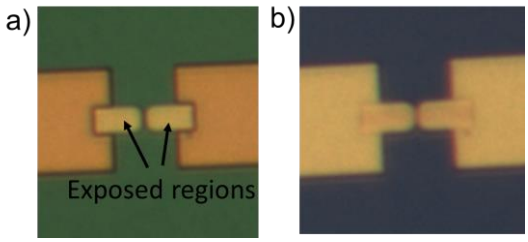

Figure 3.15 Optical microscope images of the top contact metal layer deposition. a) After EBL. b) After lift-off process.

The definition of the GNR was performed in the same way as in the case of the sample with suspended contacts. Bilayer of PMMA and AR-N 7520.07 was used. The development was performed with developer AR 300-47 for 50 seconds and DIW rinse for 30 seconds. Baking on a hot plate for 1 minute at 85 ºC was performed to increase the AR-N 7520.07 resistance to RIE. O_2 RIE was performed for 2 minutes and 15 seconds (10 SCCM, 4 Pa, and 35 W). The resist was removed with acetone for 10 minutes, and the sample was cleaned with annealing in an Ar + H_2(10%) atmosphere at a flow rate of 0.5 l/min at 300 ºC for three hours. Figure 3.16 shows the optical image microscope pictures of a device before and after the oxygen RIE.

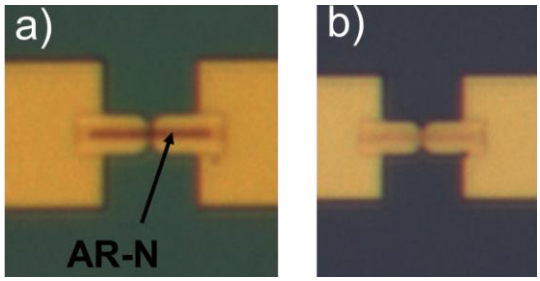

Figure 3.16 Optical microscope images of the definition of GNR step. a) After EBL. b) After O_2 RIE.

Before the GNR was suspended, tin with a thickness of 1 nm was deposited in half of the sample's devices. The tin was deposited by PVD in a resistive thermal evaporator. A metal mask was used to avoid the deposition of tin in half the sample. Finally, The GNR was suspended by wet etching the SiO_2 in BHF for 50 seconds (75 nm etching at a rate of 1.5 nm/second), followed by supercritical drying in the same way as performed for the sample with suspended contacts. Figure 3.17(a) shows a simplified schematic of the entire fabrication process. Figure 3.18(a) shows the tilted SEM image of one of the devices and Figure 3.18(b) shows the SEM image of a device functionalized with tin.

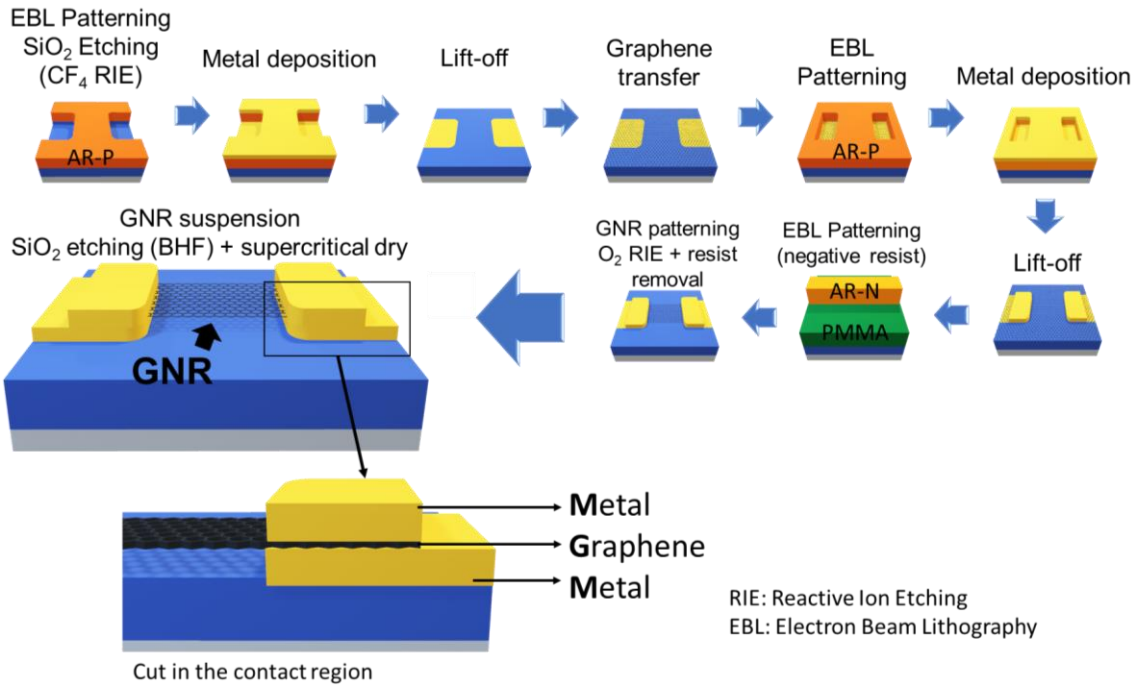

Figure 3.17 Schematic of the fabrication process of suspended GNR with metal-graphene-metal contact structure.

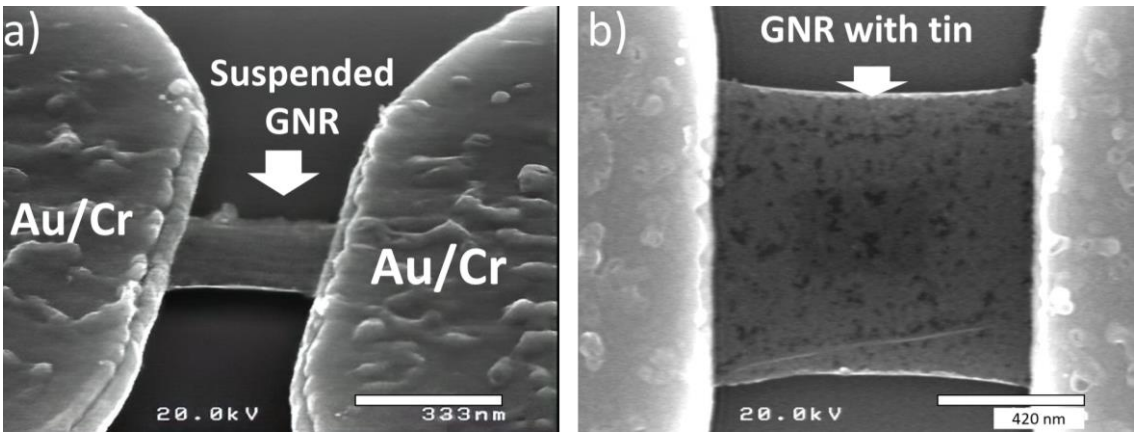

Figure 3.18 SEM image of a suspended GNR with metal-graphene-metal contacts. (a) tilted image of a device with $W = L = 400$ nm. (b) frontal image of a device with GNR and tin with $W = L = 1$ µm.

There was some overdevelopment during the definition of the bottom metal contact layer. Therefore, the real dimensions are different from the dimensions designed in the AutoCAD mask. Figure 3.19 shows a device with a mask length (L_{mask}) equal to 400 nm, but because of the overdevelopment, the real width is around 320 nm. Another point to notice is that over-etching also happened during the RIE step used to define the GNR width. As a result, the device has a real width of around 300 nm, while the channel in the EBL mask (W_{mask}) was projected to have 400 nm.

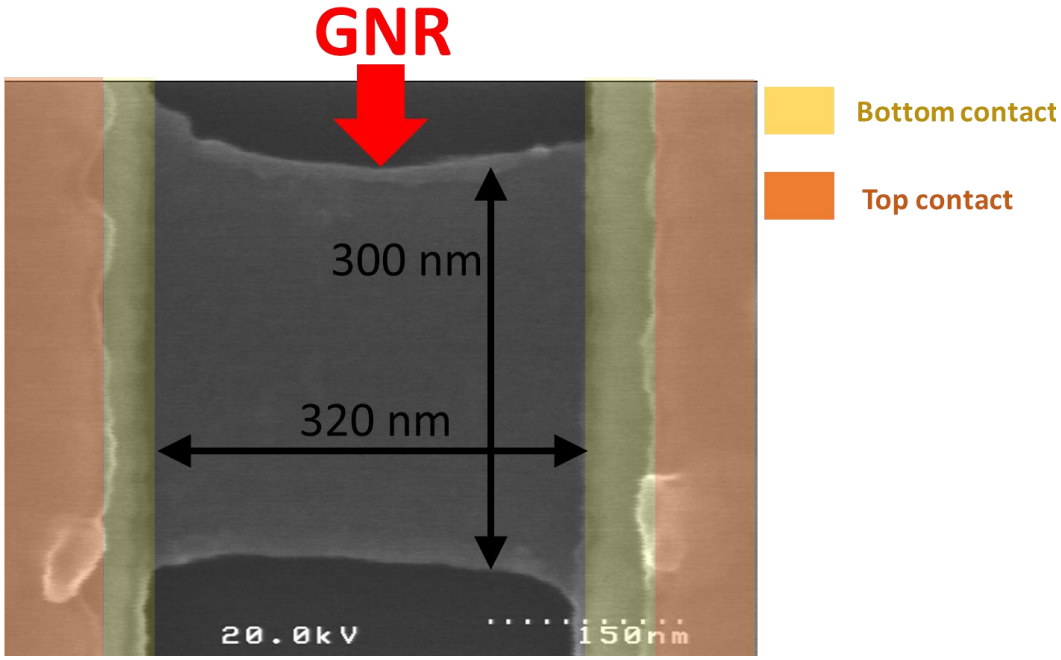

Figure 3.19 SEM image of a device designed to have $W_{mask} = L_{mask} = 400$ nm, but with smaller length and width than projected.

Another issue is that for most devices with $W_{mask} = L_{mask} = 200$ nm, the last lift-off process wasn't successful (Figure 3.20), and there is still a metal layer on the channel region. Because of this, these devices could not be utilized. All the SEM images were taken after the experiments so that the electron beam of the SEM would not alter the devices' characteristics.

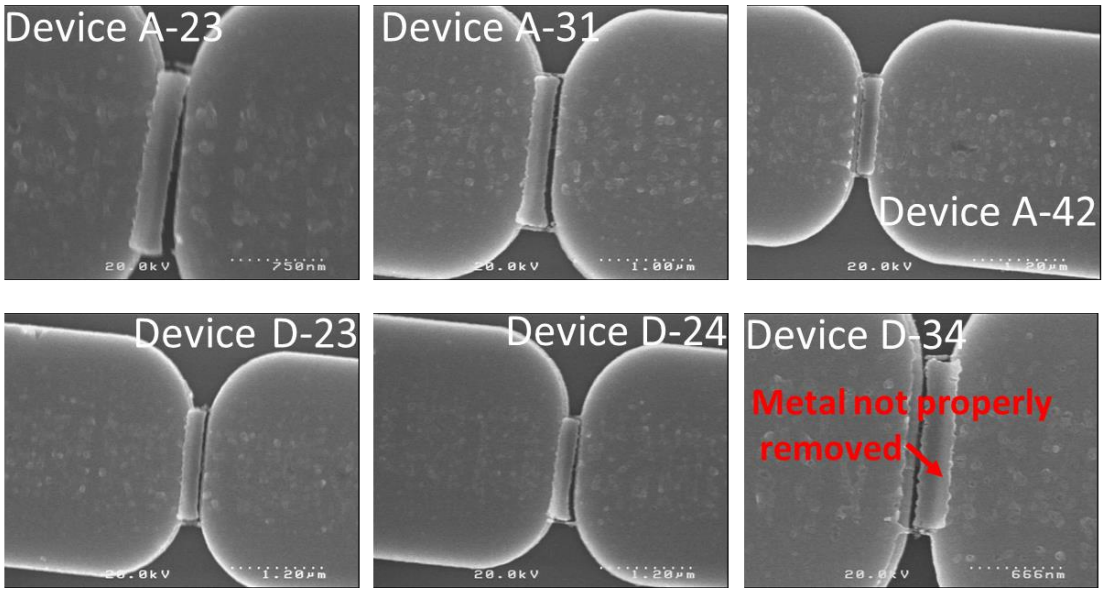

Figure 3.20 SEM images showing that the metal in the graphene channel area wasn't properly removed during the liftoff process in devices with length and width equal to 200 nm.

3.3 AC Lock-in Technique for Low-Frequency Noise Measurement

A problem with measuring low-frequency noise of a device is that amplifiers, and analog to digital converters present in measurement equipment also have low-frequency noise following the 1/*f* behavior. This intrinsic noise of the measurement set-up can hide the noise of the device, which is of interest for the purposes of this work. To overcome this issue, the AC lock-in technique was used [29] [30]. The basic principle is that an AC signal is applied to the device, such that its response will be at a higher frequency range, where the systemic noise is lower. The response of the device, then, can be recovered by demodulating the signal with a lock-in amplifier (LIA).

In the set-up utilized in this work, the Ultra-High Frequency lock-in amplifier (600 MHz) from Zurich instruments (Figure 3.21) generates a sinusoidal voltage signal

$\tilde{v}_d = \sqrt{2}v_d \cos(2\pi f_m t)$, where v_d is the root mean square (RMS) value of the sinusoidal signal and f_m is the frequency used for the modulation. This signal is applied to the drain terminal of the device, and the resulting electrical current is given by $i_d(t) = \sigma(t)\sqrt{2}v_d \cos(2\pi f_m t + \theta)$, where $\sigma(t)$ is the time-dependent electrical conductance of the device and θ is any phase lag that may appear due to the cables' length. Therefore, the current can be thought of as an AC signal ($\tilde{v}_d$) with amplitude modulated by the conductance of the device. During the measurements, f_m was set to 5 MHz.

Figure 3.21 UHF Lock-in Amplifier from Zurich Instruments used during the noise measurements.

The source terminal of the device is connected to the transimpedance amplifier HCA-400M-5K-C with a bandwidth (BW) of 400 MHz, and a gain (A) of 5 kV/A obtained from FEMTO (Figure 3.22). The datasheet states that the electrical current noise is 4.4 x 10^{-22} A^2/Hz at 100 MHZ, therefore it is unlikely that it will affect the noise measurements. The use of this amplifier is necessary to convert the electrical current signal into a voltage signal, so that the LIA can read it. This signal is given by $A\sigma(t)\sqrt{2}v_d \cos(2\pi f_m t)$, and is digitalized by the LIA analog-to-digital converter (ADC) at a sample rate of 1.8 x 10^9 samples per second. The electrical current values can be obtained by simply numerically dividing the input of the LIA by A, which can be done in the LIA settings. Another important point that must be considered is that the maximum peak voltage that the LIA can read is 3.5 V. Therefore, care must be taken such that the current never goes higher than 700 µA at any moment.

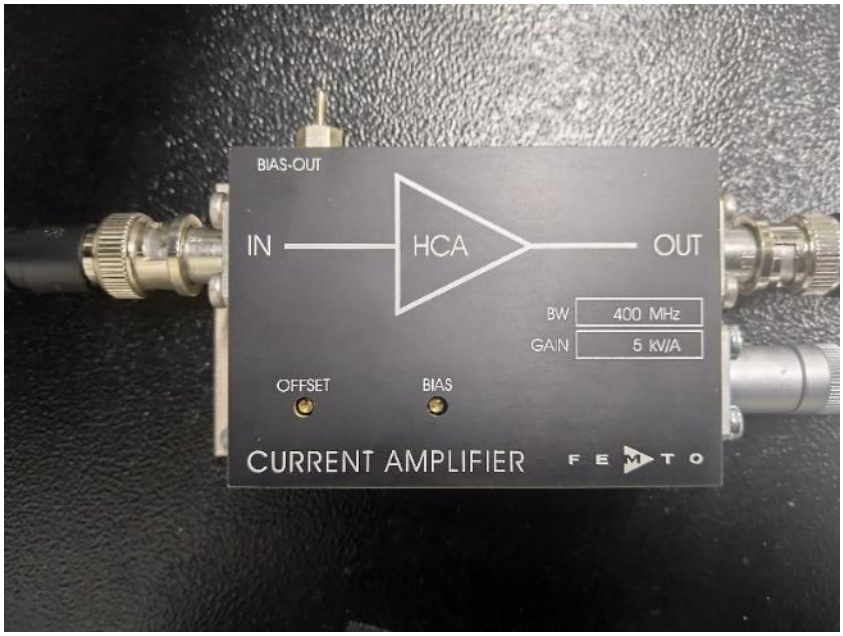

Figure 3.22 Transimpedance amplifier HCA-400M-5K-C from FEMTO.

The demodulation is digitally implemented by the LIA, and it results in two components: an in-phase component (***X***(*t*)) and a quadrature component (***Y***(*t*)). The in-phase component is obtained by multiplying the input signal by a reference at the same frequency as $\tilde{v}_d$ and phase 0º. The multiplication is given by:

$$\sqrt{2}\cos(\omega t) \times \sigma(t)\sqrt{2}v_d \cos(\omega_m t + \theta) = \sigma(t)v_d[\cos(\theta) + \cos(2\omega_m t + \theta)], \quad (3.1)$$

where ω = 2π*f*, and $\omega_m = 2\pi f_m$. By applying a low-pass filter (LPF), the high-frequency term (ω_m) is filtered, and ***X***(*t*) is given by $\sigma(t)v_d \cos(-\theta)$. The quadrature component is obtained by multiplying the input signal by a reference signal with a phase of 90º, followed by filtering. In a similar way to the in-phase component, we have $\boldsymbol{Y}(t) = \sigma(t)v_d \cos(\pi/2 - \theta) = \sigma(t)v_d \sin(-\theta)$. The magnitude of the demodulated signal ($I_{rms}(t)$) is the quadradic sum of both components and it gives the RMS value of the current at each time $(I_{rms}(t)^2 = \sigma(t)^2 {v_d}^2[\cos(-\theta)^2 + \sin(-\theta)^2] = \sigma(t)^2 {v_d}^2)$. Therefore, the resistance as a function of time can be obtained by dividing v_d by I_{rms}. Figure 3.23 shows a schematic of the entire measurement process.

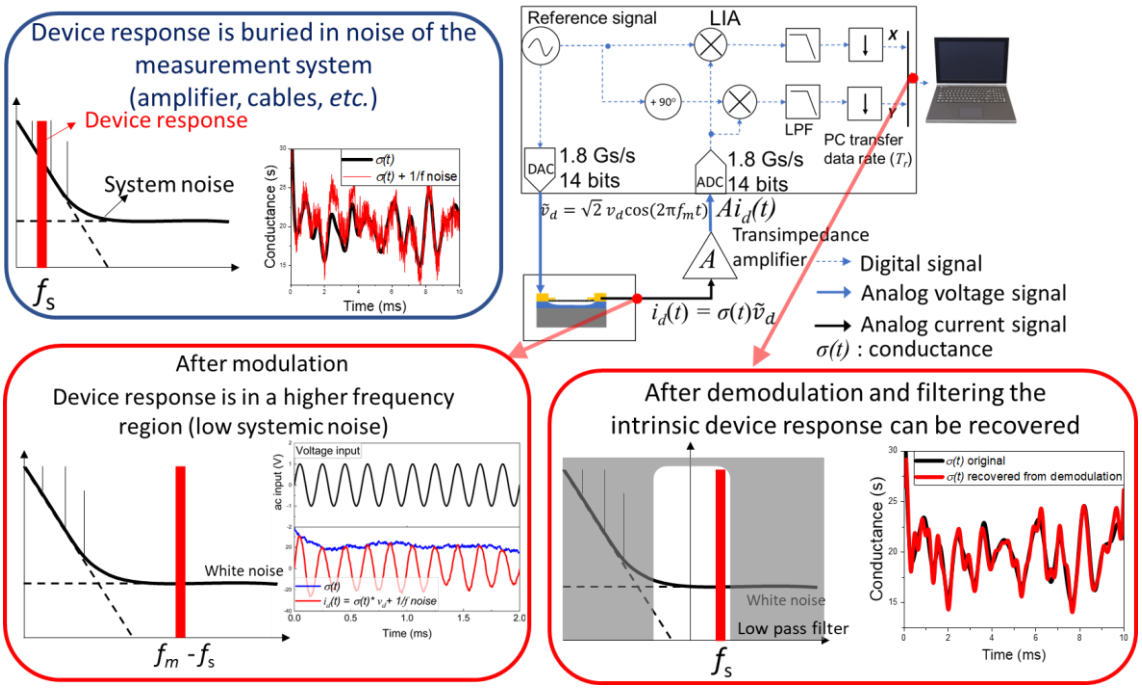

Figure 3.23 AC lock-in measurement schematic with simulated signal as example.

The demodulation and filtering are performed digitally inside the LIA at a sampling frequency of 1.8 GHz. However, the data is transferred to the personal computer (PC) controlling the LIA at a transfer rate (T_r) chosen by the user. From sampling theory, it is known that if the sampling rate is smaller than the BW of the signal, the high-frequency components can appear as low-frequency components through aliasing [66]. Therefore, *Tr* and the LPF BW must be chosen considering aliasing effects and storage memory of the PC. As will be shown later, noise measurements with 1 minute or less of duration were performed with an LPF BW of 78.45 kHz, and T_r = 219.7 kHz. Longer measurements (up to 10 minutes) had to be taken at T_r = 429 Hz, and the LPF BW was set to 30 Hz. The T_r in either case is more than two times that of the filter bandwidth, and it should be enough to avoid aliasing problems.

From the electrical current time series of the LIA, the PSD (S_I) is estimated using Welch's method [67]. In this work, S_I was obtained with the function "pwelch" of MATLAB. The total signal is divided into four segments and an overlap of half the size of each segment was used during the calculations. The MATLAB code used to calculate the S_I is shown as follows.

```
%I: electrical current vector
%SI: power spectral density vector
%f: frequency vector
%Fs: Sampling frequency
seg_size = round(length(I)/4); %size of each segment.
n_overlap = seg_size/2; %overlap size
[SI,f] = pwelch(I,seg_size,n_overlap,[],Fs,'ConfidenceLevel',0.95);
```

It is important to point out that $\sigma(t)$ also includes the conductance of the cables. In the set-up used in this work, three biaxial cables with characteristic impedance of 50 Ω were used. One cable is used to connect the output of the LIA to the device drain, one to connect the device source to the transimpedance amplifier, and the third is necessary to connect the amplifier to the input of the LIA. Therefore, it seems advantageous if the noise of the cables can be estimated. To do so, the cables were connected in series directly between the output and input of the LIA, and the voltage time series was monitored for 30 seconds with v_d = 100 mV, LPF BW of 78.45 kHz, and T_r = 219.7 kHz. The modulating frequency used was 5 MHz. Figure 3.24 shows the product between the normalized PSD and the frequency (remembering that $S_I/I^2 = S_V/V^2$). The roughly horizontal curve in Figure 3.24 shows that 1/*f* noise is still present, and that the PSD x frequency has a value of approximately 2 x 10^{-8}.

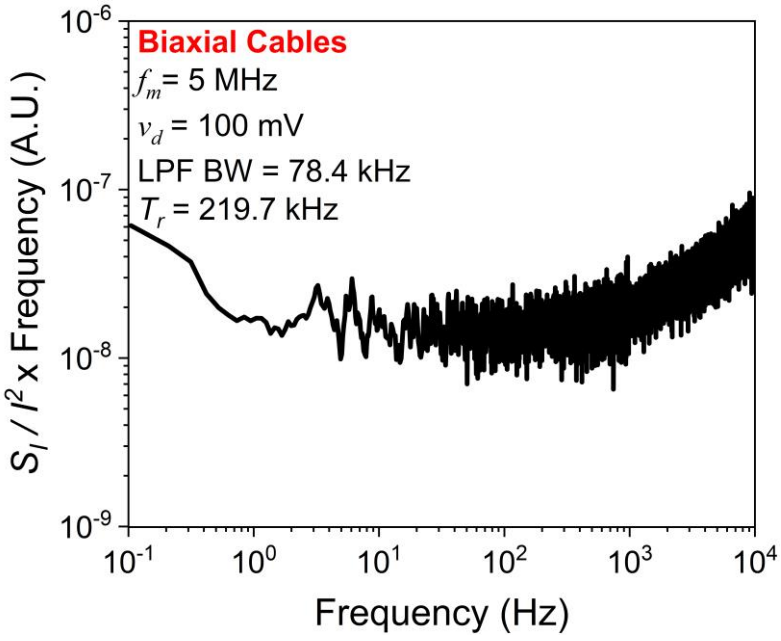

Figure 3.24 Normalized Power Spectral density x Frequency of the biaxial cables.

Another advantage of using an LIA to measure noise is that the $\boldsymbol{X}(t)$ and $\boldsymbol{Y}(t)$ components can be used for further signal processing and filtering. The power spectral density for frequencies lower than $f_m/2$ can be approximated by [30]:

$$S_I \approx G^2[S_I^0(f_m - f) + I_{rms}^2 S_{Id}(f)cos^2(\varphi)], \tag{3.2}$$

where G is the amplifier(s) gain, S_I^0 is the background noise, S_{Id} is the noise of the device, and φ is the phase angle of the demodulation. By demodulating at $\varphi = 90^o$ (component $\boldsymbol{Y}(t)$), the background noise can be stipulated. With $\boldsymbol{Y}(t)$ as an estimative of the background noise, a Wiener filter ($\Phi(f)$) was applied by multiplying the Fourier transform of the signal by the filter, which in the frequency domain has the following form [30]:

$$\Phi(f) = \frac{|\widehat{\boldsymbol{X}}(f)|^2 - |\widehat{\boldsymbol{Y}}(f)|^2}{|\widehat{\boldsymbol{X}}(f)|^2}, \tag{3.3}$$

where $\widehat{\boldsymbol{X}}(f)$ and $\widehat{\boldsymbol{Y}}(f)$ are the Fourier transform of the $\boldsymbol{X}(t)$ and $\boldsymbol{Y}(t)$, respectively. Equation 3.2 is one of the reasons why f_m was chosen to be 5 MHz, since it is only valid for frequencies way below the f_m. Figure 3.25 shows the power spectral density for both components and the result of the filtering for a suspended GNR with $W = L = 200$ nm (suspended contact). To recover the filtered signal in the time domain, one just needs to apply the inverse Fourier transform. This filtering process was applied to all the data obtained by the LIA shown in this work.

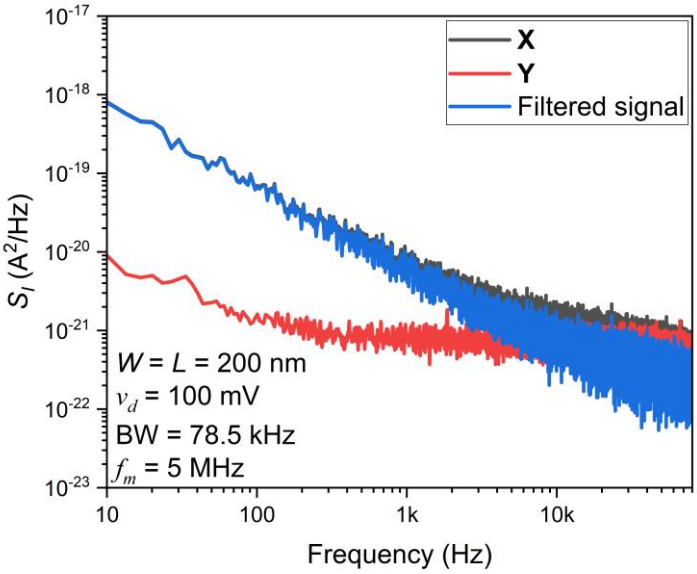

Figure 3.25 Power spectral density of $\boldsymbol{X}$, $\boldsymbol{Y}$ component, and the resulting filtered signal.

Chapter 4
Anomalous Random Telegraph Signal in Oxygen Environment

In this chapter, the effect of oxygen in two devices (Device A and Device B) is presented. Both devices were fabricated at the same time in the same sample with the suspended contact structure. Also, both have the same size ($W = L = 200$ nm). Oxygen was chosen as the object of this study because it has a large influence on graphene (charge transfer from graphene to the O_2 of 0.2 electrons per molecule [37]) and because it is the second most abundant gas in our atmosphere. Therefore, the results obtained in this section may be useful for devices based on graphene that will operate in air and/or environments rich in oxygen.

4.1 Thermal and Current Annealing for Device Cleaning

After fabrication, it is unavoidable that resist leftovers from lithography procedures will be on the GNR. Also, exposure to air results in the adsorption of oxygen and water molecules on the graphene, resulting in doping [68]. Therefore, to study the effect of gas on pristine graphene, it is very important that the surface of graphene is as clean as possible. Annealing in a vacuum can be used to clean the graphene.

The sample was loaded into the gas chamber and left in a vacuum of approximately 6 mTorr. Device A was annealed by using electrical current annealing. In this process, a large drain current (250 μA) was applied to the device until the CNP was around 0 V. The transfer characteristics (I_D vs V_G) were obtained using the Keysight B1500 parameter analyzer (Figure 4.1(a)) and using the bottom Si as the gate electrode (Figure 4.1(c)).

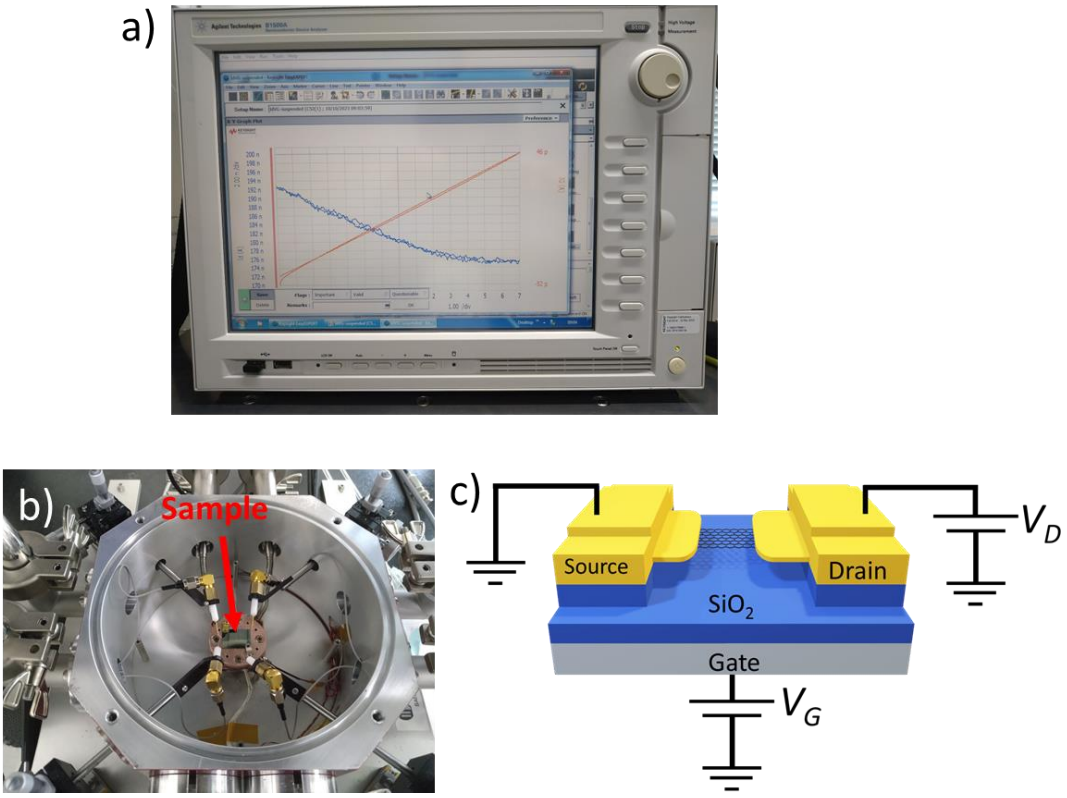

Figure 4.1 Measurement. (a) B1500 Semiconductor Parameter Analyzer. (b) Gas chamber and measurement stage. (c) Schematic of the transfer characteristics measurement.

Figure 4.2(a) shows the transfer characteristics of device A before the annealing, right after the annealing, and 4 hours after the annealing. The V_G range was kept between -7 and 7 V to avoid the risk of collapse of the suspended GNR due to electrostatic forces. It can be noticed that hysteresis between the forward and backward sweep is not present in any measurement. This is a good indication that the device is suspended. In the case of suspended devices, the gate voltage sweep can charge carrier traps in the oxide interface, and hysteresis is usually observed between the forward and backward sweeps [69]. Initially, the graphene is p-doped and the CNP is not in the measurement range. After current annealing, impurities evaporate and/or diffuse away from the graphene [70], and the CNP is close to 0 V. However, after a waiting time in a vacuum, the CNP changes to positive values and is not in the measurement range anymore. Figure 4.2(b) shows the transfer characteristic taken in an interval of 24 minutes, where it is visible that the CNP slowly becomes more positive. Figure 4.2(c) shows the CNP obtained from Figure 4.2(b). The CNP shift seems to be slower than 1 V per minute. This rate also seems to slow down after some time. Therefore, the CNP shift won't interfere with the measurements, especially if there is some waiting time before the noise measurements.

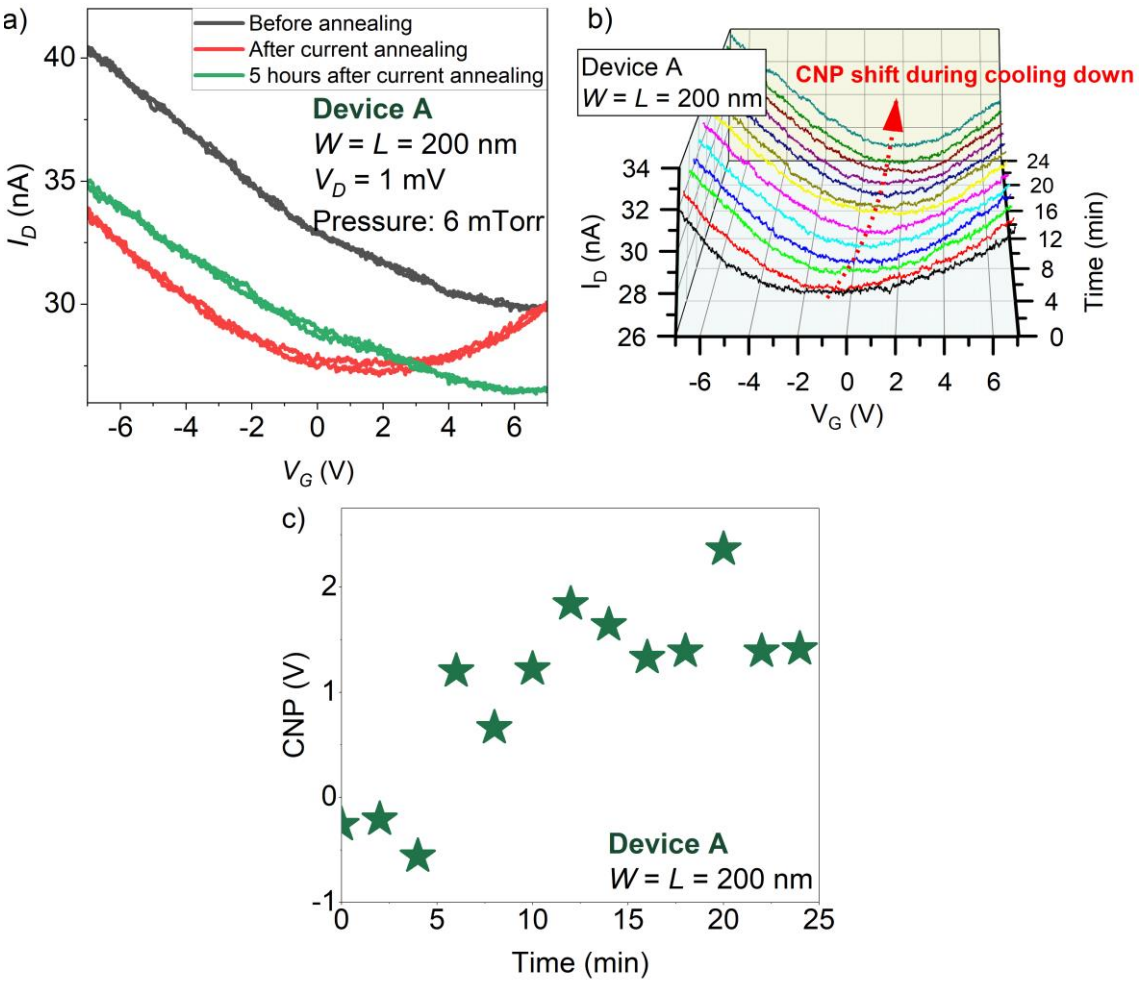

Figure 4.2 Current annealing of Device A. (a) Transfer characteristics of Device A before and after current annealing. (b) Transfer characteristic of Device A as it was cooling down in a vacuum. (c) CNP of Device A as it was cooling down.

It is known that graphene on SiO_2 substrate will be n-doped when heated, and the CNP will become more positive as the sample cooldown [71]. However, this device is suspended, so there is no effect of the SiO_2 on the graphene. It is important to point out that 6 mTorr is not a very good vacuum. The number of gas molecules inside the chamber can be estimated from $PV = Nk_BT$, where P is the pressure, V is the volume, N is the number of molecules, k_B is the Boltzmann constant (1.380649 x 10^-23 J/K), and T is the temperature. The chamber used has a volume of approximately 2 liters, which results in $N = 3.8 \times 10^{17}$ molecules at room temperature and $P = 6$ mTorr (0.8 Pa). These molecules could eventually adsorb on the graphene and be responsible for the positive CNP shift. Also, impurities on the contacts could diffuse to the channel, and molecules physiosorbed near the device (metal contacts and SiO_2 substrate), could desorb from their original place

and adsorb on the graphene. For device B, thermal annealing was used to try to eliminate the effect of nearby impurities. This time, the entire sample was heated at 150 ºC with a resistive heater for 4 hours. As can be seen in Figure 4.3(a), thermal annealing alone is not enough to bring the CNP to 0 V, and current annealing is still necessary. This happens because the temperature used is not enough to desorb molecules that are chemisorbed on defects and edges of graphene. However, it is enough to desorb molecules that are physiosorbed near the device. After the CNP is brought close to 0 V with current annealing, the shift is much smaller, and the CNP is around 4 V even after 3 hours of waiting time in a vacuum. A very similar behavior was observed when thermal annealing at 150 ºC for 3.5 hours was used before current annealing in Device A (Figure 4.3 (b)). In this case, the CNP is around 2 V even after 3.5 hours of waiting time in a vacuum.

While more investigation on the topic is necessary, these results reinforce the hypothesis that nearby impurities could be diffusing to the graphene channel and p-doping the device. Nevertheless, the investigation of this effect is beyond the scope of this work, and the main point is that the CNP shift will not affect the subsequent noise measurements.

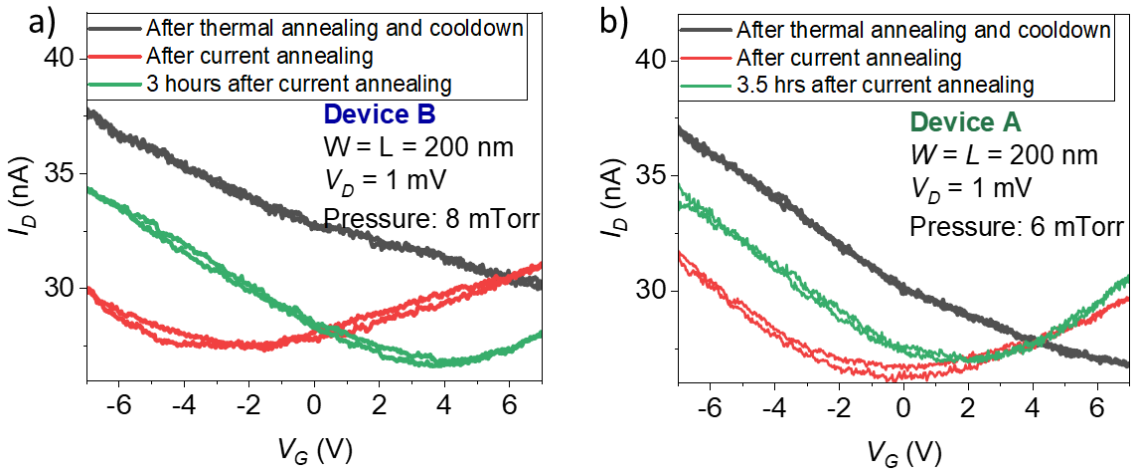

Figure 4.3 Transfer characteristics with thermal annealing. (a) Device B. (b) Device A.

4.2 Low-Frequency Noise in a Vacuum and Oxygen Environment

After the annealing, the resistance time series measurements of the devices were performed in vacuum and oxygen environments with the LIA using the lock-in technique explained in section 3.3. The two devices were measured on different days. For Device A, only current annealing was performed before the experiments. Thermal annealing

followed by current annealing was used before the measurements with Device B. An AC signal of 150 mV peak (v_d = 106 mV) with f_m = 5 MHz was applied to the drain terminal of the devices. The resistance time series was obtained as explained in section 3.3, followed by wavelet denoising (Appendix C). For completeness, the raw data obtained from the LIA (electrical current as a function of time) is shown in Appendix D. No gate voltage was applied during these measurements. Measurements of the resistance time series were performed for around 1 minute in a vacuum with pressure of 6 mTorr (Device A) and 8 mTorr (Device B). An LPF of order one and BW of 78.45 kHz was used to filter the signal during the demodulation. The Transfer rate was set to 219.7 kHz. Figure 4.4 (a) and Figure 4.4(b) show the resistance time series of Device A and Device B, respectively. The noise shown looks like pink noise (1/f noise). However, a closer observation shows that at some moments, there is a resistance drop, as shown in Figure 4.4(c) and Figure 4.4(d). Likely, this is caused by adsorption and desorption of gas molecules that are still present in the chamber. However, they are too rare and sparse to be statistically analyzed.

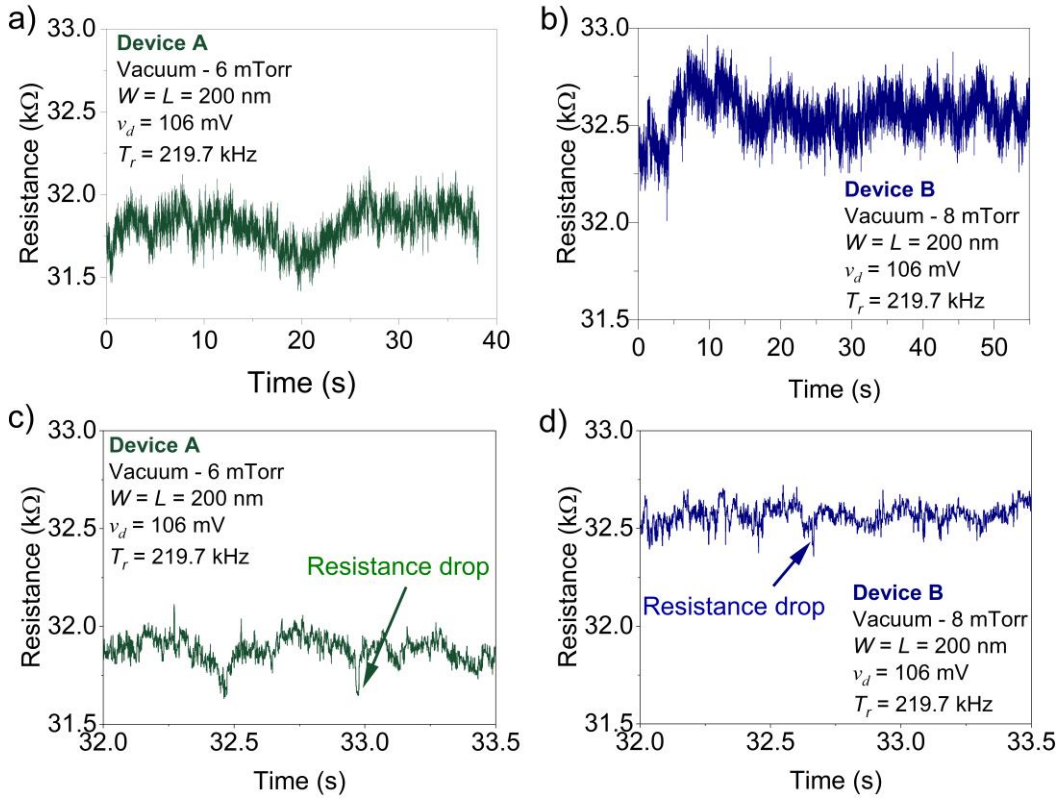

Figure 4.4 Resistance time series in a vacuum. (a) Entire time series of Device A. (b) Entire time series of Device B. (c) 1.5 seconds section of time series of Device A. (d) Section of 1.5 seconds of the time series of Device B.

The resistance of Device A was measured while pure oxygen was introduced into the chamber at a rate of 100 SCCM. The oxygen was introduced from a cylinder with grade 2 (purity greater than 99.999%) provided by Unosanso Ltd. Figure 4.5 shows the resistance time series (black line), and the standard deviation calculated in windows of 10 seconds (red line). Due to memory concerns, this measurement was performed with T_r = 429 Hz and LPF BW = 39.18 Hz. From visual inspection, it can be noticed, that at around 250 seconds ($P \approx 370$ Torr) there is an increase in the noise. This increase in noise can be confirmed by looking at the standard deviation. Initially, the standard deviation was between 50 Ω and 100 Ω. After 250 seconds, there is a sudden increase, and the standard deviation varies between 100 Ω and 200 Ω. While the increase in noise due to oxygen was observed, it is unclear if it was caused by the pressure change or the prolonged exposure to the gas.

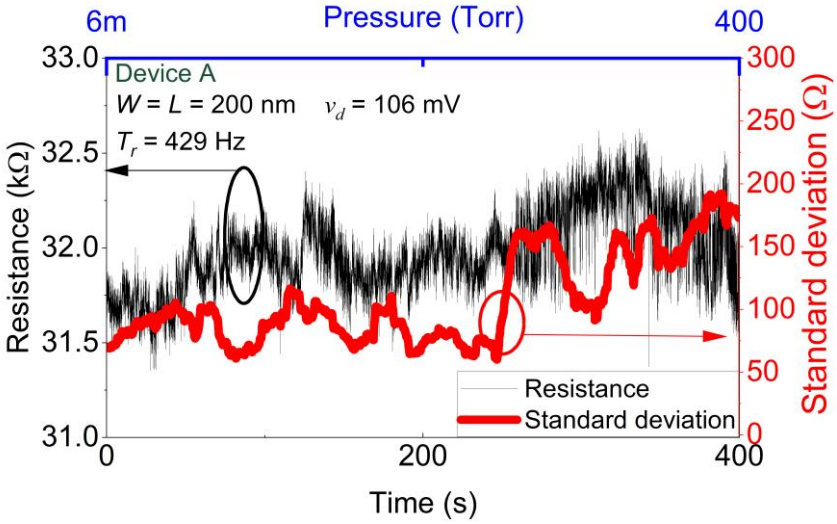

Figure 4.5 Resistance time series and standard deviation in windows of 10 seconds of Device A as oxygen is introduced into the gas chamber.

After the pressure arrived at 400 Torr, the oxygen flow was stopped, and resistance measurements at T_r = 219.7 kHz were performed. The same procedure was performed with Device B, though the resistance time series wasn't monitored during oxygen introduction. Figure 4.6(a) shows the initial and end of the resistance time series in the oxygen environment of Device A, and Figure 4.6(b) shows the time series of Device B. It is clear that the increase in noise is due to the appearance of RTS. In Device A, what seems to be a usual two-state RTS is present. In Device B, the RTS has a more interesting behavior. Most of the time, the resistance has a value of approximately 31.2 kΩ, but at some periods (denominated as fast RTS), fast transitions between this value and 30.9 kΩ

are present. This corresponds to a percentage change of 0.96% between the high and low resistance values. Another important point is that the fast RTS seems to cease at the end of the measurement. This indicates that the RTS is the result of a transitory effect. While the RTS in device A seems more well-behaved, it also has differences between the beginning and end of the measurement, and it seems that the fast RTS becomes present at the end.

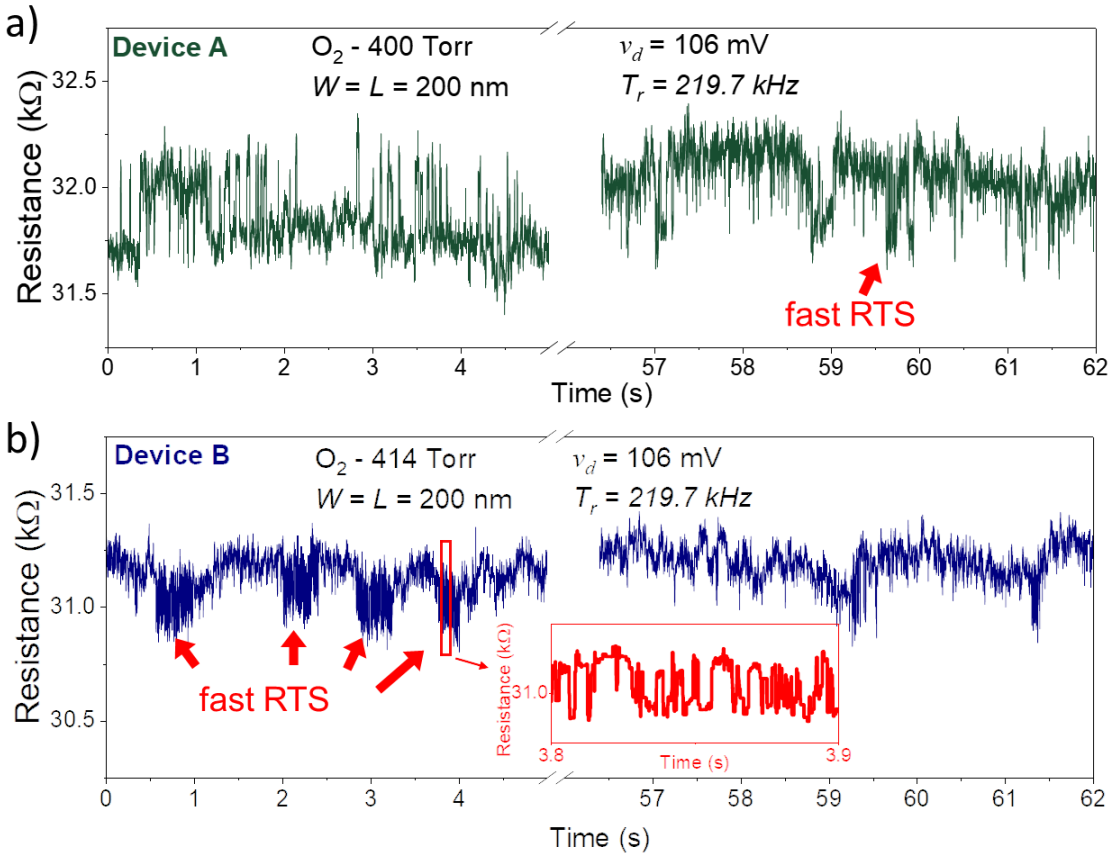

Figure 4.6 Resistance time series in oxygen environment. (a) Device A. (b) Device B

RTS like the one observed in Device B has already been demonstrated in MOSFETs and is usually denominated as “anomalous RTS” in the literature. In that case, the anomalous RTS was attributed to oxide charge traps with metastable states [72] [73]. However, these devices are suspended, and the effect of the substrate traps cannot explain the RTS.

A possible origin for the RTS is the trapping/de-trapping of charges between the adsorbed graphene molecules. Taking the resistance value of 30.9 kΩ, and $W = L = 200$ nm, the resistivity (ρ) of the GNR is 30.9 kΩ per square. Since the CNP is positive, at $V_G = 0$, the major charge carriers are holes, and the 2-dimensional hole density (p_{2d}) can be

estimated by $p_{2d} = 1/e\mu_h\rho$. By considering a usual field effect transistor (FET) model, the mobility can be estimated by: $\mu = \frac{\partial I_D}{\partial V_G}\frac{L}{C_G W V_D}$ [74]. The gate capacitance in the devices is given by the series arrangement of the SiO_2 layer and the gap layer. Since 70 nm of the 300 nm of SiO_2 was etched, the final SiO_2 has a thickness of 230 nm, and the gap between the substrate and GNR is 70 nm. Using the parallel plates capacitance relationship, the capacitance per area is given by ε/t_{ox}, where ε is dielectric permittivity, and t_{ox} is the isolator thickness (oxide and vacuum in this case). By using a dielectric constant of 3.9 for SiO_2, the total gate capacitance was calculated to be 6.86 nF/cm^2. The transconductance ($\partial I_D/\partial V_G$) was obtained by taking the derivative of the curve in green in Figure 4.3(a) (curve taken 3 hours after current annealing). To reduce the noise, the derivative was smoothed by adjacent averaging in windows of 50 points (the total number of points of the measurement is 561). Figure 4.7 shows the transconductance as a function of V_G, and it shows that for gate voltages lower than -4 V, the transconductance is approximately 1 nA/V. Finally, the mobility was calculated with these values and resulted in 146 cm^{2}V^{-1}s^{-1}. However, it is worth mentioning that the mobility of 146 cm^{2}V^{-1}s^{-1} is much smaller than the values expected for suspended graphene. One of the possible explanations is that graphene in these devices has many defects. Another point is that the voltage applied is too close to the devices' CNP, and the estimated mobility might be underestimated.

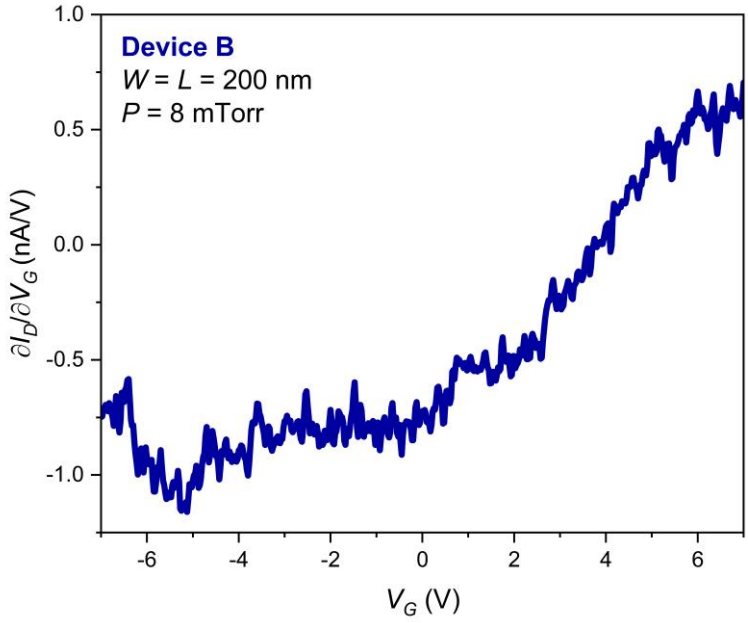

Figure 4.7 Transconductance ($\partial I_D/\partial V_G$) of Device B 3 hours after current annealing in a vacuum as a function of gate voltage (V_G).

Using μ_h = 146 $cm^2V^{-1}s^{-1}$, the carrier density was calculated to be 1.383 x 10^{12} cm^{-2} for Device B. Considering the GNR area, there are roughly 554 holes at one determined time. If one of these holes gets trapped, the remaining holes give a carrier density of 1.386 x 10^{12} cm^{-2}, and a resistivity of 30.95 kΩ per square, or a percentage change of 0.18% between the high and low resistivity. As commented before, the resistance change observed was 0.96%, such that it seems unlikely that the trapping/de-trapping of one carrier is responsible for the RTS. However, the mobility might be underestimated, and the hypothesis that charge trapping/de-trapping is causing the RTS cannot be completely ruled out.

Another possible explanation is that the RTS is caused by the movement of the oxygen molecules before they find an energetically favorable site to chemisorb. Under adsorption, there will be charge transfer from oxygen molecules to the graphene, resulting in p-doping of graphene. Since the devices are already slightly p-doped, this effect tends to reduce the electrical resistance of the GNR. Another effect of oxygen adsorption is the increase of Coulomb scattering, which tends to increase the electrical resistance. Therefore, the total effect will depend on these two competing effects, and their contribution can depend on the oxygen molecules' orientation, their relative position to the graphene plane, and on the adsorption site (if the adsorption site is a defect, and what kind of defect). For device B, most of the time, there is no RTS. In that case, the system (graphene, adsorbate, and gas) is in equilibrium. Once some disturbance occurs, some molecules could start oscillating on the graphene, changing their distance to the plane the contribution from doping and Coulomb scattering. At this moment it is unclear whether this is a collective effect, with the RTS being the average result of many molecules, or the effect of single/few molecules in specific adsorption sites.

Figure 4.8(a) shows the power spectral density of Device A and Device B in vacuum and oxygen environments. There is roughly no difference between the two devices in a vacuum, and the S_I follows the $1/f^{\alpha}$ behavior. A linear fit between 1 and 1 kHz shows that α has a value of 1.06 and 1.04 for Device A and Device B in a vacuum, respectively. After oxygen introduction in the chamber, the appearance of RTS shows as bulges in the *1/f* spectrum. These bulges are very clear for both devices, but they seem to be in different frequency ranges, which is expected since it was already evident that the RTS in both devices is different by inspecting the resistance time series. The RTS bulges can be better observed by plotting the product of S_I and the frequency (Figure 4.8(b)), where the bulges appear as peaks. For Device B, there is a clear peak around 200 Hz. For device A, the peak seems to be around 100 Hz. It is interesting to notice that the product between S_I/I^2 and the frequency has a minimum value of around 5 x 10^{-8} (Figure 4.8(b)).

This value is just a bit higher than the estimated noise from the cables at the same bias conditions shown in Figure 3.24 (2 x 10^{-8}). Since uncorrelated noise is summed [43], it can be concluded that the cables still have some effect on the measured noise. Nevertheless, the observed RTS PSD is larger than the background noise, so this is not a problem.

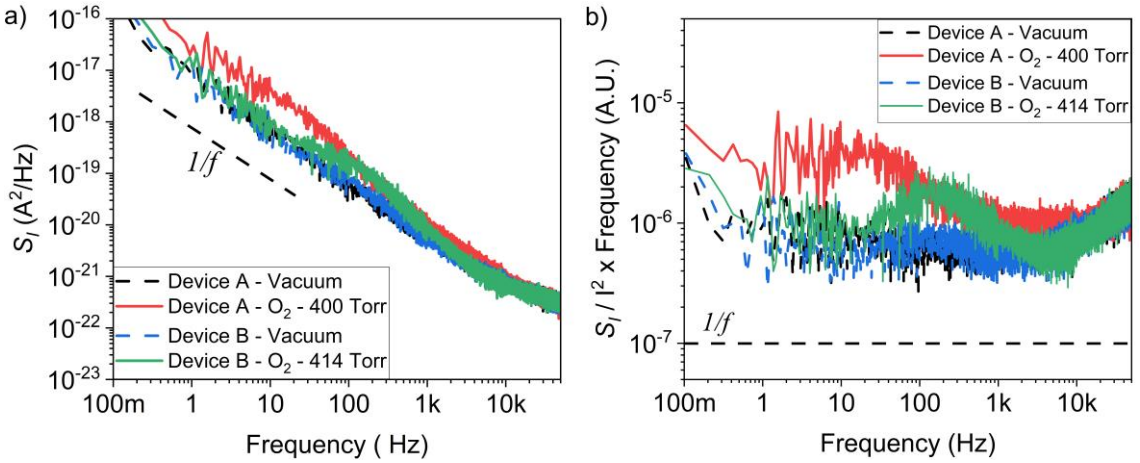

Figure 4.8 Frequency response. (a) Power spectral density of Device A and Device B in vacuum and oxygen environments. (b) Product between the normalized power spectral density and the frequency of Device A and Device B in vacuum and oxygen environments.

4.3 Statistical Analysis

A statistical analysis was performed on the RTS of both devices. For Device B, the regions with and without RTS were separated by taking the envelope of the signal. For such, the MATLAB function “envelope” with the option “peak” was used; with these settings, the envelope is obtained from the spline interpolation of maxima and minimum points (Figure 4.9(a)). The envelope amplitude was defined as the difference between the upper and lower limits of the envelope. Periods where RTS is present have a larger envelope amplitude than periods without it. As Figure 4.9(b) shows, there are two peaks in the histogram of the envelope amplitude (one at 165 Ω and another at 365 Ω). By considering only sections where the amplitude envelope is above 300 Ω, the fast RTS of Device B can be separated and analyzed.

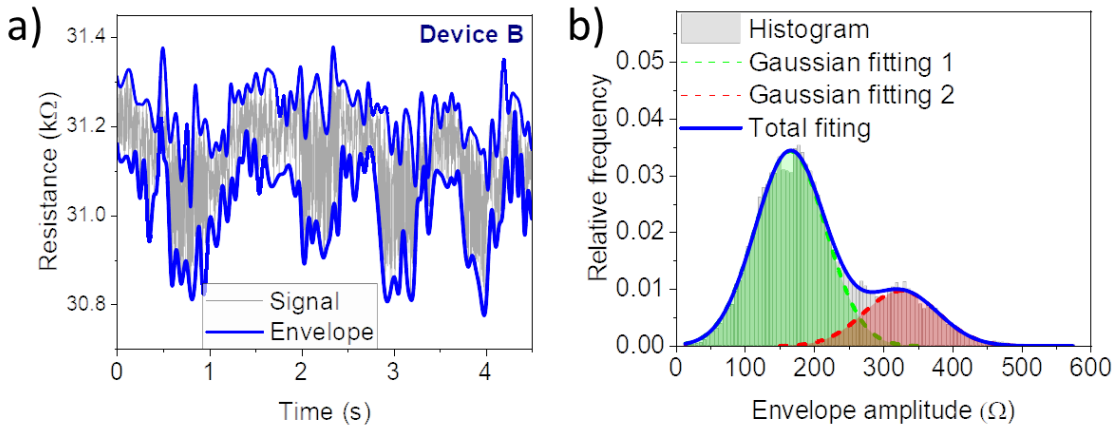

Figure 4.9 Envelope of the resistance time series of Device B. (a) Signal and envelope of a 5-seconds section. (b) Envelope amplitude histogram.

Figure 4.10(a) shows the histogram and the Gaussian fitting of the regions with RTS of Device B. The Gaussian fitting was performed using the software OriginPro 2022. The Gaussian curves give an estimative of the distribution probability of the RTS and can be used in a cumulative sum (CUMSUM) algorithm to determine when a transition between two states has occurred (Appendix E). From the CUMSUM algorithm, the time in which each transition (from up to the down state, and vice versa) can be obtained. From the time, the mean dwell time in the up state (t_{up}) and down state (t_{down}) can be obtained and stored in the order in which they occur. As commented in section 2, in the case that the RTS is a Poisson process, τ_{up} and τ_{down} can be estimated by plotting -ln(1-F), where F is the exponential distribution cumulative function. Figure 4.10(b) shows the probability plot of the dwell times of Device B. The symbols were obtained from the percentiles of experimental data, and the lines are the respective linear regression. From the slope of the lines, it was found that τ_{up} = 2.9 ms, and τ_{down} = 2 ms. Thus, on average, the GNR is in the high-resistance state for 2.9 ms and in the low-resistance state for 2 ms when RTS is present.

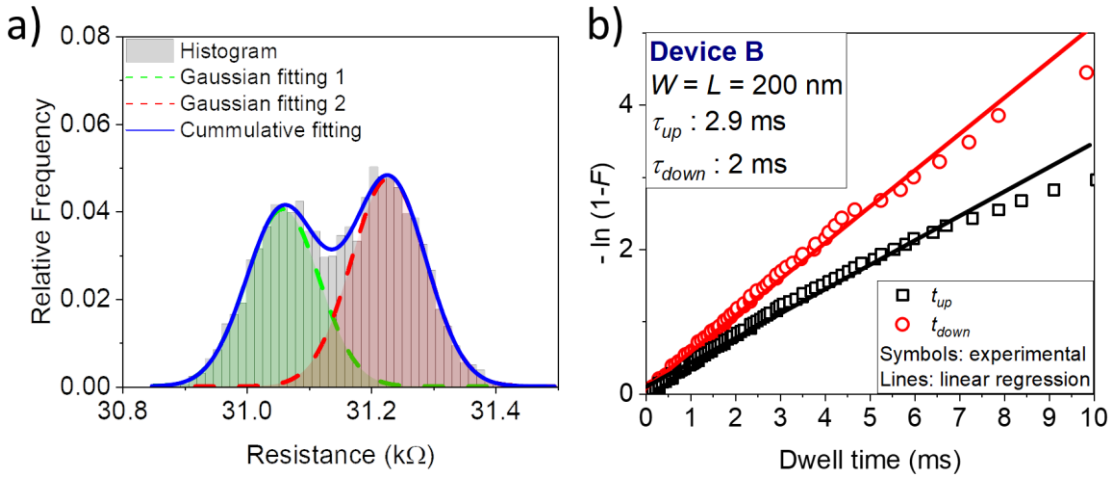

Figure 4.10 Statistical analysis of RTS of Device B. (a) Histogram and Gaussian fitting of the resistance on regions where RTS is present. (b) Exponential Probability plot of the dwell times in each state of the fast RTS, and its linear regression, where F is the cumulative probability.

Since RTS is present during the entire measurement range of Device A, the entire time series was analyzed. Figure 4.11(a) shows the histogram and the Gaussian fittings of the Resistance. Like it was done with Device B, the dwell times for Device A were obtained through the CUMSUM algorithm. It is important to point out that the dwell times of Device A don't follow the Exponential probability, which could indicate that the statistical behavior of the RTS is time-dependent. The temporal behavior of the dwell time was obtained to verify this hypothesis. Figure 4.11(b) shows t_{up} as a function of time. Naturally, the individual values of t_{up} don't tell much, and an estimative for τ_{up} is necessary. A moving average filter with a window of 1000 points was used to obtain an estimative of the average dwell times (red line in Figure 4.11(b). The result is that the estimated τ_{up} increases from around 6 ms at the beginning of the measurements to approximately 35 ms at the end. *i.e.*, the transitions are becoming rarer with time. For the down state case, there is also some variation (τ_{down} goes from 8 ms to around 3 ms). This strongly suggests that chemisorption is occurring at the end of the process. If physisorption was the main mechanism, the molecules could desorb at room temperature, and the average dwell time should be independent of time.

In summary, both devices have shown temporal dependence on their RTS. Also, as shown in the histograms of Figure 4.10(a) and Figure 4.11(b), the time spent in the high-resistance state is longer than in the low-resistance state in both devices. However, the time constants are different in the two devices (a simple average gives $\tau_{up,} = 19.37$ ms,

and $\tau_{down,}$ = 4.9 ms for Device A). Therefore, the RTS is device-dependent and might be related to gas molecule adsorption on defects. Another possibility is that the dwell times are different because of the time dependence of the RTS.

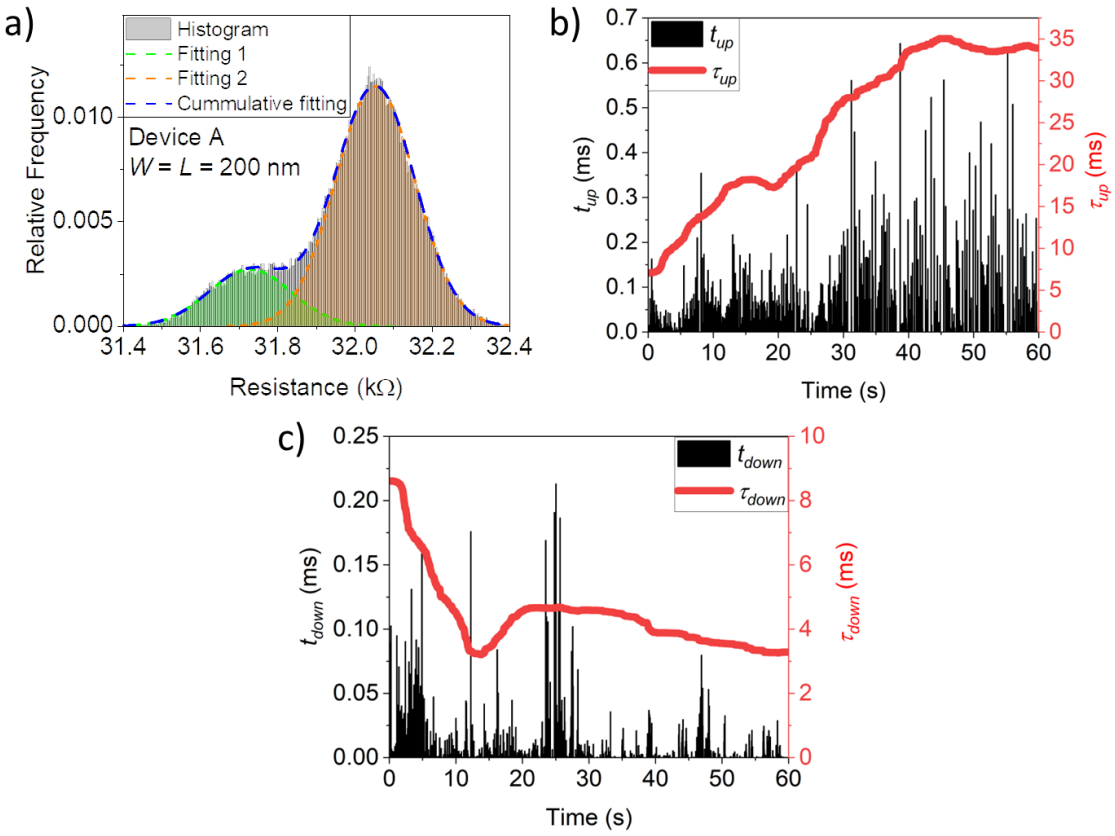

Figure 4.11 RTS analysis of Device A in an oxygen environment. (a) Resistance histogram of the entire measurement and Gaussian fitting. (b) Dwell time in the up state (t_{up}) in the left-hand axis (black columns) and the estimated mean dwell time (τ_{up}) in the up state in the right-hand axis (red line). (c) Dwell time in the down state (t_{down}) in the left-hand axis (black columns) and the estimated mean dwell time (τ_{down}) in the down state in the right-hand axis (red line)

4.4 Experiment Repetition with Device B.

Right after the first experiment with device B, the chamber was evacuated to around 10 mTorr and thermal annealing was performed at 150 °C for 1.5 hours. As shown in Figure 4.12, the CNP is not in the measurement range anymore due to oxygen doping. After new current annealing by applying a current of 250 µA, the CNP shifted to around – 3V. The device was left in a vacuum overnight for 14 hours. By the end of this period,

the positive CNP shift was observed again. However, even after 14 hours, the CNP is around 5 V, just 1 V higher than the CNP in the first experiment (Figure 4.3). This reinforces the argument that the CNP shift after many hours is negligible in the time scale of the noise measurements.

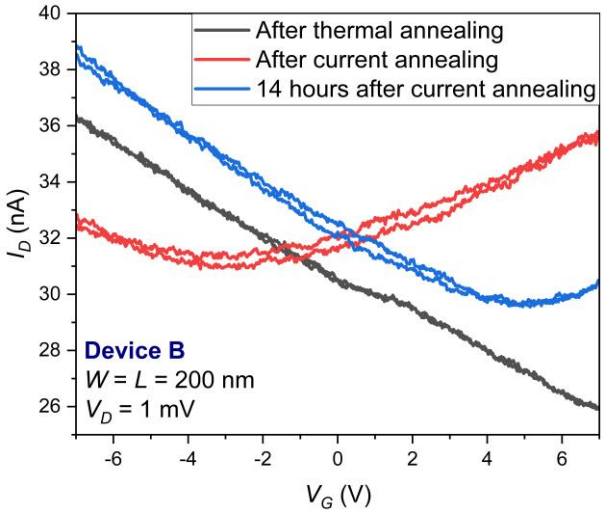

Figure 4.12 Transfer characteristics of Device B after thermal and current annealing.

To confirm that there aren't big chances in noise while the device is in a vacuum, the resistance was monitored in a vacuum for 5 minutes using the usual parameters for long measurements (Tr = 429 Hz, LPF BW = 39.18 Hz). Figure 4.13 shows the resistance time series (black line) and its standard deviation calculated in windows of 10 seconds (red line), where no change with time was noticed.

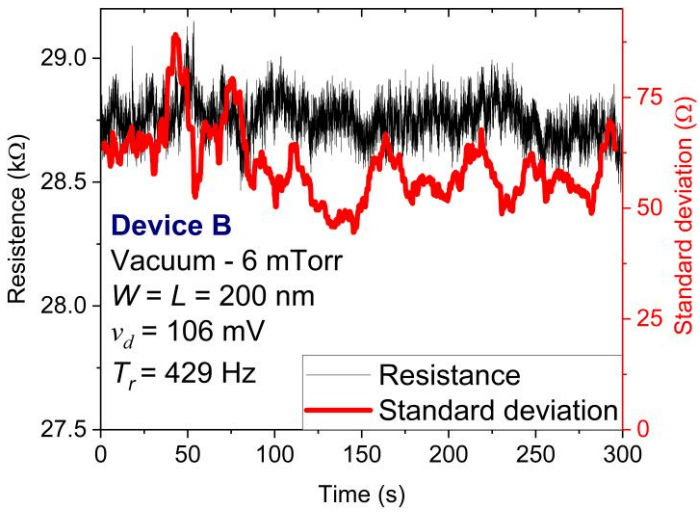

Figure 4.13 Resistance time series and standard deviation of Device B in a vacuum.

After the measurement shown in Figure 4.13, a new time series with a faster transfer rate was taken to analyze the electrical noise (in the same way as in the first experiment). Figure 4.14(a) shows the total resistance time series in a vacuum, and Figure 4.14(b) shows a section of 15 ms of duration. While the resistance baseline is around 28.6 kΩ, very sharp transitions to 29 kΩ are visible. These sharp transitions have a duration of just a few samples. Given that the sampling period is 4.5 μs, it is likely that their duration is even shorter, but the measurement setup could only capture the slower ones. As commented previously, the vacuum in the chamber is not very good. At a pressure of 6 mTorr (the pressure in this experiment), there are still 3.8 x 10^{17} molecules in the gas chamber. Therefore, these sharp transitions may be caused by the adsorption/desorption of leftover gas molecules.

Pure oxygen was introduced into the chamber until the pressure arrived at 400 Torr. Figure 4.14(c) shows the resistance time series in the oxygen environment after the influx was stopped. By comparing Figure 4.14 (a) and Figure 4.14 (c), the reduction of the resistance by the effect of doping by oxygen is clear. Also, by looking at a short section (Figure 4.14(d)), it becomes clear that the sharp transitions to higher resistance values are not present anymore. There are many more molecules able to adsorb on the graphene after oxygen introduction into the chamber. The larger coverage of the GNR may work as a protection film, and adsorption/desorption noise is reduced. Instead, there are some transitions with a larger duration to a lower resistance state. This behavior has similarities to the RTS observed previously. However, the transitions this time were too few, and a proper statistical analysis could not be performed. Chemisorption is a possible explanation behind the change in the RTS in the oxygen environment. During the first experiment, oxygen molecules were chemisorbed on the graphene, and when the experiment was repeated, there were fewer active sites for chemisorption. Also, the current annealing could have changed the structure of the GNR, and defects could've been removed and/or modified. However, the possibility of the RTS caused by oxygen having influence from defects needs further investigation.

After the measurement in an oxygen environment, the chamber was evacuated to around 10 mTorr. Five minutes after the evacuation, new measurements were performed (Figure 4.14(e)). This time, the resistance time series shows a hybrid of the two previous behaviors. Figure 4.14(f) shows that the general noise increased if compared to the measurements in oxygen (the total standard deviation increased slightly from 32.98 Ω to 49.4 Ω in a section of 0.5 seconds). This is expected if previously physiosorbed molecules desorb, giving space for adsorption/desorption noise to take place. Another point is that transitions to a low-resistance state are still present.

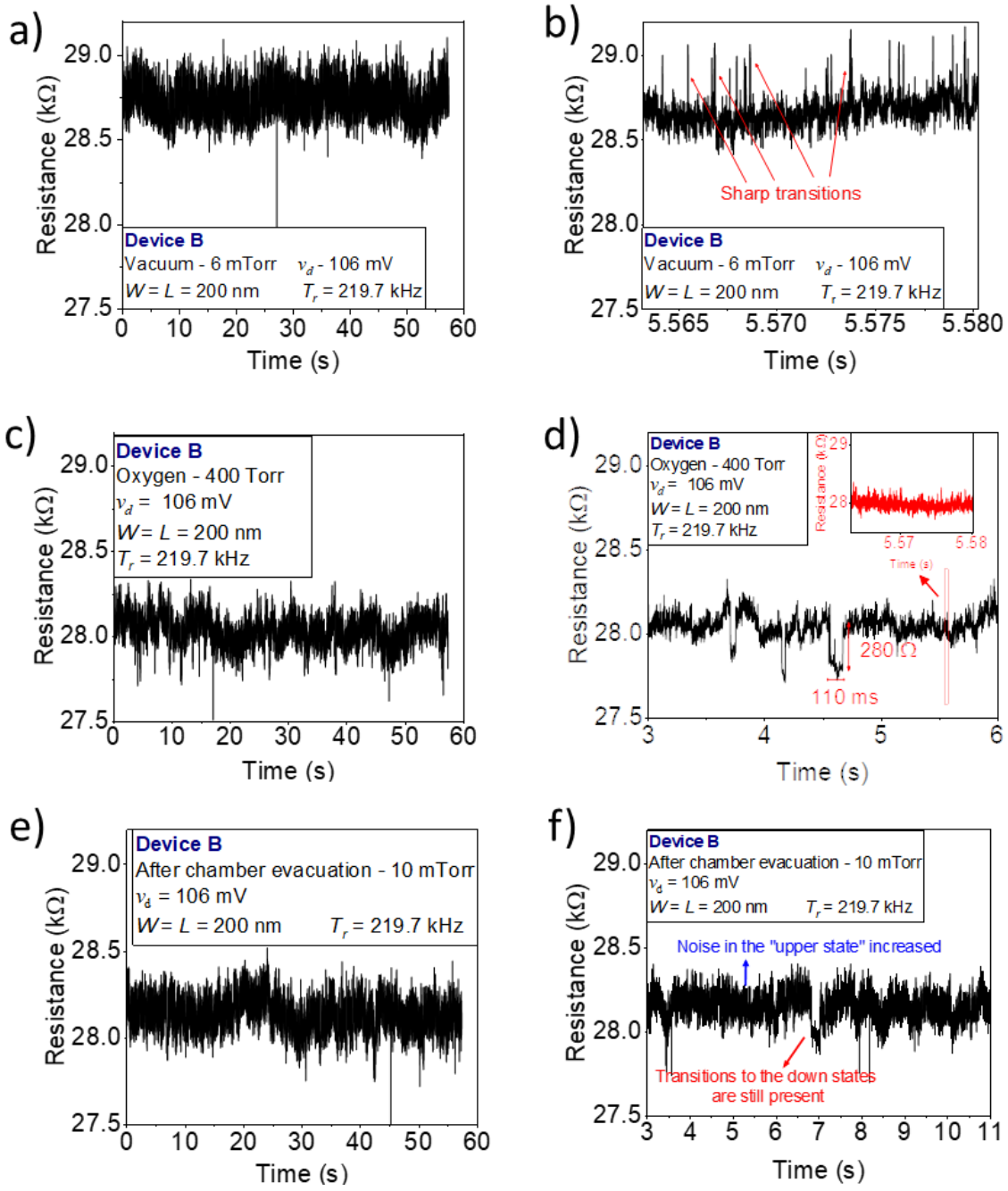

Figure 4.14 Resistance time series of Device B from the second experiment. (a) Total time series in a vacuum. (b) Section (15 ms) of resistance time series in a vacuum. (c) Total time series in oxygen environment. (d) Three-seconds section of resistance time series in oxygen environment. (e) Total time series after chamber evacuation. (f) Eight-second section of resistance time series after chamber evacuation.

Finally, Figure 4.15 shows the transfer characteristics before the RTS measurements (vacuum), after the measurements in an oxygen environment, and after the device was left in a vacuum of around 6 mTorr for 8 hours. In a vacuum, the CNP was originally at 4 V. The CNP shifts in the positive direction and is not visible in the measured range after oxygen introduction because of p-doping. After 8 hours in a vacuum, there was no noticeable change in the transfer curves, and the p-doping due to oxygen remains. If physisorption was occurring, the molecules would desorb after such a long time in a vacuum, and some shift in the CNP would be noticeable. Since that is not the case, it can be concluded that the chemisorption of oxygen molecules caused the doping.

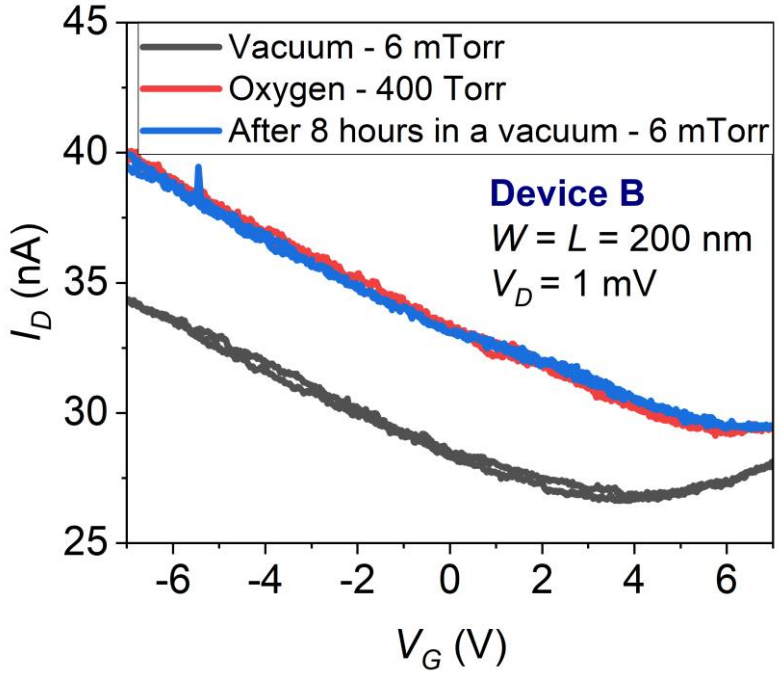

Figure 4.15 Transfer characteristics of Device B in a vacuum, in oxygen environment and after 8 hours in a vacuum.

It seems clear that the process of oxygen chemisorption oxygen on suspended graphene can cause RTS. However, the exact mechanism still needs more investigation. In particular, the influence of defects and impurities still needs to be investigated. As commented in Chapter 3, the devices presented in this chapter have suspended metal contacts, and the graphene under the metal contacts is also exposed. Because of this, it is unclear if the RTS is due to adsorption on the GNR channel or on the graphene under the metal contacts. In order to remove this uncertainty and investigate the effect of other gases on the suspended GNR, an improvement in the device design is necessary.

Chapter 5
Low-Frequency Noise of Tin-functionalized Suspended Graphene Nanoribbon

RTS with oxygen was observed in devices fabricated following the first design. However, the SiO_2 substrate is also etched in the contact area of those devices. Because of this, many devices collapsed on the substrate. Another issue is that, even for the devices that remained suspended, a large area under the suspended contacts has graphene exposed (much larger than the graphene channel). Therefore, it isn't clear if the RTS is a channel or contact effect. To solve this problem, a new sample following a new design was fabricated. In this sample, the Metal-Graphene-Metal (MGM) contacts avoid the excessive over-etching by BHF.

Another point is that defects may be acting as adsorption sites, and their influence on the RTS presented in Chapter 4 is unclear. If that is the case, defect engineering could be useful to enhance or reduce this extra noise. However, this approach is technically challenging, and small variations in the defects' position and structure may lead to large variations among devices. Another possibility is to use nanoparticles as adsorption sites. In this case, many adsorption sites can be introduced in the hope that the average effect of these sites will result in lower variation among different devices. In this work, tin (1 nm thickness) was deposited in half of the sample devices to investigate the possibility of using nanoparticles as adsorption sites to enhance the effect of gas molecules on the device's noise. Tin was chosen, because of previous experience using tin nanoparticles to functionalize graphene [75]. In this chapter, the results obtained from a sample fabricated following the MGM contact structure (Section 3.2) are presented.

5.1 Low-Frequency Noise in a Vacuum.

Initially, the effect of tin on the intrinsic noise of the devices was verified. This time current annealing wasn't used because its effect on the tin deposited on the graphene isn't clear. Thermal annealing was performed at 400 ºC for 4 hours in a vacuum of 6 mTorr. Eight devices were measured in a vacuum of 6 mTorr with the AC lock-in technique. The current of each device was measured for 30 seconds, with the following parameters: f_m = 5 MHz, Tr = 219.7 kHz, LPF BW = 78.45 kHz, and v_d = 50 mV. Four of the devices (group with "C" in the denomination) were functionalized with tin, while the other four (group "F") were not. All the devices were fabricated in the same sample, at the same

time. all devices have the same mask dimensions (W_{mask} = L_{mask} = 400 nm), though their real dimensions can be smaller than planned due to over-etching and overdevelopment. Table 5.1 summarizes the devices' nomenclature and which of them were functionalized.

Graphene functionalized with tin (1nm)	Device C-21
	Device C-22
	Device C23
	Device C-24
Graphene	Device F-21
	Device F-23
	Device F-24
	Device F-34

Table 5.1 Device nomenclature summary.

To compare the devices, it is easier to analyze their noise spectrum. The PSD was calculated using Welch's method, as already described in Section 3.3. Figure 5.1 shows the S_I/I^2 x frequency plot of these devices. It may sound reasonable that devices functionalized with tin could have a higher noise figure. However, except Device C-21, all the other devices have the same noise level. Therefore, functionalization with 1 nm tin doesn't seem to affect the noise level. Device C-21 is a particular case and will be addressed in more detail later in this text.

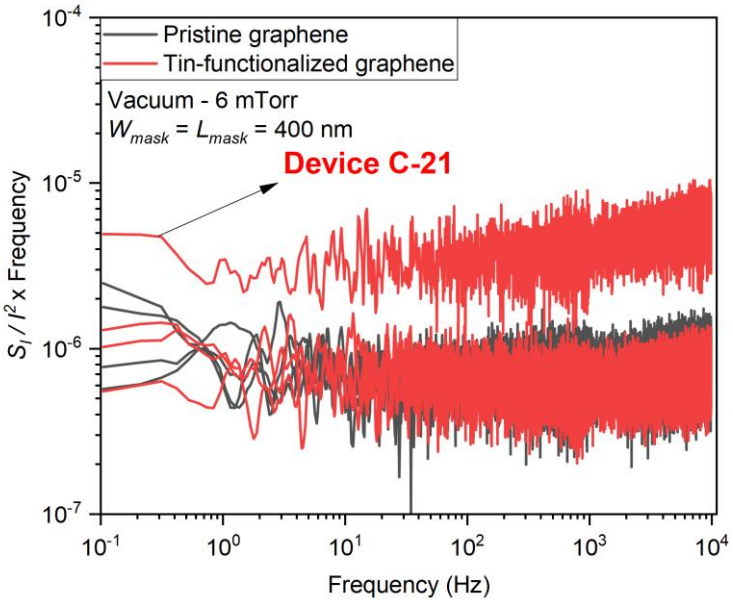

Figure 5.1 PSD x frequency in a vacuum of tin-functionalized graphene (red lines) and pristine graphene devices (black line) with MGM contacts.

5.2 Effect of Gas Molecules on Low-Frequency Noise

After the measurements in a vacuum, the effect of different gases on the low-frequency noise of the devices was verified. Before each exposure to a new gas, the chamber was evacuated and left in a vacuum for at least three hours at room temperature. Then, new measurements in a vacuum were taken, and gas was introduced at a flux rate of 100 SCCM until the desired pressure/concentration was achieved.

Ethanol was the first gas to be tested. There are two main motives for testing ethanol. The first one is that the PSD of supported exfoliated graphene showed a bulge at around 400-500 when exposed to ethanol vapor [26]. The second reason is that tin-functionalized graphene was used to obtain selectivity toward ethanol by the CNP-shift method. Ethanol diluted in nitrogen (an inert gas) was introduced into the chamber at a flux rate of 100 SCCM until the pressure achieved 154 Torr. The original ethanol concentration in the gas cylinder used is 9.73 ppm. Since the atmospheric pressure is 760 Torr, a pressure of 154 Torr is equivalent to a concentration of around 2 ppm. Measurements were performed with the LIA (same parameters as the measurements in a vacuum). After these measurements, gas was introduced once more at 100 SCCM until a pressure of 608 Torr (8 ppm).

Figure 5.2 shows the normalized PSD x frequency plot for the devices functionalized by tin in a vacuum and exposed to ethanol, while Figure 5.3 shows the same for pristine graphene. There was no ethanol effect on the devices' noise. It is not clear why the bulge at 400 Hz wasn't observed. One reason might be that CVD graphene is not suitable for these kinds of measurements. Another possibility is that the bulge is the result of interactions among the graphene, the SiO_2 substrate, and the gas. Since the devices in this work are suspended, there is no effect from the substrate, and the bulge isn't visible. Another difference is that in the experiments of reference [26] the vapor gas was diluted in dry air, and the other gas molecules present could also have some effect.

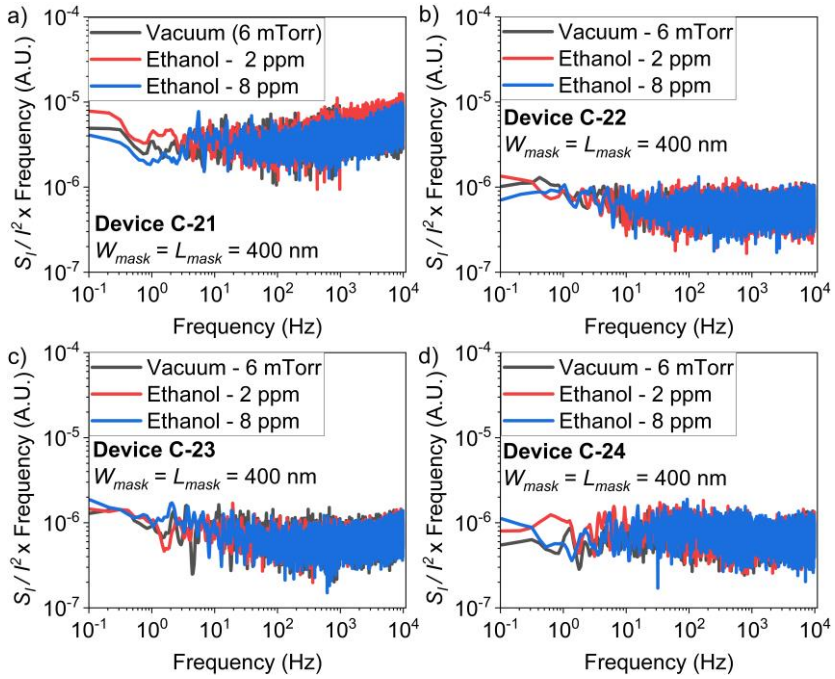

Figure 5.2 Product of the normalized power spectral density (S_I/I^2) by frequency as a function of frequency of tin-functionalized suspended GNR with MGM contacts in a vacuum and exposed to ethanol diluted in nitrogen at concentrations of 2 ppm (154 Torr) and 8 ppm (608 Torr).

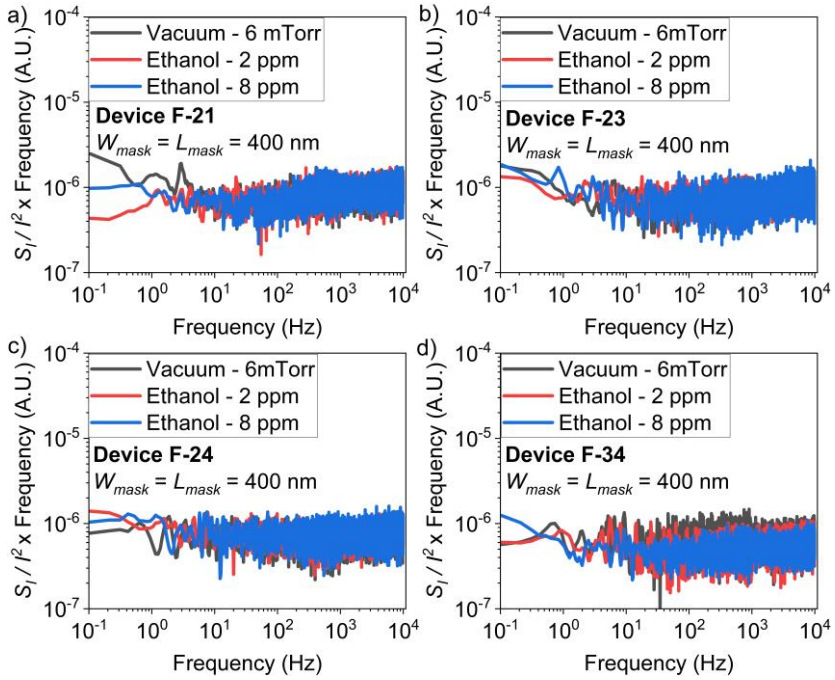

Figure 5.3 Product of the normalized power spectral density (S_I/I^2) by frequency as a function of frequency of suspended GNR with MGM contacts in a vacuum and exposed to ethanol diluted in nitrogen at concentrations of 2 ppm (154 Torr) and 8 ppm (608 Torr).

After the experiment with ethanol, the chamber was evacuated, and the devices were left in a vacuum at room temperature for 3 hours. Then, new measurements in a vacuum were taken (6 mTorr), and the same measurement scheme was performed with acetone. The gas cylinder used has acetone diluted in nitrogen at a concentration of 10.1 ppm. LIA measurements were performed at concentrations of 2 ppm (154 Torr) and 8 ppm (600 Torr). Figure 5.4 shows the PSD results for the devices functionalized with tin, and Figure 5.5 shows the results obtained for pristine graphene. Once more, there was no observable effect on the noise by the exposure to the targeted gas.

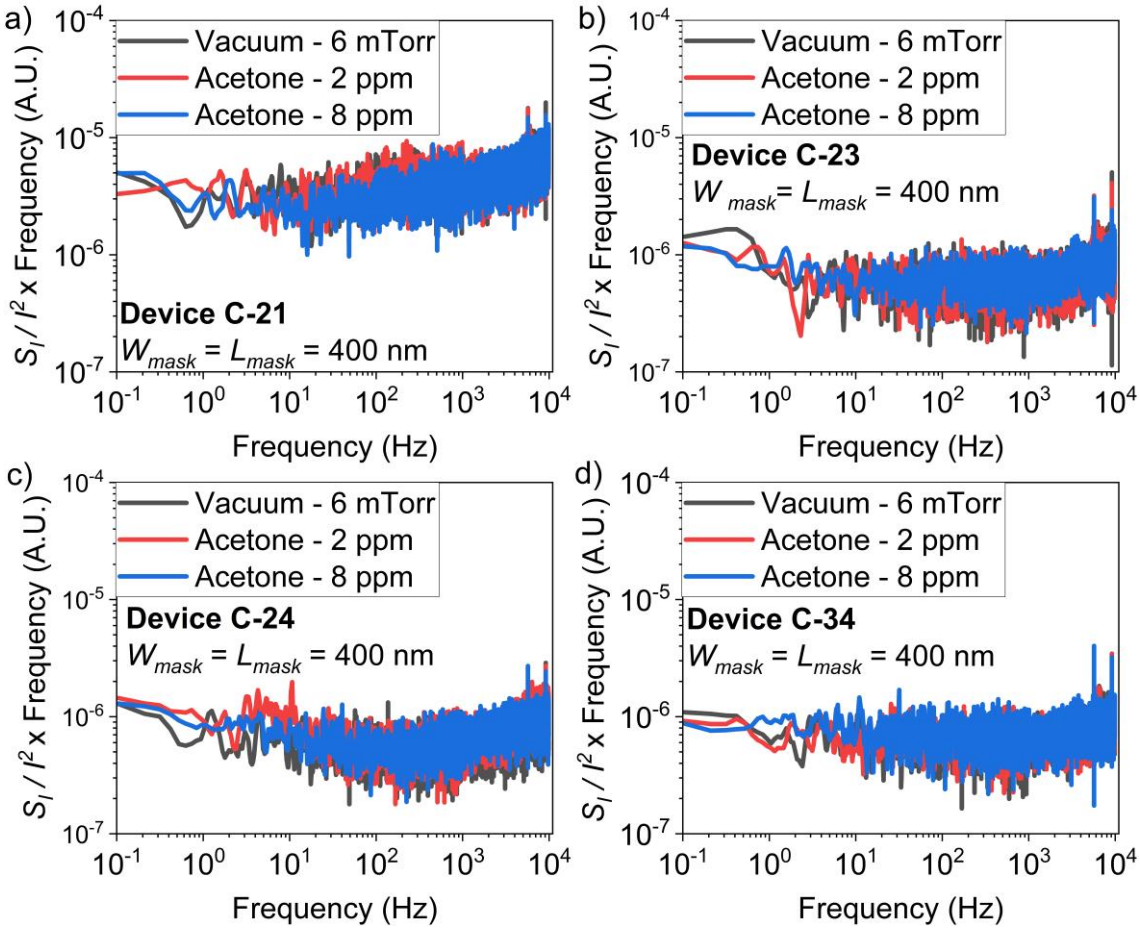

Figure 5.4 Product of the normalized power spectral density (S_I/I^2) by frequency as a function of frequency of tin-functionalized suspended GNR with MGM contacts in a vacuum (6 mTorr) and exposed to acetone diluted in nitrogen at concentrations of 2 ppm (154 Torr) and 8 ppm (600 Torr).

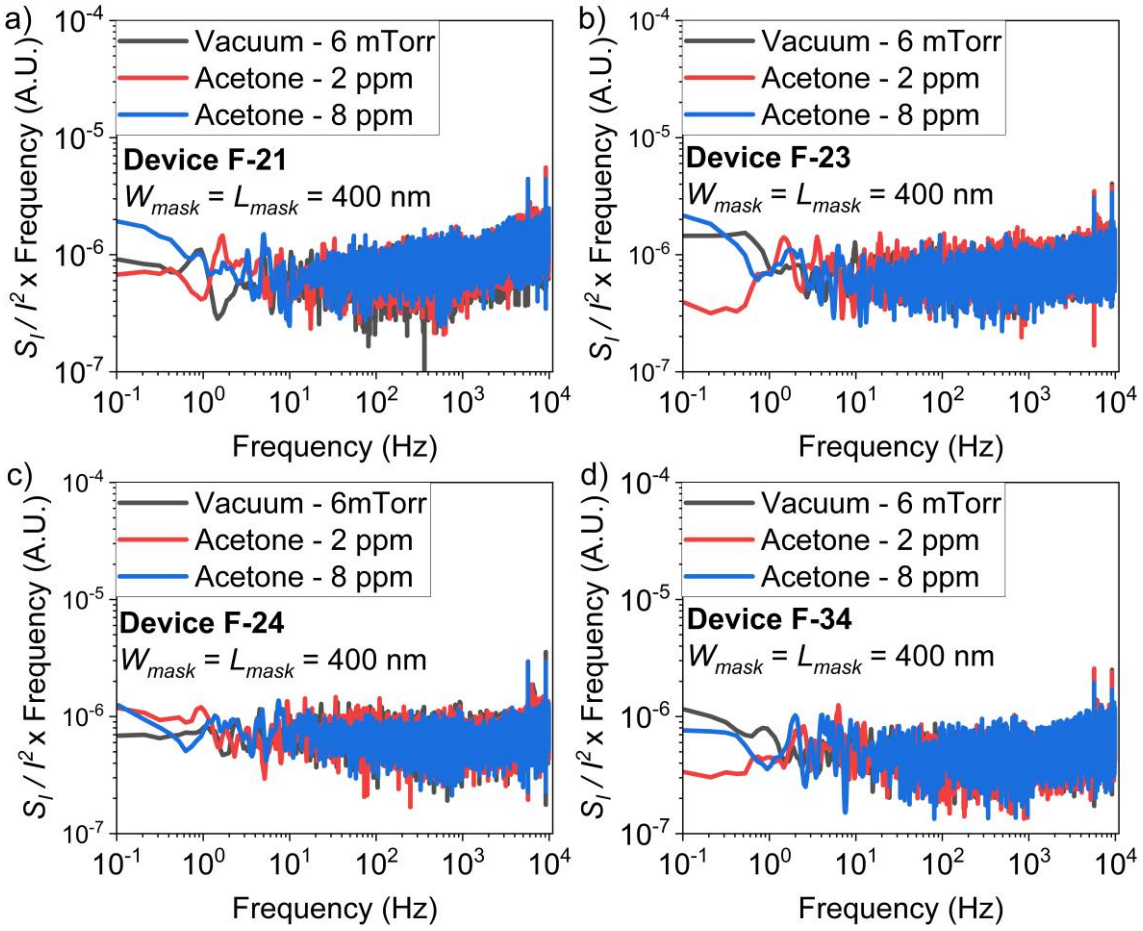

Figure 5.5 Product of the normalized power spectral density (S_I/I^2) by frequency as a function of frequency of suspended GNR with MGM contacts in a vacuum (6 mTorr) and exposed to acetone diluted in nitrogen at concentrations of 2 ppm (154 Torr) and 8 ppm (600 Torr).

After the experiment with acetone, the chamber was once more evacuated and left in a vacuum at room temperature overnight (14 hours) and experiments with benzene were performed. Measurements in a vacuum were taken and benzene diluted in argon was introduced into the chamber at 100 SCCM until a pressure of 150 Torr. The gas cylinder used has benzene in a concentration of 508 ppm. Thus, at a pressure of 150 Torr, the final concentration was around 80 ppm. Figure 5.6 and Figure 5.7 show the results for tin-functionalized graphene and for pristine graphene, respectively. Once more there were no observable noise changes.

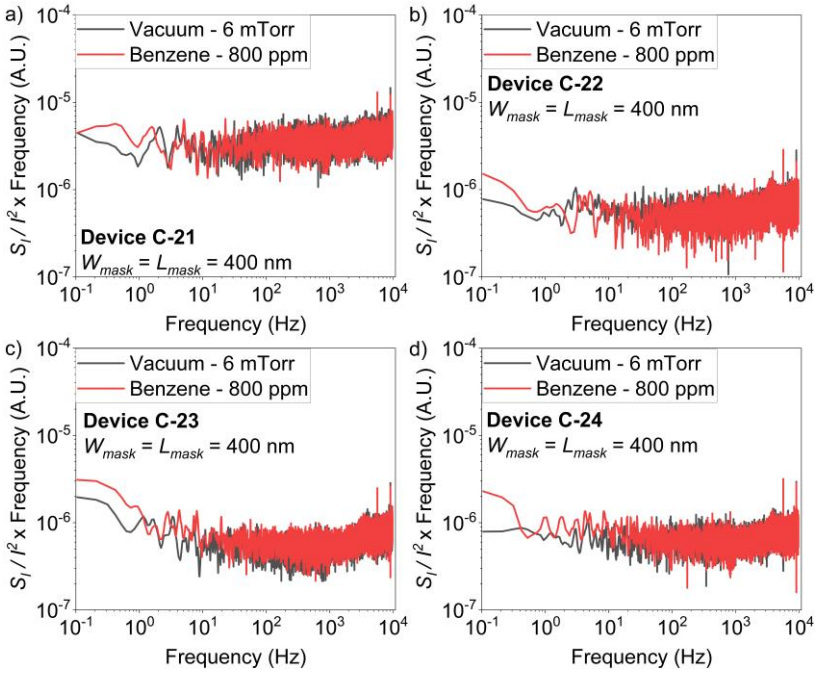

Figure 5.6 Product of the normalized power spectral density (S_I/I^2) and frequency as a function of frequency of tin-functionalized suspended GNR with MGM contacts in a vacuum and exposed to benzene diluted in argon at a concentrations of 800 ppm (300 Torr).

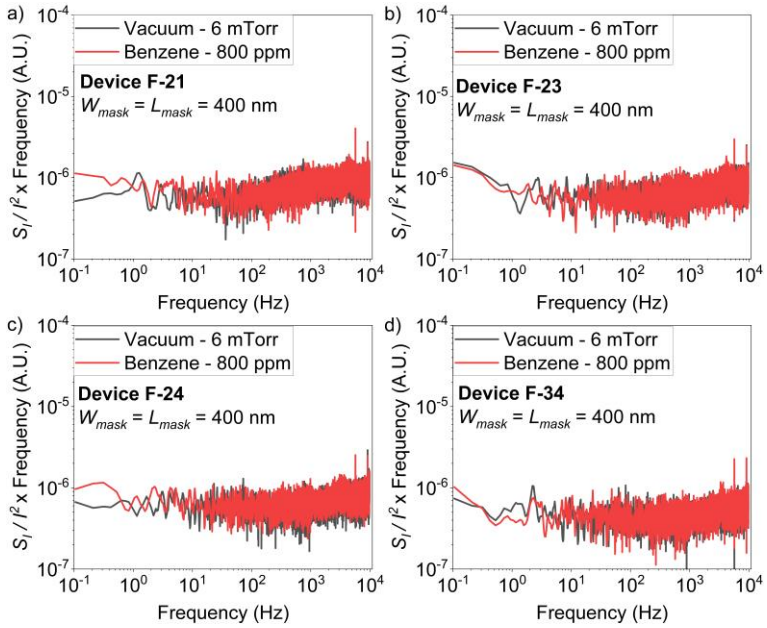

Figure 5.7 Product of the normalized power spectral density (S_I/I^2) and frequency as a function of frequency of suspended GNR with MGM contacts different devices in a vacuum and exposed to benzene diluted in argon at a concentrations of 800 ppm (300 Torr).

In the experiments with oxygen, pure gas with a purity of 99.999% was used. (gas cylinder with grade 2 provided by Unosanso Ltd). Measurements in a vacuum were taken, and oxygen was introduced until a pressure of 400 Torr. Figure 5.8 and Figure 5.9 show the plot of the normalized PSD x frequency in a vacuum and in the oxygen environment. One of the devices (Device C-21) showed a small peak in the normalized PSD at around 1 to 10 Hz (Figure 5.8 (a)), while no changes were observed in the other devices. This peak was caused by the appearance of RTS, as it can be confirmed by looking at the resistance time series in Figure 5.10. It is important to note that measurements were performed in series, and Device C-21 was the first device to be measured. There is already evidence from the experiments performed on the previous sample that the RTS disappears after some time. Therefore, one possible explanation for the lack of observation of RTS in the other devices is that the adsorption of O_2 molecules had already ceased when the measurements were performed. The devices that weren't functionalized with tin were the last ones to be measured. For that reason, it is unclear whether the tin had any effect.

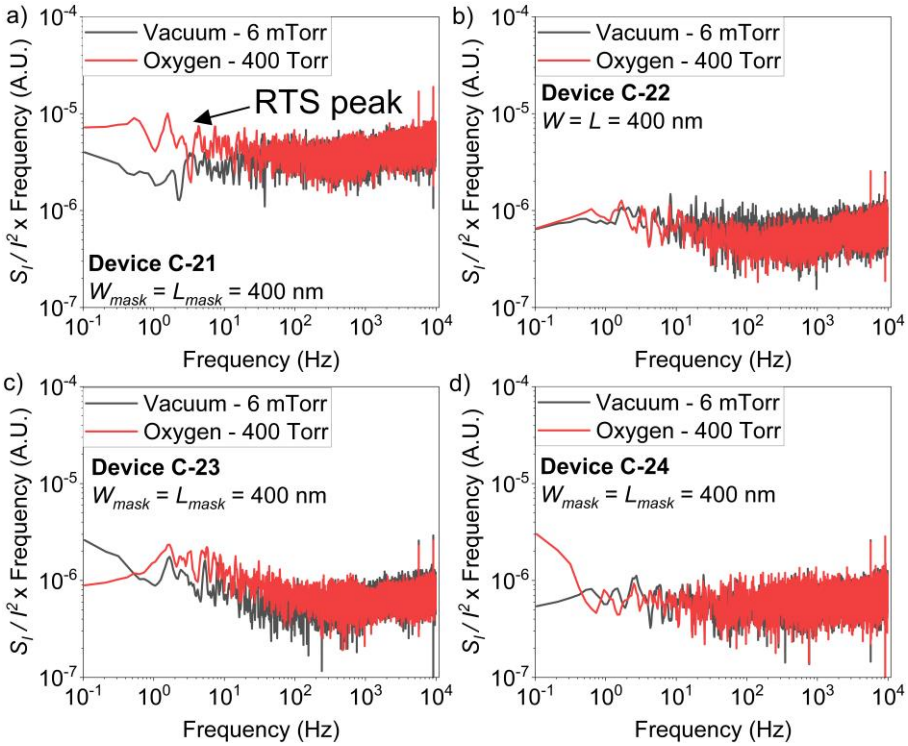

Figure 5.8 Product of the normalized power spectral density (S_I/I^2) and frequency as a function of frequency of tin-functionalized suspended GNR with MGM contacts in a vacuum (6 mTorr) and exposed to pure oxgen (400 Torr).

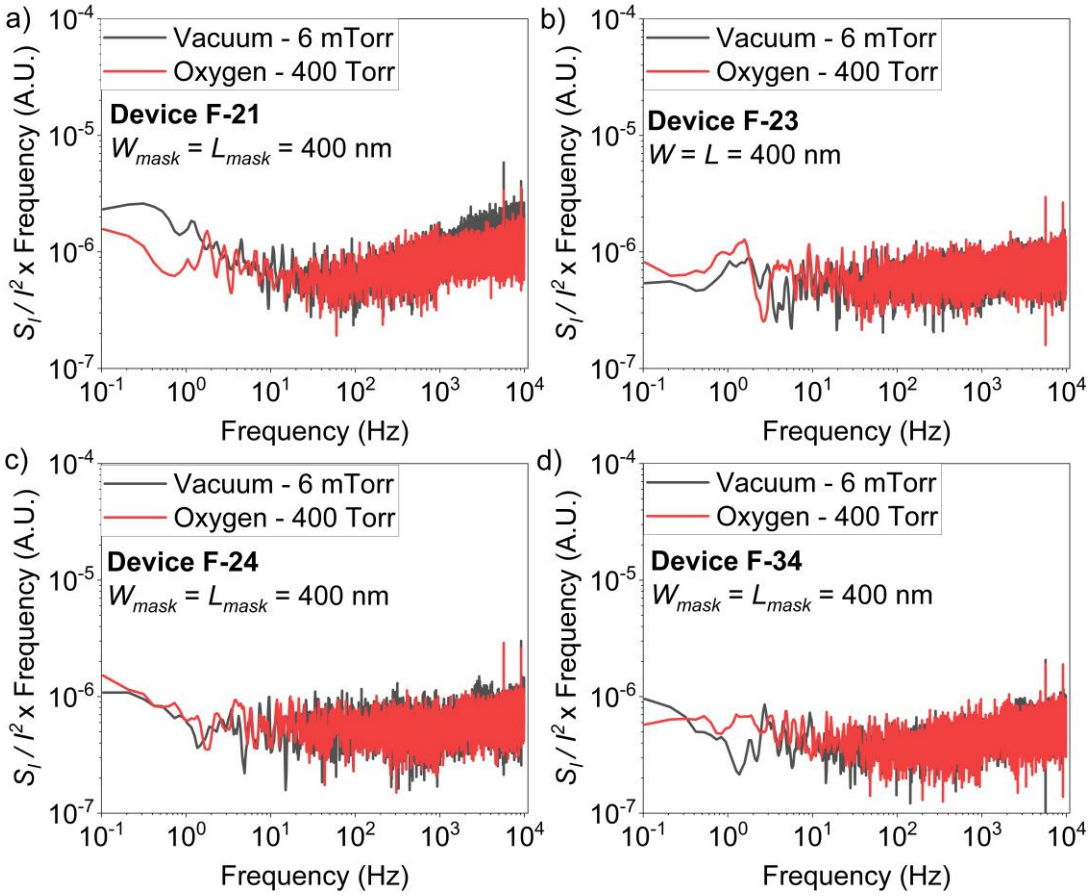

Figure 5.9 Product of the normalized power spectral density (S_I/I^2) and frequency as a function of frequency of tin-functionalized suspended GNR with MGM contacts in a vacuum (6 mTorr) and exposed to pure oxgen (400 Torr).

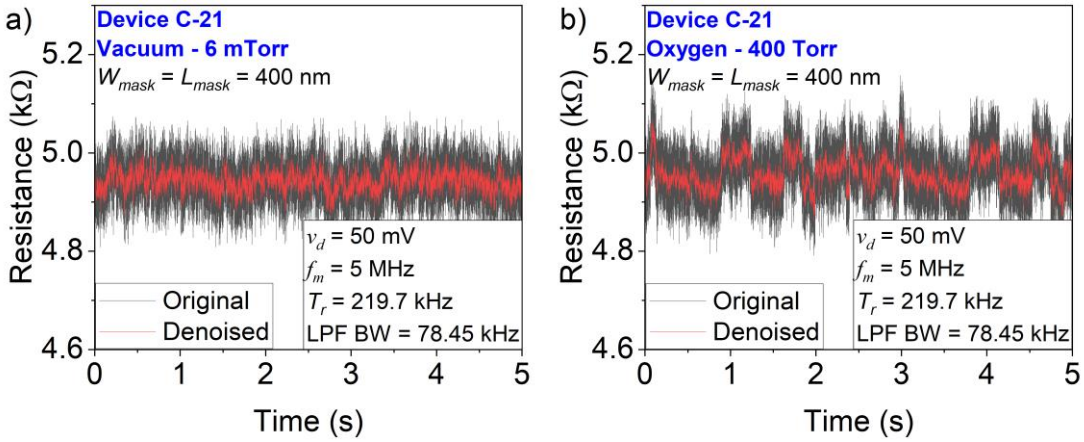

Figure 5.10 Section with 5 seconds of duration of the original and denoised resistance of Device-C21. (a) Measurement taken with the device in a vacuum. (b) Measurement taken with the device exposed to oxygen (400 Torr).

SEM images were taken after the experiments with gas. The images were taken after the experiments to avoid modification of the GNR properties by the electron beam. As shown in Figure 5.11, the lift-off of Device C-21 wasn't well succeeded. Because of this, the GNR has a triangular shape, with a base of around 100 nm. It can also be seen that there is a short circuit between the drain and the source. However, the contact between the metals isn't very good and conductance modulation of the graphene by the gate voltage can still be observed (Figure 5.12).

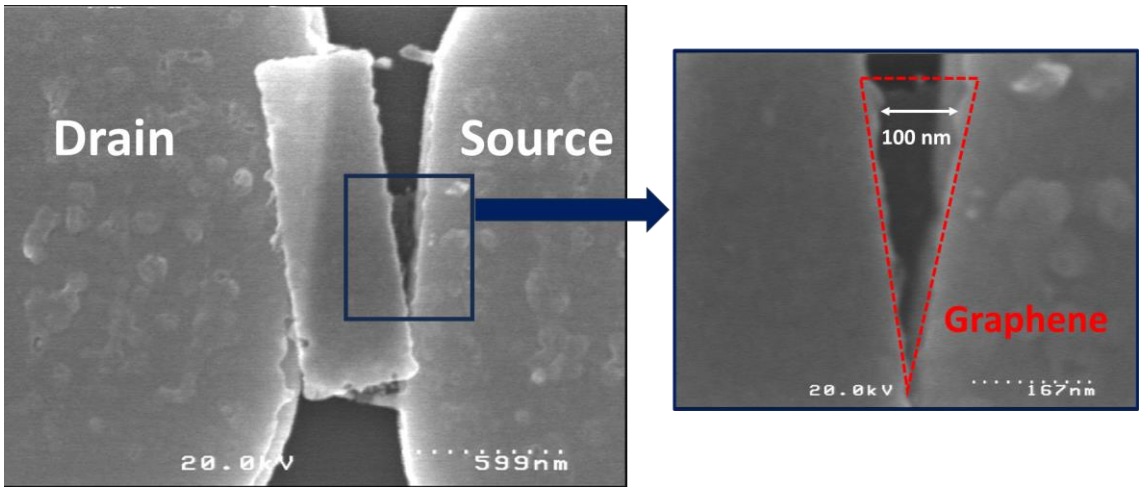

Figure 5.11 SEM Image of Device C-21, showing that the lift-off wasn't completely successful, but a small area of graphene in a triangular shape is exposed.

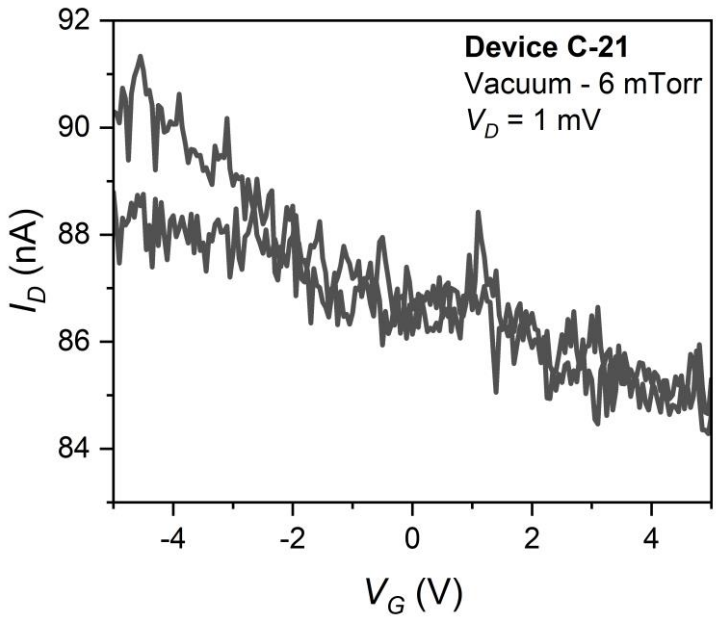

Figure 5.12 Transfer characteristic of Device C-21 in a vacuum.

This unexpected geometry of Device C-21 might explain why it has a larger noise than all other devices measured. Also, it can be said that one of the contacts is also suspended since there is graphene underneath the metal that wasn't properly removed during lift-off. This problem happened only with Device C-21. In all the other 7 devices, the lift-off was successful (Figure 5.13). There are at least three different reasons for Device C-21 to be the only one to show RTS with oxygen. The first possibility is that the RTS is caused by adsorption on the graphene underneath the suspended metal layer. The SEM images of the other devices show that overdevelopment of the bottom metal layer and small misalignments result in an area of the graphene that is supported on gold. Therefore, this hypothesis alone cannot explain why Device C-21 was the only one to show RTS with oxygen. A second hypothesis is that, as commented, the RTS stops after some time, and the RTS was observed in Device C-21 because it was the first device to be measured. A third possibility is that RTS can only be observed in smaller dimensions. The other devices all have a length of at least 300 nm, while the length of Device C-21 at the longest point is around 100 nm.

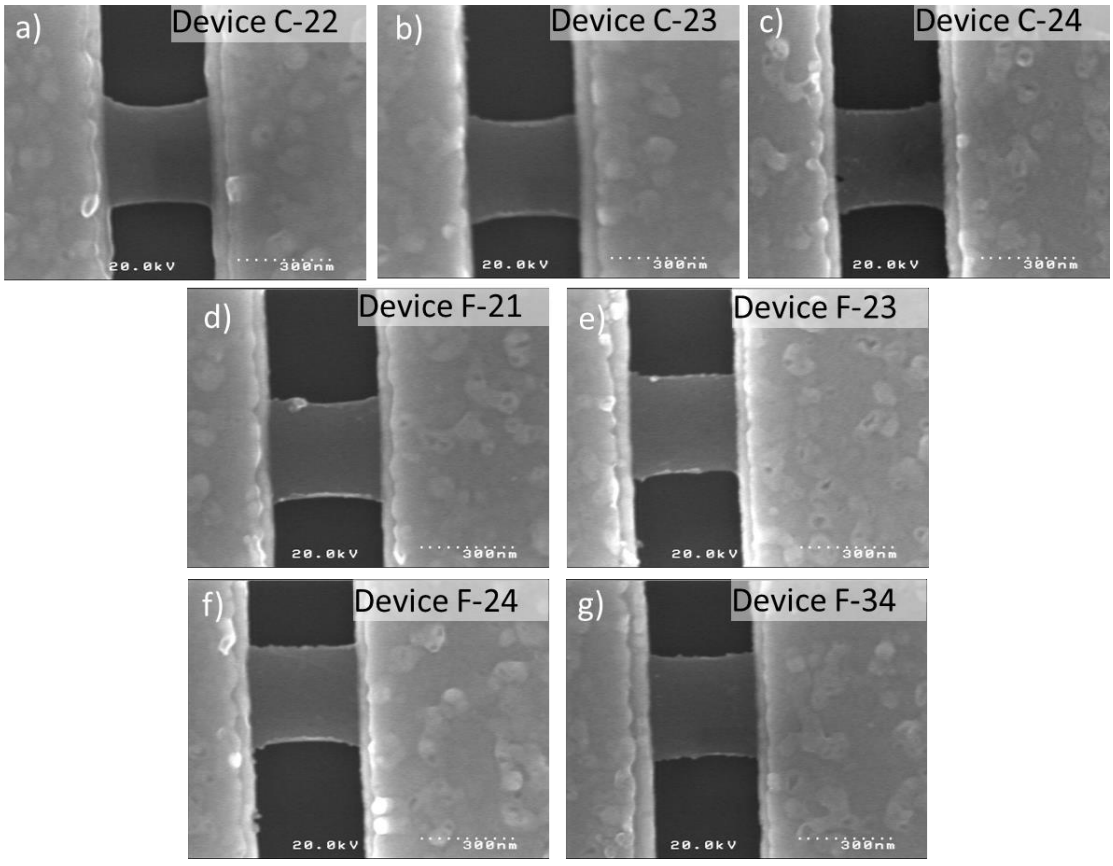

Figure 5.13 SEM images of MGM devices used in the experiments. (a) Device C-22. (b) Device C-23. (c) Device C-24. (d) Device F-21. (e) Device F-23. (f) Device F-24. (g) Device F-34.

In summary, 4 different gases were tested. Only oxygen caused changes in the noise and the appearance of RTS, if compared to the device's noise in a vacuum. Among the gases tested, oxygen has a large charge transfer from graphene. Benzene, for example has a charge transfer of 0.018 *e*, while oxygen has a charge transfer of -0.208 *e* [37]. Also, pure oxygen was used, while the other gases were diluted in an inert gas. Thus, their concentration was much smaller. Either way, it seems reasonable to investigate more the effect of oxygen.

5.3 Current Annealing and Oxygen Effect

The effect of oxygen was further investigated in a different device (Device C-42). This time, current annealing was used to clean the GNR. This device is one of the devices that were functionalized with tin. Current annealing was performed by varying the gate voltage between -5 V and + 5 V many times (Figure 5.14). Initially a V_D of 1 V was used (current around 200 μA). Since the CNP still wasn't very clear, a drain voltage of 2 V was applied (current around 240 μA). The CNP still wasn't visible, and a new annealing at 3 V was performed. This time, the drain current was around 80 nA, a large drop if compared to the previous cases. The resistance increased from the original 7 kΩ to 38 kΩ. This high increase in the resistance is an indication that the GNR started to break due to high temperatures prevenient from the current annealing. After the current annealing, the device was left in a vacuum for 3 days at room temperature. As Figure 5.15 shows, the cleaning was successful. While the CNP isn't visible, before the annealing the current would reduce with V_G. This means that the CNP is larger than 5 V, and the device was originally p-doped. After the annealing, the drain current started to increase with V_G. Therefore, the CNP is lower than -5 V, and the device is n-doped.

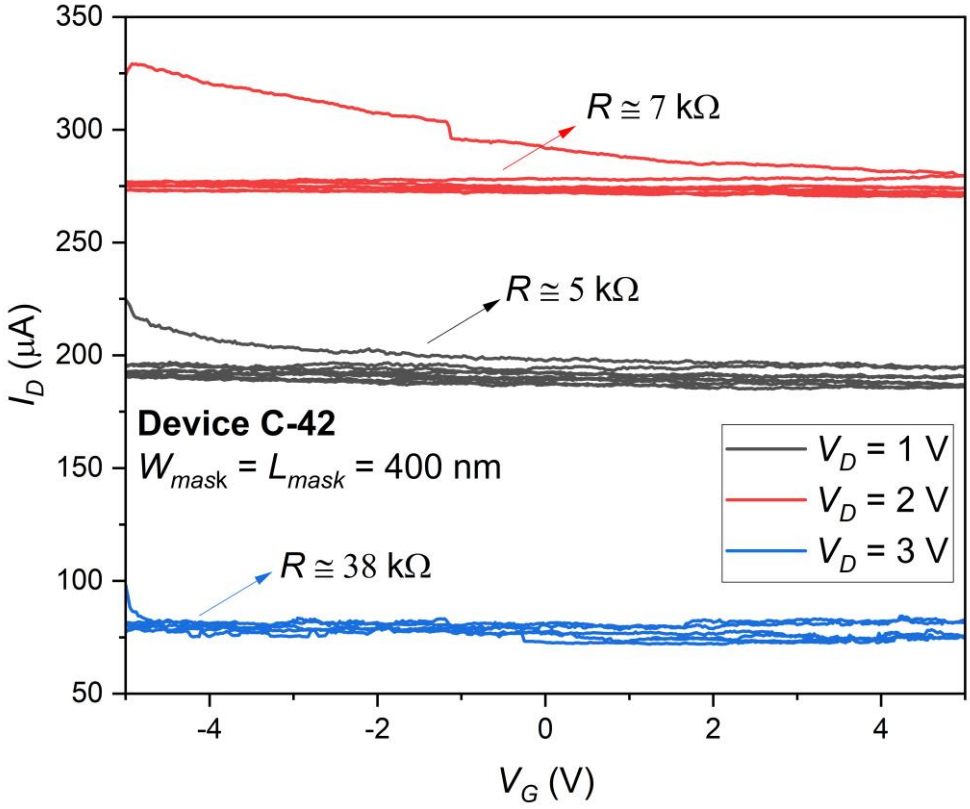

Figure 5.14 Current annealing of Device C-42.

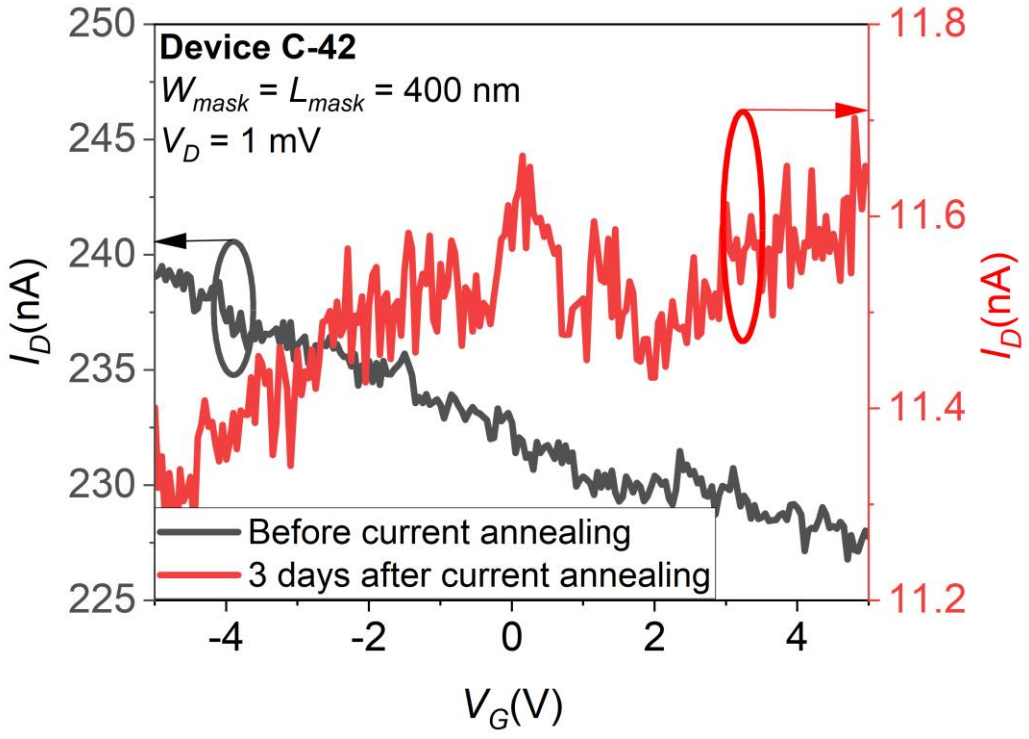

Figure 5.15 Transfer characteristic of Device C-42 before and after current annealing.

Experiments with oxygen were performed three days after the current annealing. The resistance was measured with the LIA in a vacuum for 30 seconds with the following parameters: f_m = 5 MHz, Tr = 219.7 kHz, LPF BW = 78.45 kHz, and v_d = 10 mV. Then, oxygen was introduced until a pressure of 400 Torr. Figure 5.16(a) shows the PSD x frequency plot in a vacuum and with oxygen. There is a strong response, and the noise after oxygen introduction is much higher than in a vacuum. Especially between 1 and 10 Hz. After this experiment, the chamber was evacuated, and the device was left in a vacuum at room temperature. Four hours later the experiment was repeated. The peak in the PSD disappeared in a vacuum. After oxygen was introduced again a large peak (larger than before) appeared, and the noise was higher than in a vacuum up to 100 Hz (Figure 5.16(b)). The resistance time series confirms that the bulges are caused by the appearance of RTS (Figure 5.17). The large resistance increase observed during the annealing indicates that the device had started to break, and its effective width was probably much smaller than designed. The small width might've made the device more sensitive to oxygen, and the noise increase was easily observed. Also, reproducibility was confirmed by just leaving the device in a vacuum for 4 hours, though the RTS time parameters are different. A possible reason for this is that the GNR was slowly breaking, thus changing the RTS observed. After these experiments, the chamber was evacuated, and the sample was left in a vacuum at room temperature. Unfortunately, the device was already broken the next day. Even though the device was fine for 3 days, it broke soon after the experiments with oxygen. This gives rise to the hypothesis that the chemisorption of oxygen on defects may be etching the graphene. This hypothesis is supported by some theoretical works [76] [77] [78], though more experimental investigation is needed.

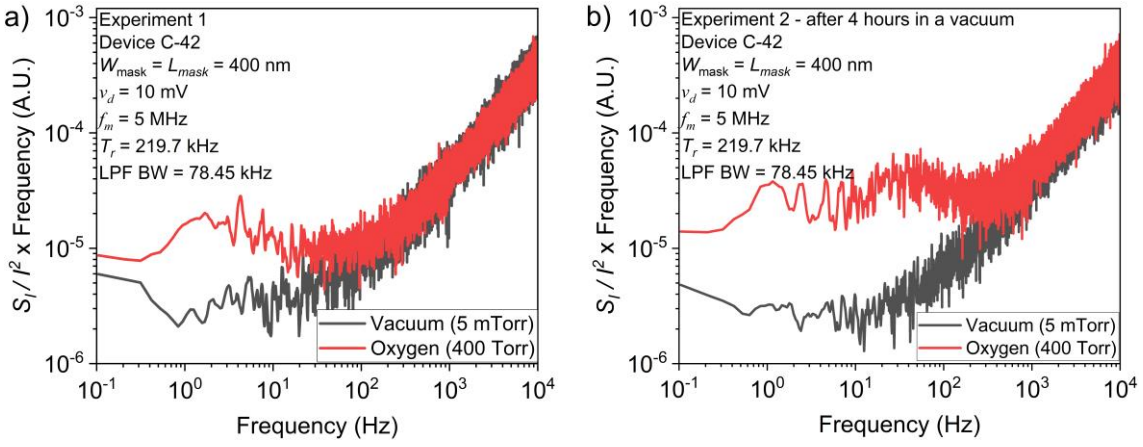

Figure 5.16 Product between the PSD and the frequency of device C-42 in a vacuum and in an oxygen environment. (a) First experiment. (b) Second experiment.

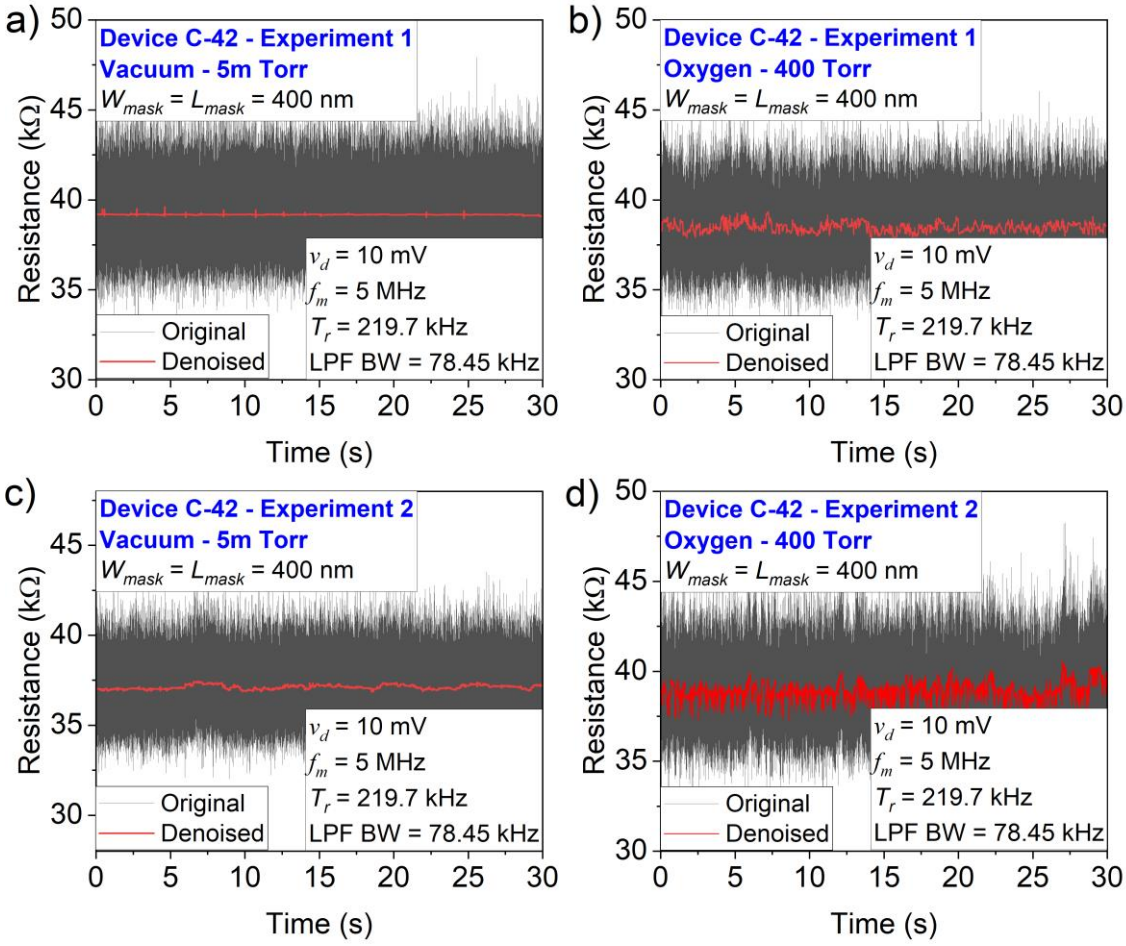

Figure 5.17 Resistance time series of Device C-42. (a) Vacuum - experiment 1. (b) Oxygen - experiment 1. (c) Vacuum - experiment 2. (d) Oxygen - experiment 2.

Lastly, the influence of current annealing on the functionalized device with W_{mask} = L_{mask} = 1 µm (Device C-52) was investigated through SEM images. This device was chosen because it is the largest device in the sample, and its observation on SEM would be easier. Current annealing was performed in a vacuum by applying a drain voltage of 2 V ($I_D \approx 320$ µA). Figure 5.18 shows the transfer characteristics before and after the current annealing. Though the CNP still is not visible, the curve shape indicates the CNP is likely near 7 V.

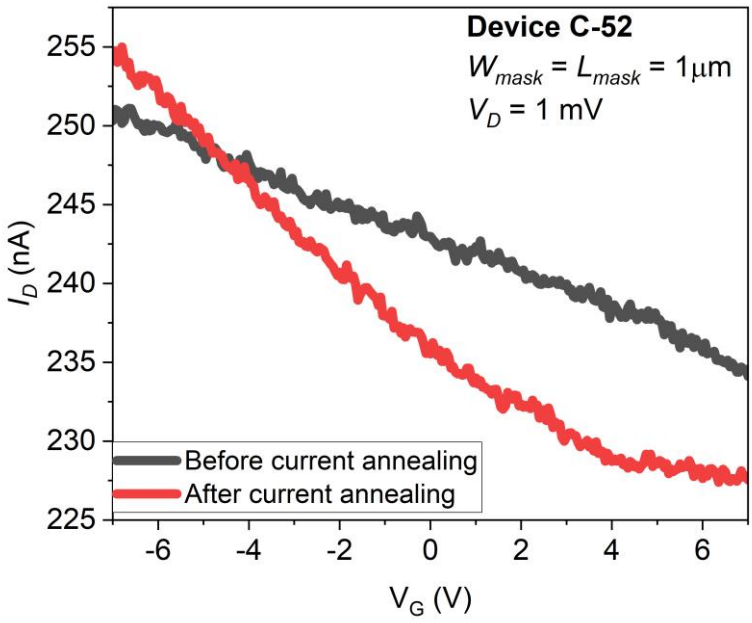

Figure 5.18 Transfer characteristic of Device C-52 before and after current annealing.

SEM images were taken before and after the current annealing. As shown in Figure 5.19 (a), the tin deposition created a tin film that covers almost the entirety of the GNR. This is not ideal, because the effect of gases on the graphene will be diminished, and this might be the reason the tin-functionalized devices didn't show response to most of the gases studied. After the current annealing (Figure 5.19(b)), it can be noted that the film in the center of the device started to become darker than the region near the contacts. When current annealing is performed there is a gradient of temperature. The center has the highest temperature and can achieve temperatures as high as 700 K [70]. The temperature is much smaller on the sides because the metal contacts work as a heat sink. Therefore, the darker color near the center after the annealing is due to the diffusion of Tin from the center (hot places) to the side of the GNR (colder places).

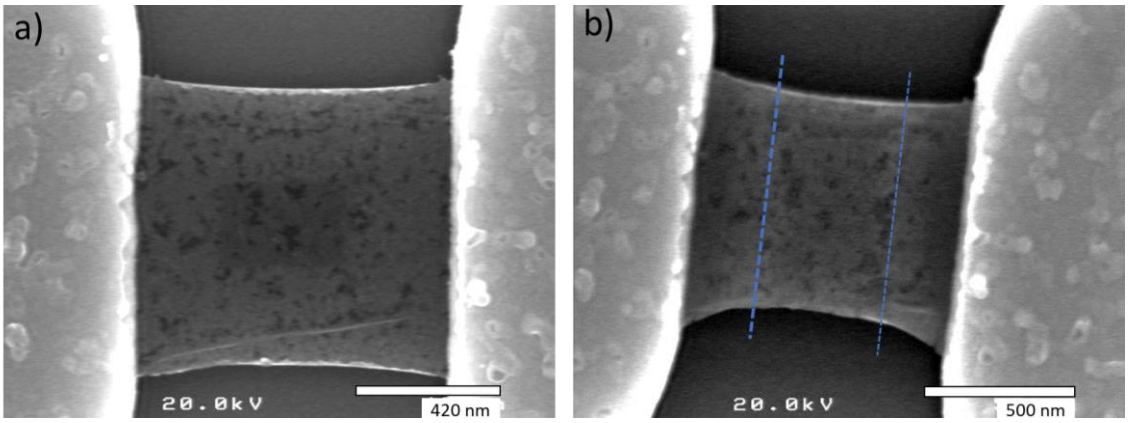

Figure 5.19 SEM images of Device C-52. (a) Before current annealing. (b) After current annealing.

In summary, no clear differences were observed in the effect of different gases on the devices PSD between suspended CVD graphene and tin-functionalized graphene. However, these are very preliminary investigations, and nanoparticles on suspended graphene still need more study, including how the size and clustering of nanoparticles affect the graphene response to gas molecules. The effect of BHF (commonly used to suspend graphene) on the nanoparticles also needs more investigation. Tin in particular can react with hydrofluoric acid (HF) to form tin(II) fluoride (SnF_2) and hydrogen (H_2). If that is the case, it seems unlikely that the response of tin-functionalized supported and suspended graphene would be the same. Lastly, there is evidence that the width of the GNR must be considered when trying to observe the RTS caused by oxygen. The reason for that is that as the width gets smaller, the influence of oxygen adsorption on the total resistance of the GNR is higher, the width dependence may be due to the closing of a conduction channel. Another possible explanation is that the RTS is caused by O_2 adsorption on dangling bonds of the GNR edges. Since edge effects are more pronounced at smaller W, this would also explain the width dependence.

Chapter 6
Conclusions and Future Work

Two samples with different CVD GNR structures were successfully fabricated. Due to the fast diffusion of BHF, the first sample has suspended metal contacts, which resulted in the collapse of many devices. Nevertheless, RTS caused by oxygen was observed in two devices ($W = L = 200$ nm). One device demonstrated anomalous RTS behavior, where the RTS is only present at some periods. By considering only these periods, dwell times of 2 ms (high-resistance state) and 2.9 ms (low-resistance state) were extracted. The other device seemed to show regular RTS behavior, but after statistical analysis, it was noticed that the dwell time in the high-resistance state increased from 6 to 35 ms during the measurement. This shows that the RTS caused by oxygen has a transient behavior, likely caused by the dynamics of oxygen molecules during adsorption, and care must be taken when using the spectrum for identification purposes.

The second sample was fabricated using a metal-graphene-metal contact structure. With this, the metal contacts are not suspended anymore, and the chance of collapse is reduced. Another advantage is that there is no graphene under the metal contacts, such that there is more confidence that any observed effect is due to adsorption on the graphene channel. Also, some devices were functionalized with tin to verify if nanoparticles can work as adsorption sites to enhance sensitivity. Due to lift-off problems, the 200 nm devices could not be used. Instead, the measurements were performed on devices with 400 nm.

Experiments with ethanol, acetone, benzene, and oxygen were performed. Only for oxygen, there was a change in the low-frequency noise if compared to measurements in a vacuum. RTS with oxygen was observed in different devices through bulges in the low-frequency spectrum at around 1-100 Hz. In one of the cases, the device (Device C-21) has an unexpected triangular shape due to lift-off problems. At the longest point, this device has only 100 nm of length, much smaller than the planned 400 nm. In a different device (Device C-42), current annealing was performed before the measurements. A high increase in resistance was observed after current annealing, indicating that the GNR started to break due to annealing. Experiments with oxygen were performed. Again RTS (and its resulting bulge in the PSD) were observed when the GNR was exposed to graphene. Remarkably, the PSD could recover after 4 hours in a vacuum, and RTS appeared again when the devices were exposed to oxygen once more. Though it could not be confirmed by SEM images, it is likely that the device width was already smaller than

the intended 400 nm. Therefore, a narrow width might be essential to observe the RTS caused by oxygen. Another very important point is that this device broke the next day, giving rise to the hypothesis that oxygen may be adsorbing graphene defects, and creating new defects in this process. Thus, helping the nanoribbon to break.

Unfortunately, the effect of tin could not be confirmed, though it was confirmed through SEM images that the tin formed a roughly uniform film on the graphene. Because of this, the gas molecules could not interact directly with graphene, reducing sensitivity and selectivity. After the current annealing diffusion of tin from the center of the GNR (hottest spot during annealing) to the sides was confirmed, but the effect of annealing on suspended tin-functionalized GNR still needs more investigation.

Oxygen has a relatively high transfer to graphene and this larger effect might be the reason it was the only gas to show a response. In reference [26], exfoliated graphene supported on SiO_2 was used to differentiate some vapor gases through low-frequency noise spectra. Therefore, it is possible that if very clean, defectless graphene is used, response from the other 3 gases could be observed. Another factor that needs more study is the effect of the substrate. Therefore, a comparative study between exfoliated and CVD graphene as well as suspended and supported graphene is necessary for future work.

It was confirmed in different devices with different structures that oxygen causes RTS on suspended CVD graphene. Oxygen is the second most abundant gas in our atmosphere. Therefore, it is expected that graphene-based gas sensors will be in contact with this gas. In this work, the effect of oxygen was observed while the gas was being introduced, and at a constant pressure of 400 Torr. Because of this, it is unclear whether the RTS in the suspended GNR is related to the number of molecules interacting with graphene or to the exposure time. Therefore, more experiments with different pressures and time scales are necessary. In addition, the devices' size most likely plays a role, with smaller devices being more sensitive to the RTS. Therefore, is necessary to investigate the effect of oxygen on smaller devices. Lastly, the mechanism responsible for the RTS still needs more investigation, and theoretical work is necessary to complement the experimental work presented. More rigorous studies on these topics could lead to the device's optimization, such that variability among devices can be reduced and sensitivity towards other gases can be increased.

Appendix A – Fabrication Runsheet of Suspended Graphene Nanoribbon with Suspended Contacts

Dicing and cleaning	Spin-coating: • PMMA 4000 RPM, 60 seconds • Hot plate: 180 ºC, 5 minutes Dicing: 15 x 20 mm size samples Back oxide etching: CF_4 RIE: 20 SCCM, 4 Pa, 100 W, 9 minutes. Cleaning: • Hot acetone (60 ºC) for 30 minutes • IPA for 2 minutes • Dry in air
Annealing	Ar + H_2(10%) atmosphere: 0.5 L/min, 300ºC
Litography (Adress pattern)	Cleaning: • Acetone: 5 minutes • IPA: 5 minutes Spin-coating: • MMA 2000 RPM, 60 seconds • Hot plate: 180 ºC, 5 minutes • PMMA 4000 RPM, 60 seconds • Hot plate: 180 ºC, 5 minutes EBL: • Current: 1 nA • Dose time: 0.21 μs Development: • MIBK:IPA 1:1, 40 seconds • IPA: 30 seconds
Metal deposition	RIE: O_2, 10 SCCM, 4 Pa, 30 W, 10 seconds PVD (electron beam thermal evaporator): • Chromium: 5 nm • Gold: 75 nm Lift-off: Acetone (60ºC), 30 minutes

Litography (contacts)	Cleaning: • Acetone: 5 minutes • IPA: 5 minutes Spin-coating: • AR-P 6200 4000 RPM, 60 seconds • Hot plate: 150 ºC, 1 minutes EBL: • Current: 250 nA • Dose time: 0.52 µs Development: • Developer AR 600-546: 50 seconds • DIW: 30 seconds
Metal deposition	PVD (electron beam thermal evaporator): • Chromium: 5 nm • Gold: 25 nm Lift-off: remover AR 600-71(80ºC), 5 minutes
Litography (GNR definition)	Spin-coating: • Hot plate: 180 ºC, 5 minutes • PMMA: 4000 RPM, 60 seconds • Hot plate: 180 ºC, 5 minutes • AR-N 7520.07 4000 RPM, 60 seconds • Hot plate: 85 ºC, 1 minute EBL: • Current: 250 nA • Dose time: 0.4 µs Development: • Developer AR 300-47: 50 seconds • DIW 30 seconds • Hot plate: 85 ºC, 1 minute RIE: O_2, 10 SCCM, 4 Pa, 35 W, 140 seconds. Resist removal: • Acetone: 5 minutes • IPA: 5 minutes
Annealing	Ar + H_2(10%) atmosphere: 0.5 L/min, 300ºC
GNR suspension	BHF: 45 seconds + DIW: 20 seconds (three times) Supercritical dry: IPA + CO_2, 14 MPa, 50 minutes

Appendix B – Fabrication Runsheet of Suspended Graphene Nanoribbon with Metal-Graphene-Metal Contacts

Dicing and cleaning	Spin-coating: • PMMA 4000 RPM, 60 seconds • Hot plate: 180 ºC, 5 minutes Dicing: 15 x 20 mm size samples Back oxide etching: CF_4 RIE: 20 SCCM, 4 Pa, 100 W, 9 minutes. Piranha cleaning: • 50 ml H_2O_2 + 50 ml of H_2SO_4: 15 minutes
Annealing	Ar + H_2(10%) atmosphere: 0.5 L/min, 300ºC
Litography (Adress pattern)	Cleaning: • Acetone: 5 minutes • IPA: 5 minutes Spin-coating: • AR-P 6200.09 4000 RPM, 60 seconds • Hot plate: 150 ºC, 1 minutes • AR-P 6200.09 4000 RPM, 60 seconds • Hot plate: 150 ºC, 1 minutes EBL: • Current: 250 pA • Dose time: 0.52 µs Development: • Developer AR 600-546: 90 seconds • Stopper AR 600-60: 30 seconds • DIW: 30 seconds • Hot plate: 130 ºC, 30 seconds
Metal deposition	RIE: CF_4, 20 SCCM, 4 Pa, 100 W, 96 seconds PVD (electron beam thermal evaporator): • Chromium: 5 nm • Gold: 75 nm Lift-off: Remover AR 600-71 (60ºC), 30 minutes RIE: O_2, 4 Pa, 30 W, 25 seconds

Graphene transfer	Copper foil + graphene coating: • PMMA 4000 RPM, 60 seconds • Hot plate: 150 ºC, 2 minutes Back side etching: • RIE: O_2, 10 SCCM, 4 Pa, 30 W, 25 seconds Copper etching: • Ammonium persulfate for more than 4 hours Transfer to SiO_2/Si substrate: • Transfer PMMA/graphene to DIW (3 times) • Manually pick PMMA/Graphene with the SiO2/Si substrate 3 hours wait Hot plate baking: 2 minutes at 200 ºC 2 hours wait PMMA removal with acetone
Annealing	Ar + H_2(10%) atmosphere: 0.5 L/min, 300ºC
Litography (contacts)	Cleaning: • Acetone: 5 minutes • IPA: 5 minutes Spin-coating: • AR-P 6200.09 4000 RPM, 60 seconds • Hot plate: 150 ºC, 1 minutes EBL: • Current: 250 nA • Dose time: 0.52 µs Development: • Developer AR 600-546: 90 seconds • Stoper AR 600-60: 30 seconds • DIW: 30 seconds • Hot plate: 130 ºC, 30 seconds
Metal deposition	PVD (electron beam thermal evaporator): • Chromium: 5 nm • Gold: 25 nm Lift-off: remover AR 600-71 (80ºC), 5 minutes

Litography (GNR definition)	Spin-coating: • Hot plate: 180 ºC, 5 minutes • PMMA: 4000 RPM, 60 seconds • Hot plate: 180 ºC, 5 minutes • AR-N 7520.07 4000 RPM, 60 seconds • Hot plate: 85 ºC, 1 minute EBL: • Current: 250 nA • Dose time: 0.4 μs Development: • Developer AR 300: 50 seconds • DIW 30 seconds • Hot plate: 85 ºC, 1 minute RIE: O_2, 10 SCCM, 4 Pa, 35 W, 140 seconds. Resist removal: • Acetone: 5 minutes • IPA: 5 minutes
Annealing	Ar + H_2(10%) atmosphere: 0.5 L/min, 300ºC
GNR suspension	BHF: 45 seconds DIW: 20 seconds (three times) Supercritical dry: IPA + CO_2, 14 MPa, 50 minutes

Appendix C – Wavelet Denoising

Wavelet transform and denoising is a very rich subject by itself. In this section, only the basics necessary to understand its application in this work are presented.

Like the short time Fourier transform, wavelet transform can give temporal and frequency information of a signal. To do so, the wavelet transform performs a 2-D mapping of the 1-D signal, parametrized by two parameters: scaling (s) and translation (τ). The continuous wavelet transform (CWT) of a signal x*(t)* is given by [79]:

$$CWT\ (s,\tau) = \frac{1}{\sqrt{s}} \int x(t) \Psi \left(\frac{t-\tau}{s} \right) dt, \qquad (C1)$$

where $\Psi(t)$ is called the mother wavelet and can have many forms. The main characteristic of mother wavelets is that they are localized in time and decay rapidly towards zero [80]. Table C1 shows some of the more common mother wavelets, though there are many more.

Wavelet name	Mathematical expression	Graph
Harr	$\Psi(t) = \begin{cases} 1, & 0 \le t \le 1/2 \\ -1, & 1/2 \le t < 1 \\ 0, & otherwise \end{cases}$	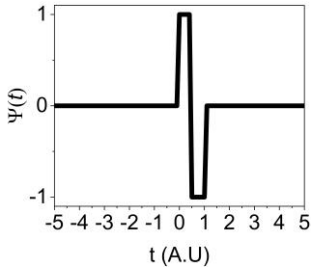
Shannon	$\Psi(t) = \frac{\sin(\pi t/2)}{\pi t/2} cos\left(\frac{3\pi t}{2}\right)$	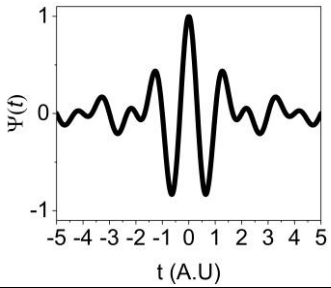
Morlet	$\Psi(t) = e^{i\omega_0 t} e^{-t^2/2}$	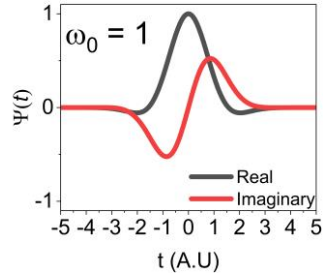

Table C1 Example of wavelets

From equation C1, one can notice that the CWT is given by the inner product between the signal and what are called baby wavelets (the mother wavelet translated by τ and scaled by s). This way, one can identify how much at a signal at a determined time is similar to the wavelet.

During denoising of a digital signal, the discrete version of wavelet transform is used. The discrete wavelet transform (DWT) is given by [81]:

$$DWT\ (l,m) = 2^{-\frac{l}{2}} \sum_{k} x[k]\, \Psi[2^{-l}k - m], \qquad (C2)$$

where, x[k] is a discrete signal, and Ψ[k] can be the discrete version of a continuous wavelet, though there are discrete wavelets without continuous counterpart. It is worth noticing that a wavelet can be viewed as a band-pass filter, and a simple way to implement the DWT is as a cascade of filters. In the first level, the signal passes through a low-pass filter (LPF) and through high-pass filter (HPF). The HPF is defined by the frequency response of the wavelet, and the LPF is its quadrature mirror filter [82]. In other words, the two filters complement each other. The second level of coefficients is obtained by applying a LPF and a HPF once again in the coefficients obtained from the LPF of the previous level. This process can be repeated, and the number of levels is limited only by the length of the signal. A schematic of the process is shown in Figure C1.

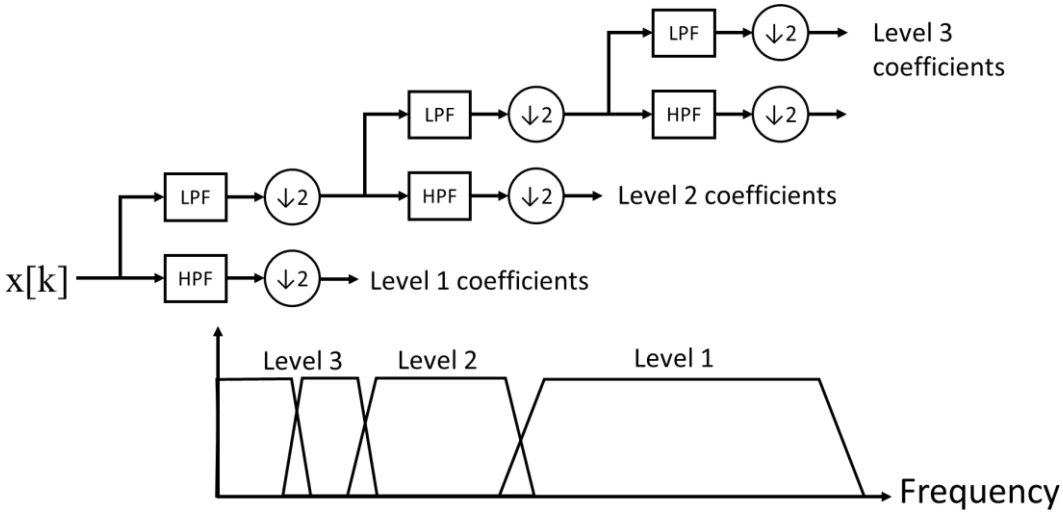

Figure C1 Schematic of the multidimensional analysis by cascading filters (adapted from [82]).

After the DWT is applied, a threshold can be used on the coefficients, and the denoised signal is obtained after applying the inverse DWT [82]. A hard threshold means that only coefficients above the threshold are kept, while the coefficients below it become 0. In a soft threshold, the coefficients continuously shrink when they are below the threshold. In this work, the resistance time-series were denoised using a Daubechies wavelet level 1 (equivalent to the Harr wavelet). As shown in Table C1, the Harr wavelet has a very similar shape to RTS, and that is the reason it was chosen. The denoising was performed down to level 19, through the function "wdenoise" from the software MATLAB. A universal threshold was chosen, using a soft threshold rule. A universal threshold is determined based on a Gaussian noise and is given by $\sigma_{std}\sqrt{2\log(N_s)}$, where σ_{std} is the estimated standard deviation of the Gaussian noise, and N_s is the number of samples of the signal [82]. There are many possible strategies for choosing the threshold, but further investigation on this topic goes beyond the scope of this work. The section of the MATLAB code implementing the denoising is shown below.

```
%R_M: Original resistance vector
%R_wd: Resistance vector after denoising
R_wd =
wdenoise(R_M,19,Wavelet="db1",NoiseEstimate="LevelIndependent",DenoisingMetho
d = "UniversalThreshold", ThresholdRule = "Soft");
```

Figure C2 shows a section of resistance time series of two devices. It becomes clear that the denoising removes most of the high frequency noise, while preserving the sharp transitions of the RTS, which wouldn't be possible with a simple low-pass filter. It also makes the two peaks in the histogram from the RTS more apparent and easier to identify (Figure C3).

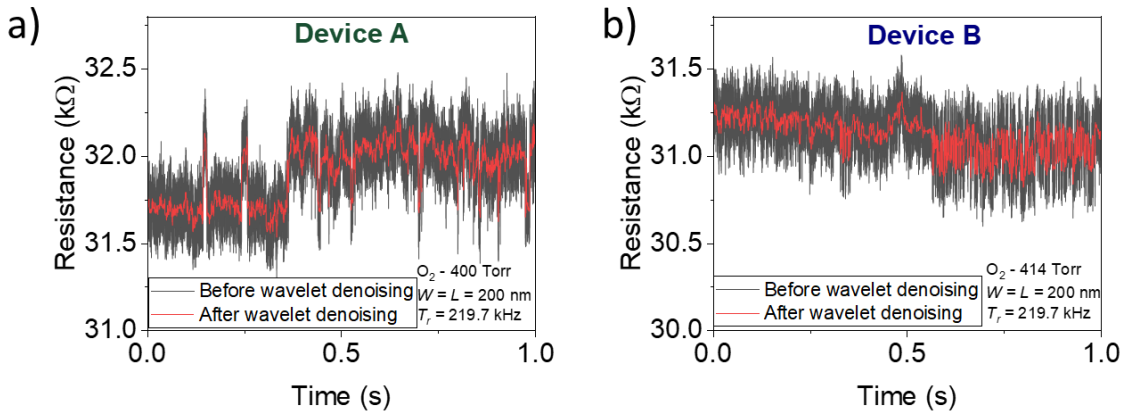

Figure C2 Resistance time series before and after wavelet denoising. (a) Device A. (b) Device B.

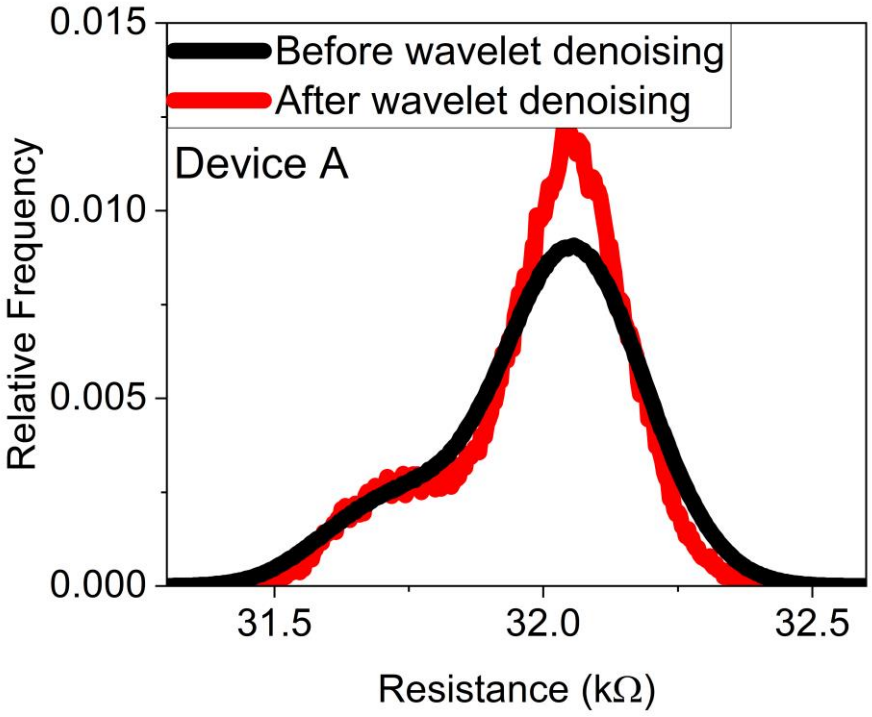

Figure C3 Resistance histogram of Device A before and after wavelet denoising.

Appendix D – Raw Electrical Current Data from Chapter 4.

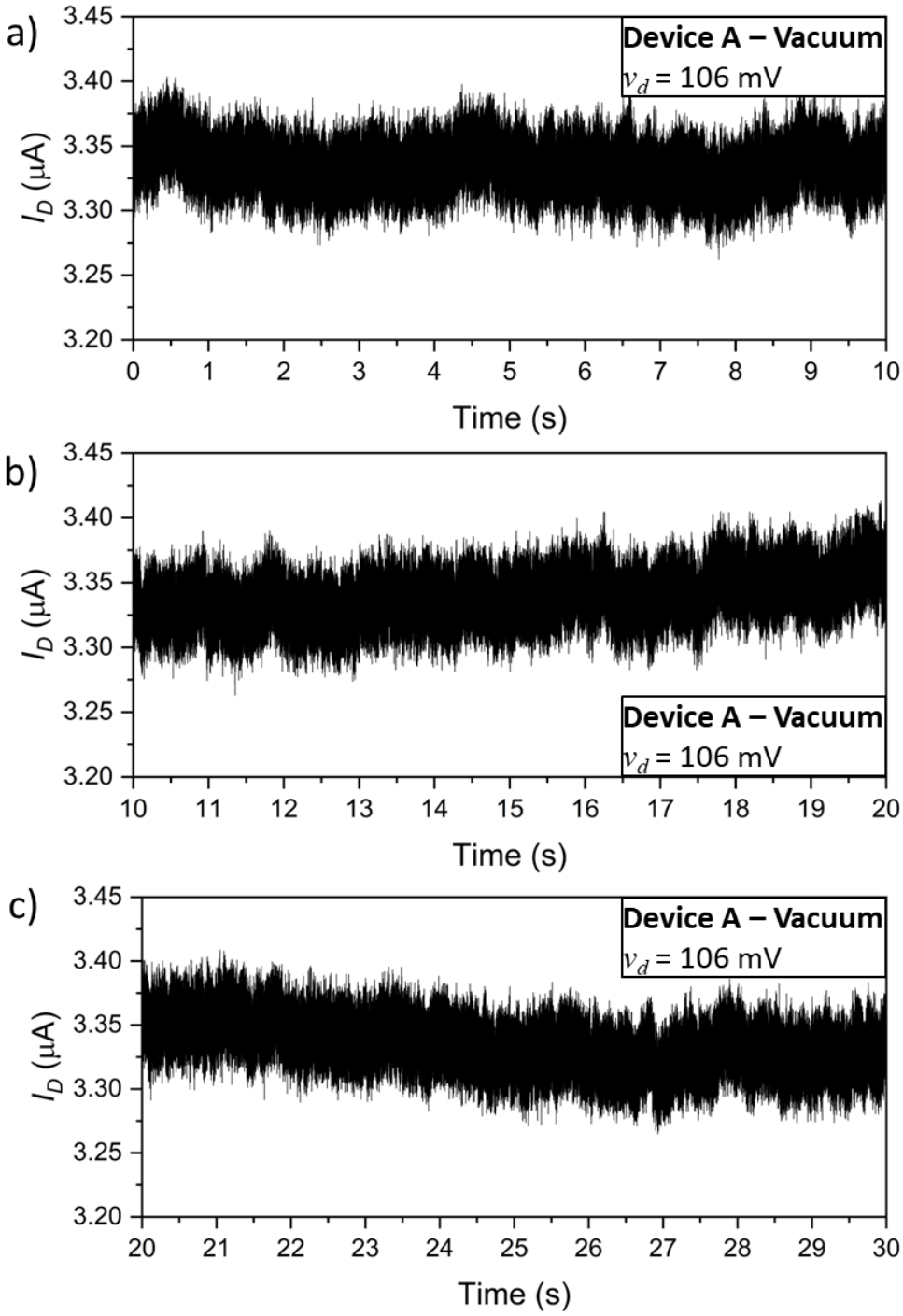

Figure D1 Current of Device A (suspended contact) in a vacuum (6 mTorr). Sections from 0 to 10 seconds (a), 10 to 20 seconds (b), and 20 to 30 seconds (c).

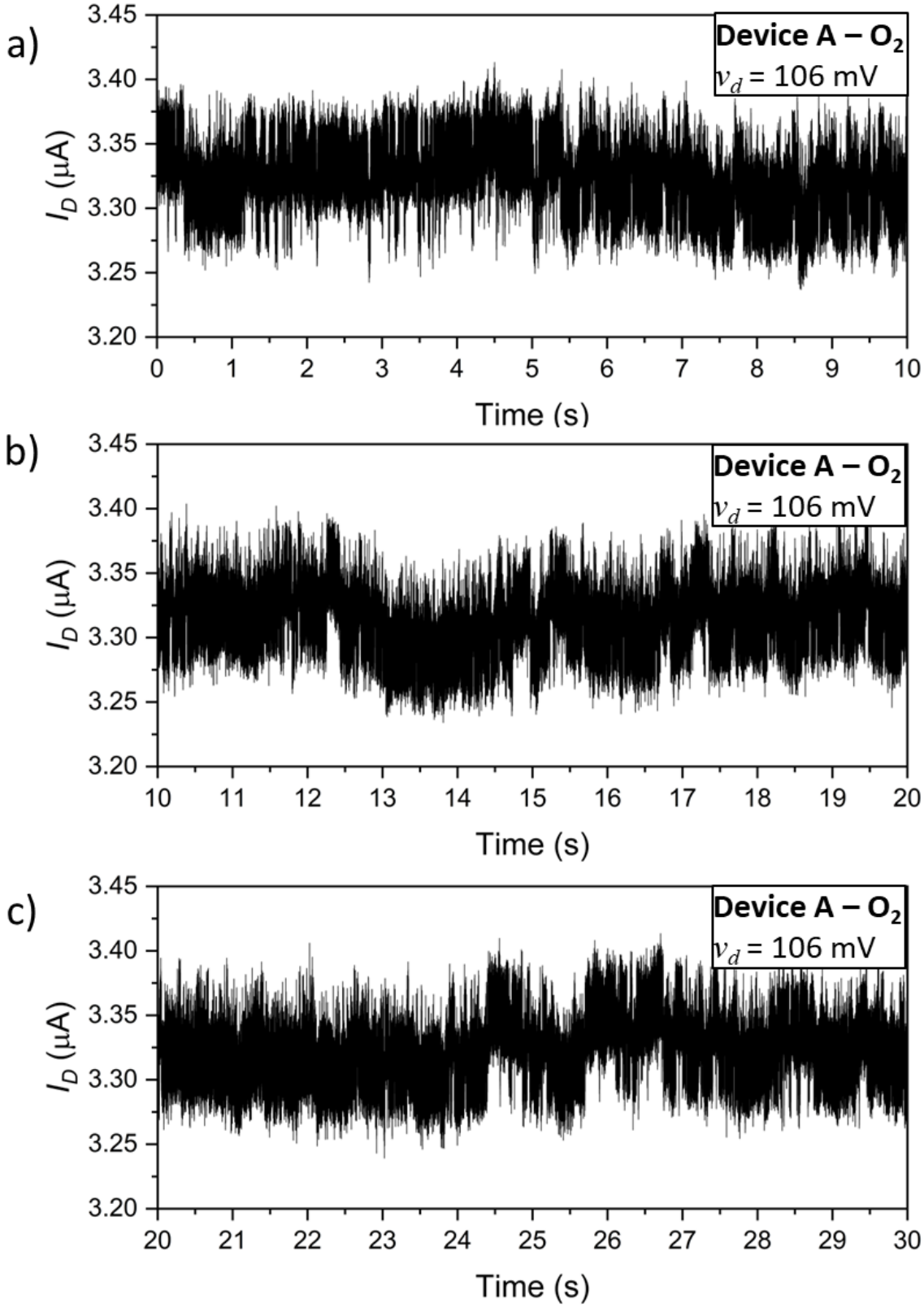

Figure D2 Current of Device A (suspended contact) with Oxygen. Sections from 0 to 10 seconds (a), 10 to 20 seconds (b), and 20 to 30 seconds (c).

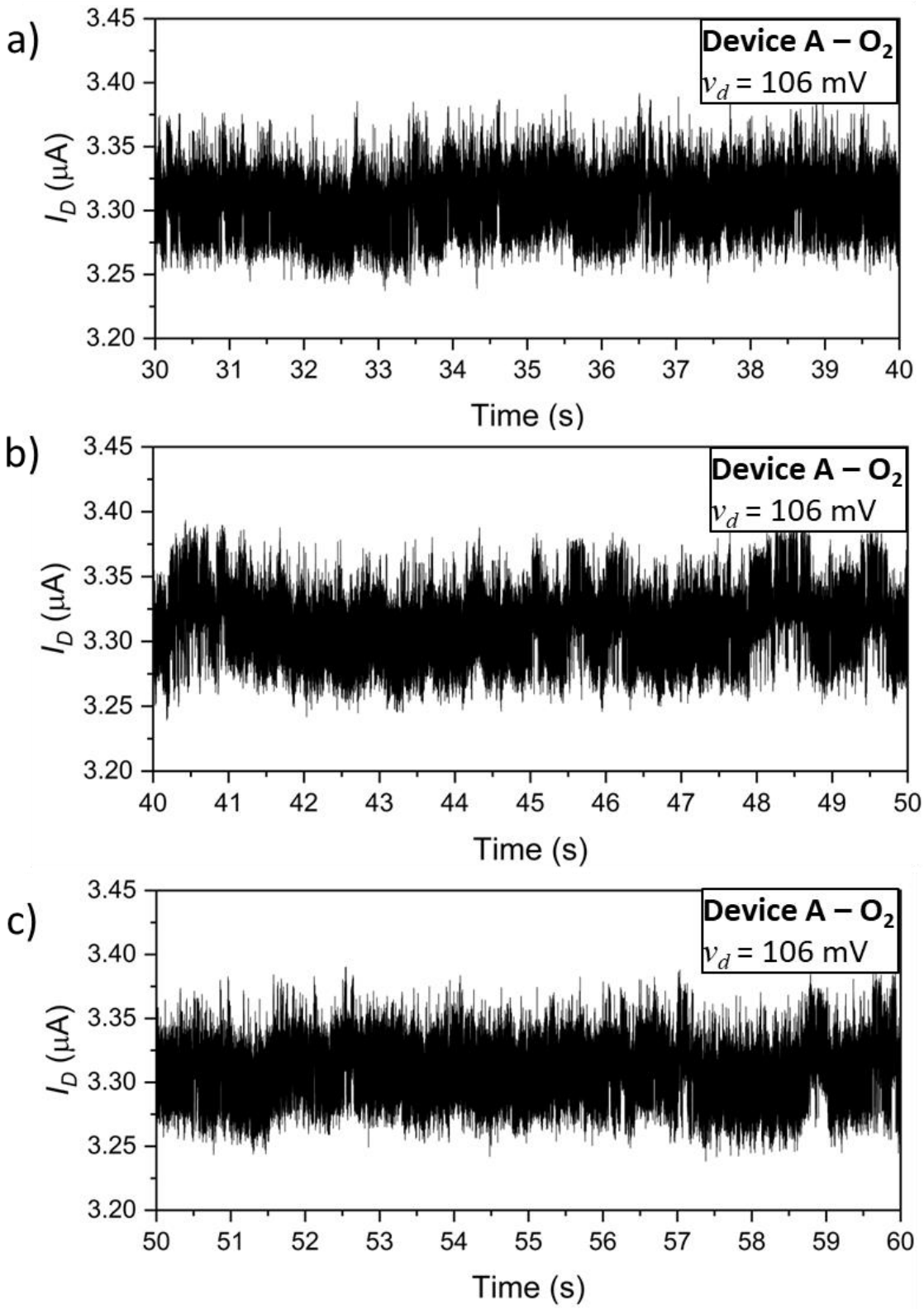

Figure D3 Current of Device A (suspended contact) with Oxygen. Sections from 30 to 40 seconds (a), 40 to 50 seconds (b), and 50 to 60 seconds (c).

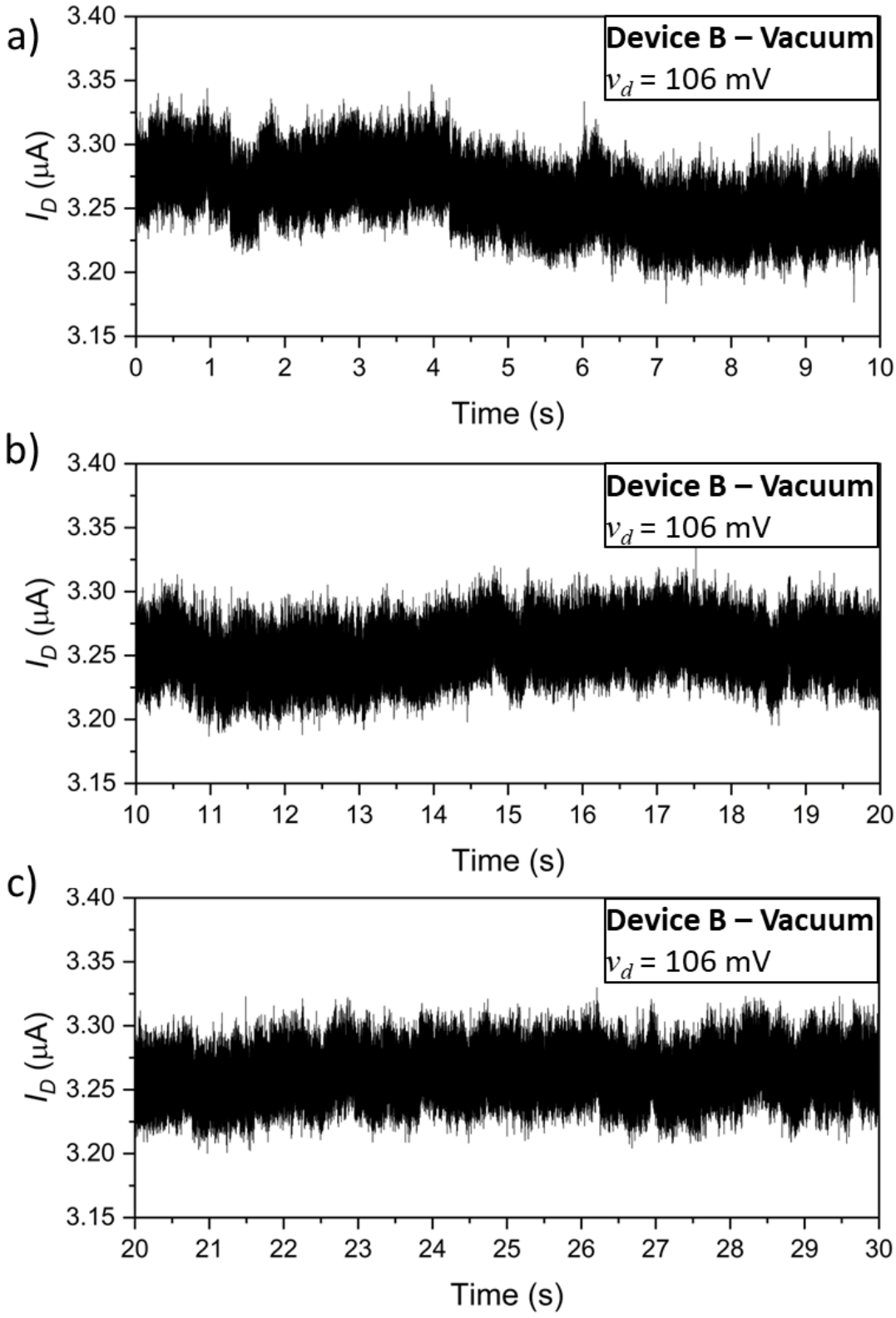

Figure D4 Current of Device B (suspended contact) in a vacuum. Sections from 0 to 10 seconds (a), 10 to 20 seconds (b), and 20 to 30 seconds (c).

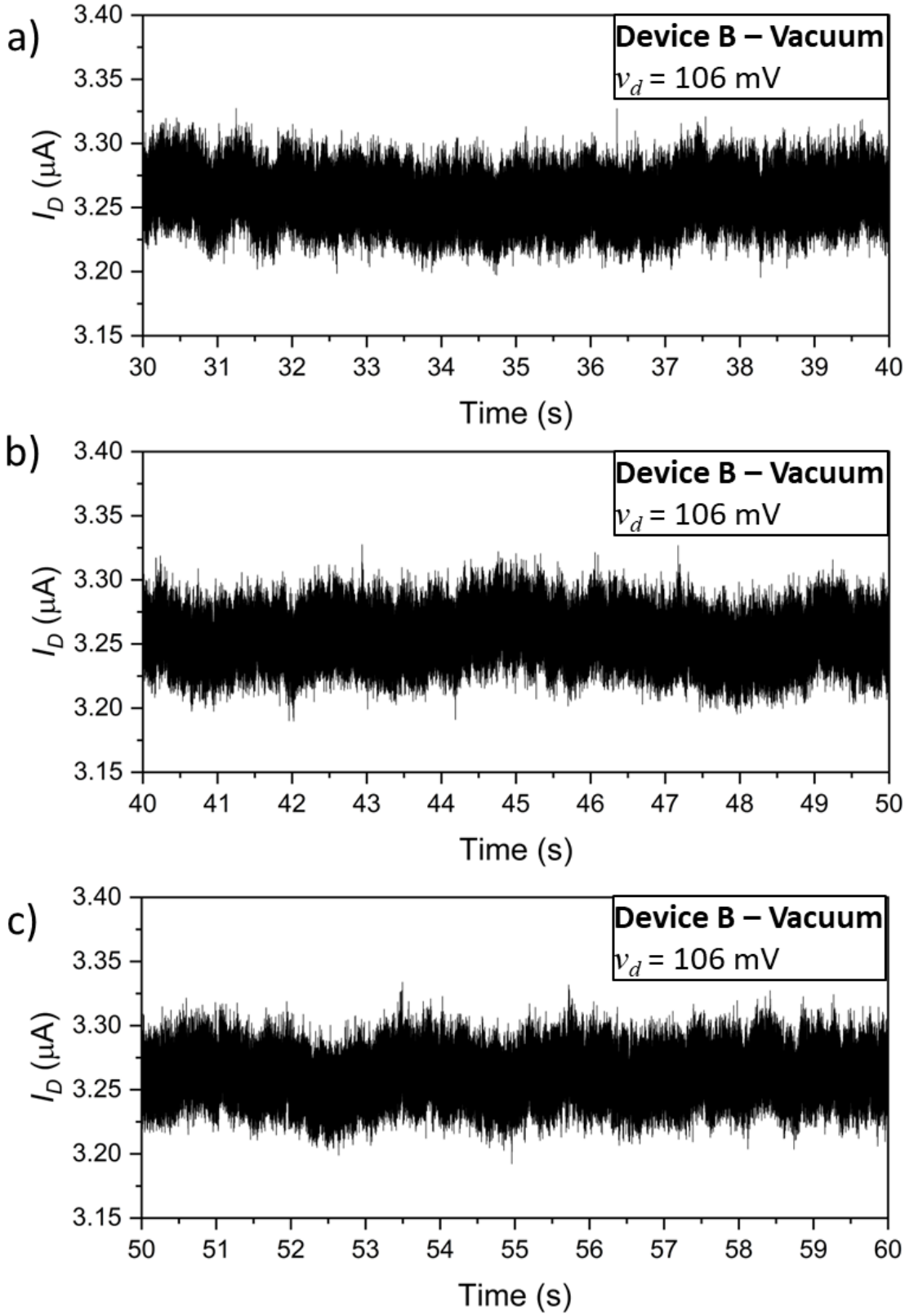

Figure D5 Current of Device B (suspended contact) in a vacuum. Sections from 30 to 40 seconds (a), 40 to 50 seconds (b), and 50 to 60 seconds (c).

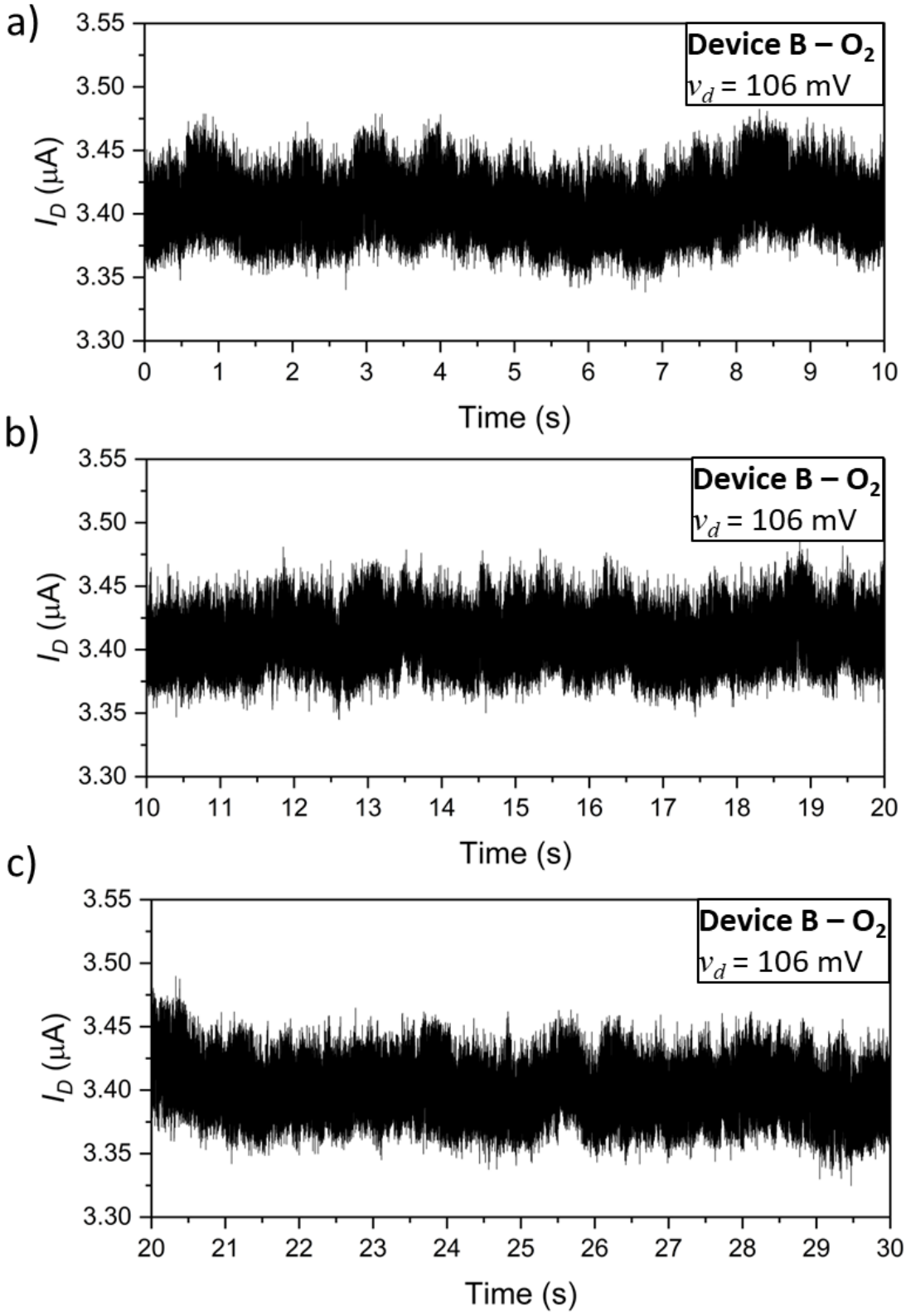

Figure D6 Current of Device B (suspended contact) with oxygen. Sections from 0 to 10 seconds (a), 10 to 20 seconds (b), and 20 to 30 seconds (c).

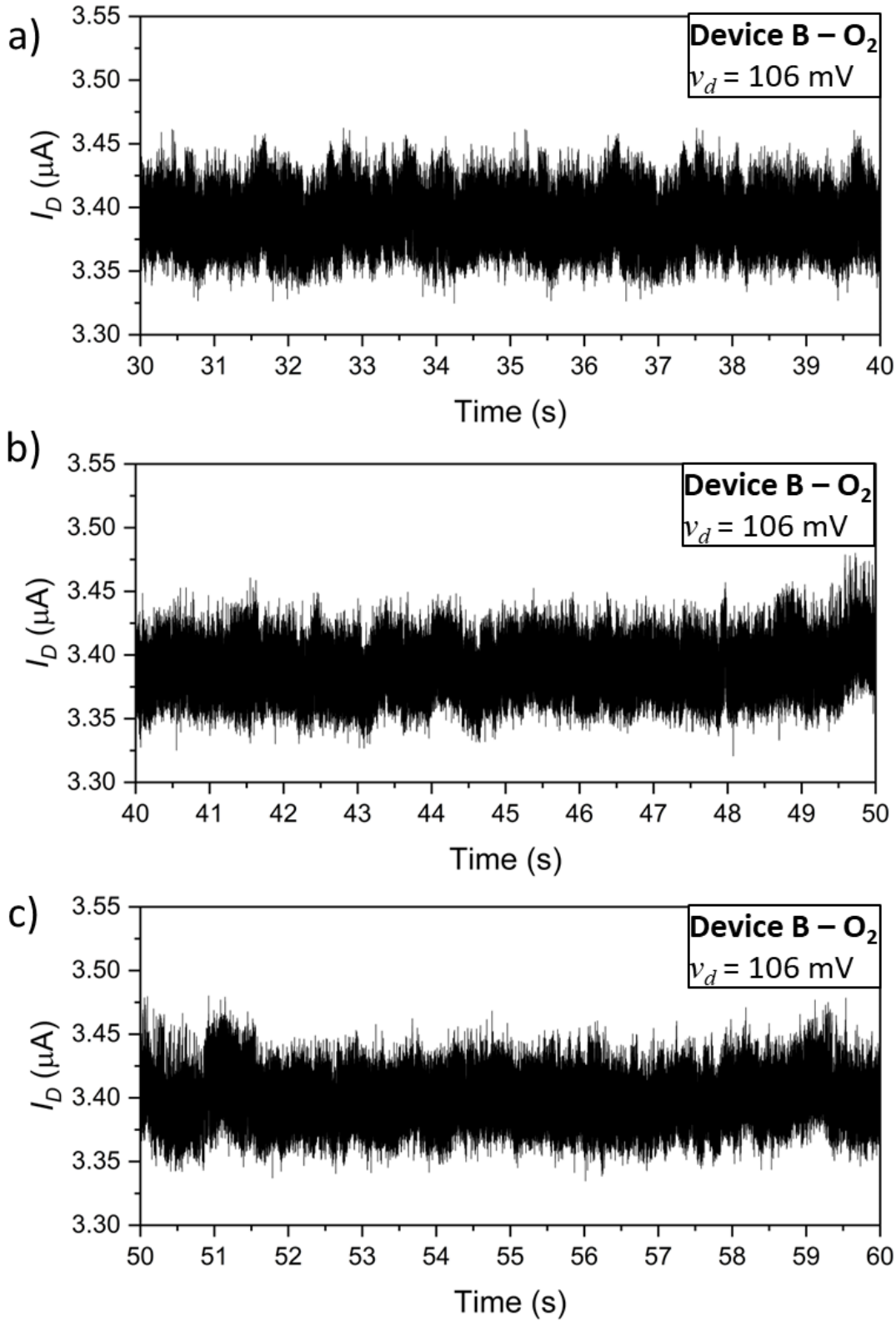

Figure D7 Current of Device B (suspended contact) with oxygen. Sections from 30 to 40 seconds (a), 40 to 50 seconds (b), and 50 to 60 seconds (c).

Appendix E – Detection of Random Telegraph Signal Transitions

To quantitatively analyze the dwell times of each RTS state, it is very important to accurately identify when a transition has occurred. To do so, a cumulative sum (CUMSUM) algorithm was implemented [83]. The algorithm is based on the cumulative sum of the log-likelihood ratio between the two states. The log-likelihood ratio cumulative sum (S_k) is given by the following equation:

$$S_k = \sum_{i=1}^{k} ln\left(\frac{\mathrm{P}_{up}(y_i)}{\mathrm{P}_{down}(y_i)}\right), \tag{D1}$$

where $\mathrm{P}_{up,down}(y_i)$ is the probability that the sample y_i is in the up/down states. If the probability for y_i to be in the high state is smaller than for it to be in the down state, the logarithm term will be negative. Therefore, if the system is in the down state and there is no transition, S_k will have a lower value than its previous value S_{K-1}. During a transition to the up state, the logarithm term will become positive, and $S_k > S_{K-1}$. This way, a transition from down to up state can be detected by comparing the value of S_K to the last minimum value $m_k = \min_{1 \le j \le k} S_j$, and an alarm can be set when the difference between S_k and m_k is larger than a determined threshold (T_{hr}). By increasing T_{hr}, the chance that only real transitions will be detected increases, but with the downside of increasing the delay between the transition and the alarm.

The ratio between P_{up} and P_{down} were calculated from the Gaussian fittings of the histograms obtained from the denoised signals. The fitting was performed with the Software Origin Pro 2022 and the following equation:

$$y = y_{0+\frac{A}{W\sqrt{\frac{\pi}{2}}}} exp\left[-2\left(\frac{x - x_c}{w}\right)^2\right]. \tag{D2}$$

.

The parameters obtained from the fittings are summarized in Table D1.

	Envelope Amplitude Device B Figure 4.9 (b)		Device B Figure 4.10 (a)		Device A Figure 4.11 (a)	
	Down state	**Up state**	**Down State**	**Up state**	**Down State**	**Up state**
y_0 (10^{-5})	-3.0238 ± 18.8981	-3.0238 ± 18.8981	16.6808 ±44.2439	16.6808 ±44.2439	-1.0225 ± 2.64582	-1.0225 ± 2.64582
x_c	165.3426 ± 0.79279	325.1224 ± 2.84669	31057.4097 ± 2.314	31227.8334 ± 1.992	31729.1601 ± 2.43196	32053.4852 ± 0.56734
w	101.7532 ± 1.58241	106.8061 ± 5.92047	117.23569 ± 4.28874	120.12629 ± 3.7545	213.33784 ± 5.06886	207.2782 ± 1.17018
A	4.3820 ± 0.07189	1.3022 ± 0.07574	5.94631 ± 0.23758	7.16173 ± 0.24171	0.7263 ± 0.01871	2.9859 ± 0.01839

Table D1 Parameters obtained from Gaussian fitting.

Figure D1 shows the calculated S_K for an interval of the denoised data of Device A (Chapter 4) with a transition from down to up state. In that case, a threshold of 2500 would result in a delay of 20 μs in the detection.

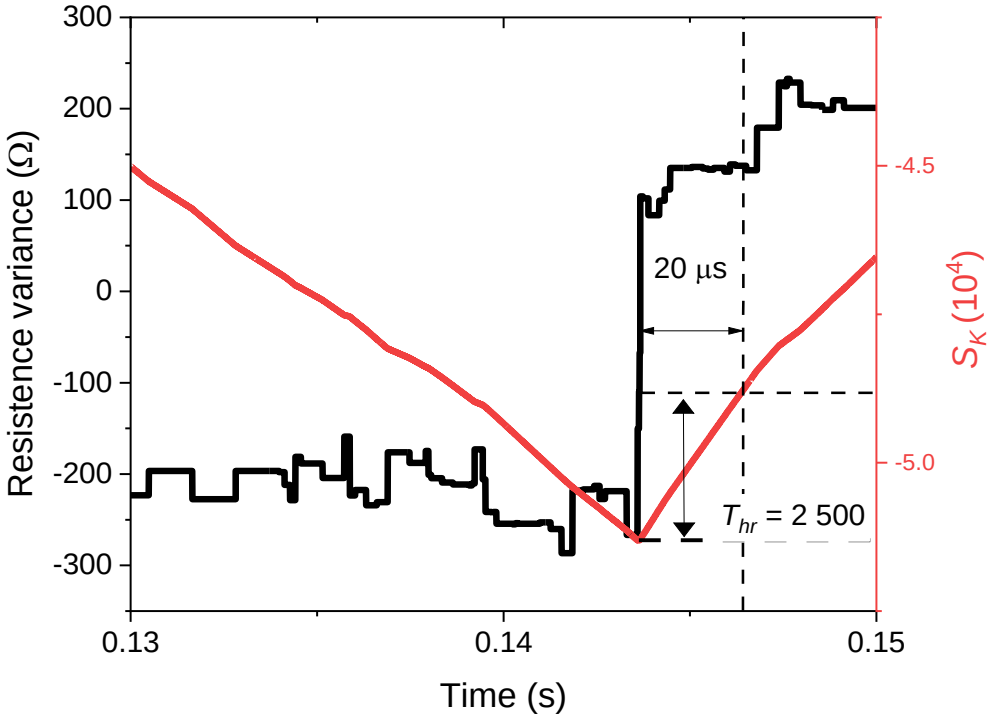

Figure E1 S_k (red line) in a transition from down to up state.

To detect a transition from up to down, one can just invert the probability ratio. The time at which each transition occurred was obtained by applying down-to-up detection, followed by up-to-down detection, and so on (or vice-versa, depending on the initial state of the time series). Higher thresholds result in longer detection delays, which influences the overall transition alarm time, especially if a new transition has occurred before there was time for S_k to go above the threshold, which results in a failure in the capture of a transition, as shown in Figure D2. Because of that, small thresholds between 0 and 100 were used. Also, it was noticed that errors can easily propagate. Because of that and since the entire time series of Device A of Chapter 4 was analyzed (1 minute long), the algorithm was applied in sections of approximately 2 seconds.

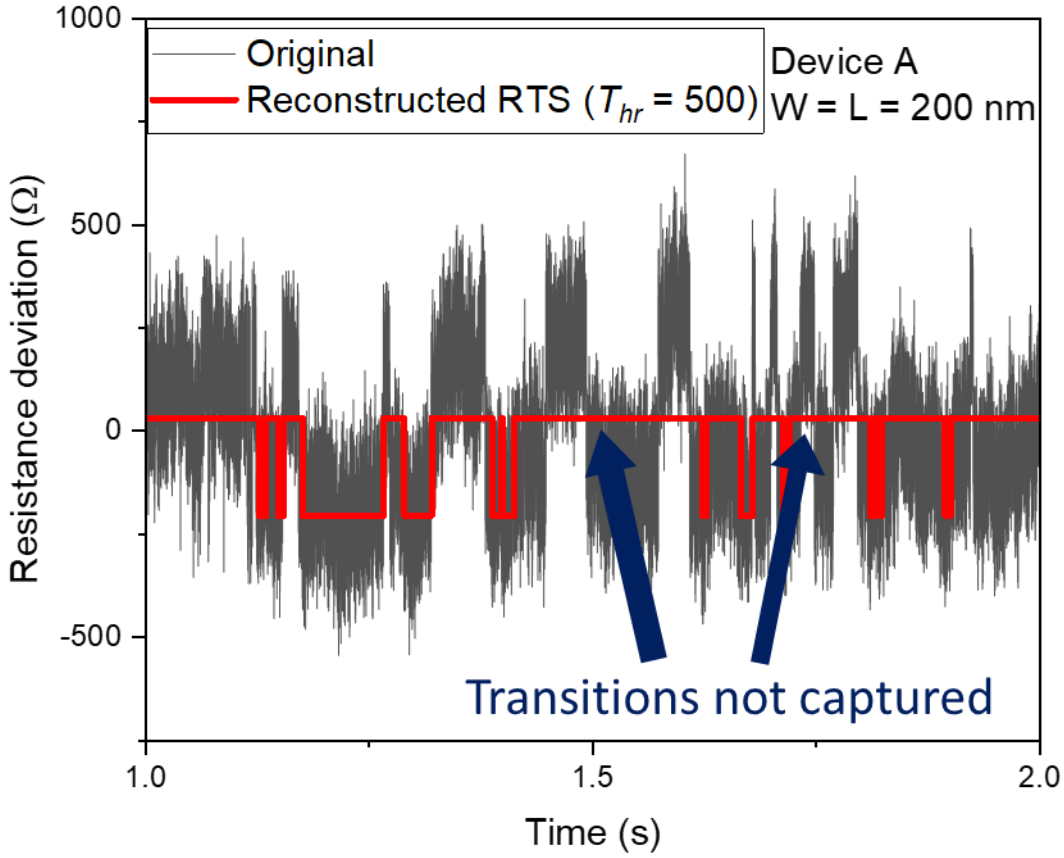

Figure E2 Original time series and the RTS reconstruction based on the CUMSUM algorithm, showing failure in capturing some transitions for T_{hr} = 500.

The MATLAB code used to implement the CUMSUM algorithm is shown below.

```
function [B,SK_1,SK_2] = cumsum_log(state1,state2,RTS_wd,h)
%%%%%%%%%%%%%%%%%%Inputs%%%%%%%%%%%%
% State1 and State 2 is a vector with the gaussian fitting parameters, in
% the following order: State_i = [A_0, W_0, xc_0, y_00], where the gaussian
curve is given by p = abs(y_0 + (A/(W*sqrt(pi/2)))*exp(-2*((RTS_wd-
xc)/W).^2));
% RTS_wd: Signal with RTS
% h: threshold

%%%%% Outputs %%%%%%%%%
% B: vector to shows transitions detections: +1 for down-to-up transitions,
% -1 for up-to-down, and 0 if no transitions was detected.
% SK_1: cummulative log-likelihood sum of transitions down to up
% SK_2: cummulative log-likelihood sum of transitions up to down


%%% First step: Defining P_0 as the down state and p_1 is the up state,
%%% independently of the vectors State1 and state2
L = length(RTS_wd);
if state1(3) < state2(3)
    p_0 = abs(state1(4) + (state1(1)/(state1(2)*sqrt(pi/2)))*exp(-2*((RTS_wd-
state1(3))/state1(2)).^2));
    p_1 = abs(state2(4) + (state2(1)/(state2(2)*sqrt(pi/2)))*exp(-2*((RTS_wd-
state2(3))/state2(2)).^2));
else
    p_1 = abs(state1(4) + (state1(1)/(state1(2)*sqrt(pi/2)))*exp(-2*((RTS_wd-
state1(3))/state1(2)).^2));
    p_0 = abs(state2(4) + (state2(1)/(state1(2)*sqrt(pi/2)))*exp(-2*((RTS_wd-
state2(3))/state2(2)).^2));
end
si_1 = log(p_0./p_1);
si_2 = log(p_1./p_0);

%%start of the computation%%
```

```
l = 1;
if log(p_0(1)/p_1(1)) < 0 %verifying if the RTS starts in the up state.
    while l < L
        k = 2;
        S_K = zeros(1,length(RTS_wd));
        m = zeros(1,length(RTS_wd));
        g(1) = 0;
        m(1) = 0;
        %Detection of up-to-down transitions
        while g(k-1) <= h && k+l <= length(RTS_wd)-10
            S_K(k) = sum(si_1(l:k+l));
            m(k) = min(S_K(1:k));
            g(k) = S_K(k) - m(k);
            k = k+1;
        end
        l = l + k;
        B(l) = -1;
        k = 2;
        S_K = zeros(1,length(RTS_wd));
        m = zeros(1,length(RTS_wd));
        g(1) = 0;
        m(1) = 0;
        %Detection of down-to-up transitions
        while g(k-1) <= h && k+l <= length(RTS_wd)-10
            S_K(k) = sum(si_2(l:k+l));
            m(k) = min(S_K(1:k));
            g(k) = S_K(k) - m(k);
            k = k+1;
        end
        l = l + k;
        B(l) = 1;
    End
% if the RTS starts in the down state:
else
    while l < length(RTS_wd)
        k = 2;
```

```
        S_K = zeros(1,length(RTS_wd));
        m = zeros(1,length(RTS_wd));
        g(1) = 0;
        m(1) = 0;
        %Detection down-to-up transitions
        while g(k-1) <= h && k+l <= length(RTS_wd)-10
            S_K(k) = sum(si_2(l:k+l));
            m(k) = min(S_K(1:k));
            g(k) = S_K(k) - m(k);
            k = k+1;
        end
        l = l + k;
        B(l) = 1;
        k = 2;
        S_K = zeros(1,length(RTS_wd));
        m = zeros(1,length(RTS_wd));
        g(1) = 0;
        m(1) = 0;
        %Detection of up-to-down transitions
        while g(k-1) <= h && k+l <= length(RTS_wd)-10
            S_K(k) = sum(si_1(l:k+l));
            m(k) = min(S_K(1:k));
            g(k) = S_K(k) - m(k);
            k = k+1;
        end
        l = l + k;
        B(l) = -1;
    end
end
SK_1 = cumsum(si_1);
SK_2 = cumsum(si_2);
end
```

Bibliography

[1] W. Miekisch, J. K. Schubert and G. F. E. Noeldge-Schomburg, "Diagnostic potential of breath analysis—focus on volatile organic compounds," *Clinica Chimica Acta,* vol. 347, p. 25–39, September 2004.

[2] Y. Chen, Y. Zhang, F. Pan, J. Liu, K. Wang, C. Zhang, S. Cheng, L. Lu, W. Zhang, Z. Zhang, X. Zhi, Q. Zhang, G. Alfranca, J. M. De La Fuente, D. Chen and D. Cui, "Breath Analysis Based on Surface-Enhanced Raman Scattering Sensors Distinguishes Early and Advanced Gastric Cancer Patients from Healthy Persons," *ACS Nano,* vol. 10, p. 8169–8179, September 2016.

[3] S.-J. Choi, B.-H. Jang, S.-J. Lee, B. K. Min, A. Rothschild and I.-D. Kim, "Selective Detection of Acetone and Hydrogen Sulfide for the Diagnosis of Diabetes and Halitosis Using SnO2 Nanofibers Functionalized with Reduced Graphene Oxide Nanosheets," *ACS Applied Materials & Interfaces,* vol. 6, p. 2588–2597, February 2014.

[4] G. Stavropoulos, K. Van Munster, G. Ferrandino, M. Sauca, C. Ponsioen, F.-J. Van Schooten and A. Smolinska, "Liver Impairment—The Potential Application of Volatile Organic Compounds in Hepatology," *Metabolites,* vol. 11, p. 618, September 2021.

[5] N. T. Brannelly, J. P. Hamilton-Shield and A. J. Killard, "The Measurement of Ammonia in Human Breath and its Potential in Clinical Diagnostics," *Critical Reviews in Analytical Chemistry,* vol. 46, p. 490–501, November 2016.

[6] J. Obermeier, P. Trefz, J. Happ, J. K. Schubert, H. Staude, D.-C. Fischer and W. Miekisch, "Exhaled volatile substances mirror clinical conditions in pediatric chronic kidney disease," *PLOS ONE,* vol. 12, p. e0178745, June 2017.

[7] S. Das and M. Pal, "Review—Non-Invasive Monitoring of Human Health by Exhaled Breath Analysis: A Comprehensive Review," *Journal of The Electrochemical Society,* vol. 167, p. 037562, January 2020.

[8] A. H. Castro Neto, F. Guinea, N. M. R. Peres, K. S. Novoselov and A. K. Geim, "The electronic properties of graphene," *Reviews of Modern Physics,* vol. 81, p. 109–162, January 2009.

[9] K. S. Novoselov, A. K. Geim, S. V. Morozov, D. Jiang, Y. Zhang, S. V. Dubonos, I. V. Grigorieva and A. A. Firsov, "Electric Field Effect in Atomically Thin Carbon

Films," *Science,* vol. 306, p. 666–669, October 2004.

[10] K. M. Tripathi, T. Kim, D. Losic and T. T. Tung, "Recent advances in engineered graphene and composites for detection of volatile organic compounds (VOCs) and non-invasive diseases diagnosis," *Carbon,* vol. 110, p. 97–129, December 2016.

[11] F. Schedin, A. K. Geim, S. V. Morozov, E. W. Hill, P. Blake, M. I. Katsnelson and K. S. Novoselov, "Detection of individual gas molecules adsorbed on graphene," *Nature Materials,* vol. 6, p. 652–655, September 2007.

[12] J. Sun, M. Muruganathan and H. Mizuta, "Room temperature detection of individual molecular physisorption using suspended bilayer graphene," *Science Advances,* vol. 2, p. e1501518, April 2016.

[13] A. W. Boots, J. J. B. N. Van Berkel, J. W. Dallinga, A. Smolinska, E. F. Wouters and F. J. Van Schooten, "The versatile use of exhaled volatile organic compounds in human health and disease," *Journal of Breath Research,* vol. 6, p. 027108, June 2012.

[14] T. Liu, L. Guo, M. Wang, C. Su, D. Wang, H. Dong, J. Chen and W. Wu, "Review on Algorithm Design in Electronic Noses: Challenges, Status, and Trends," *Intelligent Computing,* vol. 2, p. 0012, January 2023.

[15] L. T. Hoa, H. N. Tien, V. H. Luan, J. S. Chung and S. H. Hur, "Fabrication of a novel 2D-graphene/2D-NiO nanosheet-based hybrid nanostructure and its use in highly sensitive NO_2 sensors," *Sensors and Actuators B: Chemical,* vol. 185, p. 701–705, August 2013.

[16] O. G. Agbonlahor, M. Muruganathan, S. G. Ramaraj, Z. Wang, A. M. M. Hammam, A. Kareekunnan, H. Maki, M. Hattori, K. Shimomai and H. Mizuta, "Interfacial Ammonia Selectivity, Atmospheric Passivation, and Molecular Identification in Graphene-Nanopored Activated Carbon Molecular-Sieve Gas Sensors" *ACS Appl. Mater. Interfaces,* vol. 13, p. 61770–61779, December 2021.

[17] S. G. Ramaraj, M. Muruganathan, O. G. Agbonlahor, H. Maki, Y. Onda, M. Hattori and H. Mizuta, "Carbon molecular sieve-functionalized graphene sensors for highly sensitive detection of ethanol," *Carbon,* vol. 190, p. 359–365, April 2022.

[18] S. Liang, J. Zhu, J. Ding, H. Bi, P. Yao, Q. Han and X. Wang, "Deposition of cocoon-like ZnO on graphene sheets for improving gas-sensing properties to ethanol," *Applied Surface Science,* vol. 357, p. 1593–1600, December 2015.

[19] T. N. Ly and S. Park, "Highly sensitive ammonia sensor for diagnostic purpose using reduced graphene oxide and conductive polymer," *Scientific Reports,* vol. 8,

p. 18030, December 2018.

[20] Y. Seekaew, D. Phokharatkul, A. Wisitsoraat and C. Wongchoosuk, "Highly sensitive and selective room-temperature NO_2 gas sensor based on bilayer transferred chemical vapor deposited graphene," *Applied Surface Science,* vol. 404, p. 357–363, May 2017.

[21] J. Sun, X. Shu, Y. Tian, Z. Tong, S. Bai, R. Luo, D. Li and C. C. Liu, "Facile preparation of polypyrrole-reduced graphene oxide hybrid for enhancing NH_3 sensing at room temperature," *Sensors and Actuators B: Chemical,* vol. 241, p. 658–664, March 2017.

[22] A. Mirzaei, S. P. Bharath, J.-Y. Kim, K. K. Pawar, H. W. Kim and S. S. Kim, "N-Doped Graphene and Its Derivatives as Resistive Gas Sensors: An Overview," *Chemosensors,* vol. 11, p. 334, June 2023.

[23] A. Lipatov, A. Varezhnikov, P. Wilson, V. Sysoev, A. Kolmakov and A. Sinitskii, "Highly selective gas sensor arrays based on thermally reduced graphene oxide," *Nanoscale,* vol. 5, p. 5426, 2013.

[24] Y.-S. Chang, F.-K. Chen, D.-C. Tsai, B.-H. Kuo and F.-S. Shieu, "N-doped reduced graphene oxide for room-temperature NO gas sensors," *Scientific Reports,* vol. 11, p. 20719, October 2021.

[25] L. B. Kish, R. Vajtai and C. G. Granqvist, "Extracting information from noise spectra of chemical sensors: single sensor electronic noses and tongues," *Sensors and Actuators B: Chemical,* vol. 71, p. 55–59, November 2000.

[26] S. Rumyantsev, G. Liu, M. S. Shur, R. A. Potyrailo and A. A. Balandin, "Selective Gas Sensing with a Single Pristine Graphene Transistor," *Nano Letters,* vol. 12, p. 2294–2298, May 2012.

[27] A. Setiadi, H. Fujii, S. Kasai, K.-i. Yamashita, T. Ogawa, T. Ikuta, Y. Kanai, K. Matsumoto, Y. Kuwahara and M. Akai-Kasaya, "Room-temperature discrete-charge-fluctuation dynamics of a single molecule adsorbed on a carbon nanotube," *Nanoscale,* vol. 9, p. 10674–10683, 2017.

[28] Z. Cheng, Q. Li, Z. Li, Q. Zhou and Y. Fang, "Suspended Graphene Sensors with Improved Signal and Reduced Noise," *Nano Letters,* vol. 10, p. 1864–1868, May 2010.

[29] A. Ghosh, S. Kar, A. Bid and A. K. Raychaudhuri, "A set-up for measurement of low frequency conductance fluctuation (noise) using digital signal processing techniques," 2004.

[30] J. H. Scofield, "ac method for measuring low-frequency resistance fluctuation spectra," *Review of Scientific Instruments,* vol. 58, p. 985–993, June 1987.

[31] P. R. Wallace, "The Band Theory of Graphite," *Physical Review,* vol. 71, p. 622–634, May 1947.

[32] A. Jorio, R. Saito, G. Dresselhaus and M. S. Dresselhaus, Raman Spectroscopy in Graphene Related Systems, 1 ed., Wiley, 2011.

[33] S. Kim, J. Nah, I. Jo, D. Shahrjerdi, L. Colombo, Z. Yao, E. Tutuc and S. K. Banerjee, "Realization of a high mobility dual-gated graphene field-effect transistor with Al_2O_3 dielectric," *Applied Physics Letters,* vol. 94, p. 062107, February 2009.

[34] G. Ko, H.-Y. Kim, J. Ahn, Y.-M. Park, K.-Y. Lee and J. Kim, "Graphene-based nitrogen dioxide gas sensors," *Current Applied Physics,* vol. 10, p. 1002–1004, July 2010.

[35] C. Melios, A. Centeno, A. Zurutuza, V. Panchal, C. E. Giusca, S. Spencer, S. R. P. Silva and O. Kazakova, "Effects of humidity on the electronic properties of graphene prepared by chemical vapour deposition," *Carbon,* vol. 103, p. 273–280, July 2016.

[36] E. Ji, M. J. Kim, J.-Y. Lee, D. Sung, N. Kim, J.-W. Park, S. Hong and G.-H. Lee, "Substrate effect on doping and degradation of graphene," *Carbon,* vol. 184, p. 651–658, October 2021.

[37] M. Muruganathan, J. Sun, T. Imamura and H. Mizuta, "Electrically Tunable van der Waals Interaction in Graphene–Molecule Complex," *Nano Letters,* vol. 15, p. 8176–8180, November 2015.

[38] C. Wang, Y. Wang, Z. Yang and N. Hu, "Review of recent progress on graphene-based composite gas sensors," *Ceramics International,* vol. 47, p. 16367–16384, June 2021.

[39] O. G. Agbonlahor, M. Muruganathan, A. Banerjee and H. Mizuta, "Machine Learning Identification of Atmospheric Gases by Mapping the Graphene-Molecule Van Der Waals Complex Bonding Evolution," *SSRN Electronic Journal,* 2022.

[40] A. Papoulis and S. U. Pillai, Probability, random variables, and stochastic processes, 4th ed ed., Boston: McGraw-Hill, 2002.

[41] R. M. Howard, Principles of Random Signal Analysis and Low Noise Design, Wiley, 2002.

[42] R. Mancini, Op amps for everyone: design reference, 2nd ed ed., Amsterdam Boston: Newnes, 2003.

[43] P. J. Fish, Electronic Noise and Low Noise Design, Macmillan Education UK, 1993.

[44] J. B. Johnson, "Thermal Agitation of Electricity in Conductors," *Physical Review,* vol. 32, p. 97–109, July 1928.

[45] H. Nyquist, "Thermal Agitation of Electric Charge in Conductors," *Physical Review,* vol. 32, p. 110–113, July 1928.

[46] D. Wolf, "1/*f*-Noise," in *Noise in Physical Systems*, Springer Berlin Heidelberg, 1978, p. 122–133.

[47] F. N. Hooge, T. G. M. Kleinpenning and L. K. J. Vandamme, "Experimental studies on 1/*f* noise," *Reports on Progress in Physics,* vol. 44, p. 479–532, May 1981.

[48] A. L. McWhorter, "1/*f* Noise and Related Surface Effects," Massachusetts Institute of Technology, Cambridge, 1955.

[49] N. V. Amarasinghe, Z. Çelik-Butler and P. Vasina, "Characterization of oxide traps in 0.15 μm^2 MOSFETs using random telegraph signals," *Microelectronics Reliability,* vol. 40, p. 1875–1881, November 2000.

[50] K. K. Hung, P. K. Ko, C. Hu and Y. C. Cheng, "Random telegraph noise of deep-submicrometer MOSFETs," *IEEE Electron Device Letters,* vol. 11, p. 90–92, February 1990.

[51] M. J. Kirton and M. J. Uren, "Noise in solid-state microstructures: A new perspective on individual defects, interface states and low-frequency (1/*f*) noise," *Advances in Physics,* vol. 38, p. 367–468, January 1989.

[52] S. Kogan, Electronic Noise and Fluctuations in Solids, Cambridge University Press, 1996.

[53] Y.-M. Lin and P. Avouris, "Strong Suppression of Electrical Noise in Bilayer Graphene Nanodevices," *Nano Letters,* vol. 8, p. 2119–2125, August 2008.

[54] Z. Chen, Y.-M. Lin, M. J. Rooks and P. Avouris, "Graphene nano-ribbon electronics," *Physica E: Low-dimensional Systems and Nanostructures,* vol. 40, p. 228–232, December 2007.

[55] P. Dutta and P. M. Horn, "Low-frequency fluctuations in solids: 1/*f* noise," *Reviews of Modern Physics,* vol. 53, p. 497–516, July 1981.

[56] A. A. Balandin, "Low-frequency 1/f noise in graphene devices," *Nature Nanotechnology,* vol. 8, p. 549–555, August 2013.

[57] G. Liu, W. Stillman, S. Rumyantsev, Q. Shao, M. Shur and A. A. Balandin, "Low-frequency electronic noise in the double-gate single-layer graphene transistors," *Applied Physics Letters,* vol. 95, p. 033103, July 2009.

[58] G. Xu, C. M. Torres, Y. Zhang, F. Liu, E. B. Song, M. Wang, Y. Zhou, C. Zeng and K. L. Wang, "Effect of Spatial Charge Inhomogeneity on 1/*f* Noise Behavior in Graphene," *Nano Letters,* vol. 10, p. 3312–3317, September 2010.

[59] I. Heller, S. Chatoor, J. Männik, M. A. G. Zevenbergen, J. B. Oostinga, A. F. Morpurgo, C. Dekker and S. G. Lemay, "Charge Noise in Graphene Transistors," *Nano Letters,* vol. 10, p. 1563–1567, May 2010.

[60] N. Mavredakis, R. Garcia Cortadella, A. Bonaccini Calia, J. A. Garrido and D. Jiménez, "Understanding the bias dependence of low frequency noise in single layer graphene FETs," *Nanoscale,* vol. 10, p. 14947–14956, 2018.

[61] M. Kamada, W. Zeng, A. Laitinen, J. Sarkar, S.-S. Yeh, K. Tappura, H. Seppä and P. Hakonen, "Suppression of 1/*f* noise in graphene due to anisotropic mobility fluctuations induced by impurity motion," *Communications Physics,* vol. 6, p. 207, August 2023.

[62] A. Rehman, J. A. D. Notario, J. S. Sanchez, Y. M. Meziani, G. Cywiński, W. Knap, A. A. Balandin, M. Levinshtein and S. Rumyantsev, "Nature of the 1/*f* noise in graphene—direct evidence for the mobility fluctuation mechanism," *Nanoscale,* vol. 14, p. 7242–7249, May 2022.

[63] M. Kamada, A. Laitinen, W. Zeng, M. Will, J. Sarkar, K. Tappura, H. Seppä and P. Hakonen, "Electrical Low-Frequency 1/f^{γ} Noise Due to Surface Diffusion of Scatterers on an Ultra-low-Noise Graphene Platform," *Nano Letters,* vol. 21, p. 7637–7643, September 2021.

[64] K. R. Amin and A. Bid, "High-Performance Sensors Based on Resistance Fluctuations of Single-Layer-Graphene Transistors," *ACS Applied Materials & Interfaces,* vol. 7, p. 19825–19830, September 2015.

[65] E. Stolyarova, D. Stolyarov, K. Bolotin, S. Ryu, L. Liu, K. T. Rim, M. Klima, M. Hybertsen, I. Pogorelsky, I. Pavlishin, K. Kusche, J. Hone, P. Kim, H. L. Stormer, V. Yakimenko and G. Flynn, "Observation of Graphene Bubbles and Effective Mass Transport under Graphene Films," *Nano Letters,* vol. 9, p. 332–337, January 2009.

[66] A. V. Oppenheim and R. W. Schafer, Digital signal processing, Englewood Cliffs, N.J: Prentice-Hall, 1975.

[67] P. Welch, "The use of fast Fourier transform for the estimation of power spectra: A method based on time averaging over short, modified periodograms," *IEEE Transactions on Audio and Electroacoustics,* vol. 15, p. 70–73, June 1967.

[68] Z. H. Ni, H. M. Wang, Z. Q. Luo, Y. Y. Wang, T. Yu, Y. H. Wu and Z. X. Shen, "The

effect of vacuum annealing on graphene: The effect of vacuum annealing on graphene," *Journal of Raman Spectroscopy,* vol. 41, p. 479–483, May 2010.

[69] H. Wang, Y. Wu, C. Cong, J. Shang and T. Yu, "Hysteresis of Electronic Transport in Graphene Transistors," *ACS Nano,* vol. 4, p. 7221–7228, December 2010.

[70] C. Liu, J. Zhang, S. G. Ramaraj, X. Zhang, M. Muruganathan, H. Mizuta and Y. Oshima, "Current effect on suspended graphene nanoribbon studied using in–situ transmission electron microscopy," *Applied Surface Science,* vol. 573, p. 151563, January 2022.

[71] H. E. Romero, N. Shen, P. Joshi, H. R. Gutierrez, S. A. Tadigadapa, J. O. Sofo and P. C. Eklund, "n-Type Behavior of Graphene Supported on Si/SiO_2 Substrates," *ACS Nano,* vol. 2, p. 2037–2044, September 2008.

[72] S. Guo, R. Wang, D. Mao, Y. Wang and R. Huang, "Anomalous random telegraph noise in nanoscale transistors as direct evidence of two metastable states of oxide traps," *Scientific Reports,* vol. 7, July 2017.

[73] M. J. Uren, M. J. Kirton and S. Collins, "Anomalous telegraph noise in small-area silicon metal-oxide-semiconductor field-effect transistors," *Physical Review B,* vol. 37, p. 8346–8350, May 1988.

[74] S. M. Sze and M. K. Lee, Semiconductor devices, physics and technology, 3rd ed ed., Hoboken, N.J: Wiley, 2012.

[75] M. Zahidul Islam, H. Maki, M. Muruganathan, K. Afsal, S. Enomoto, Y. Onda, M. Hattori and H. Mizuta, "Tin nanoparticles functionalized graphene sensors for ethanol gas sensing," in *The 9th International Symposium on Organic and Inorganic Electronic Materials and Related Nanotechnology (EM-NANO)*, Kanazawa, 2023.

[76] J. M. Carlsson, F. Hanke, S. Linic and M. Scheffler, "Two-Step Mechanism for Low-Temperature Oxidation of Vacancies in Graphene," *Physical Review Letters,* vol. 102, p. 166104, April 2009.

[77] F. Mehmood, R. Pachter, W. Lu and J. J. Boeckl, "Adsorption and Diffusion of Oxygen on Single-Layer Graphene with Topological Defects," *The Journal of Physical Chemistry C,* vol. 117, p. 10366–10374, May 2013.

[78] X. Qi, X. Guo and C. Zheng, "Density functional study the interaction of oxygen molecule with defect sites of graphene," *Applied Surface Science,* vol. 259, p. 195–200, October 2012.

[79] Advances in spectrum analysis and array processing. 3, Englewood, Cliffs: Prentice Hall, 1995.

[80] Y. T. Chan, Wavelet Basics, Boston, MA: Springer US, 1995.

[81] M. J. Shensa, "The discrete wavelet transform: wedding the a trous and Mallat algorithms," *IEEE Transactions on Signal Processing,* vol. 40, p. 2464–2482, October 1992.

[82] M. Misiti, Y. Misiti, G. Oppenheim and J. Poggi, Eds., Wavelets and their Applications, 1 ed., Wiley, 2007.

[83] M. Basseville and I. V. Nikiforov, Detection of abrupt changes: theory and application, Englewood Cliffs, N.J: Prentice Hall, 1993.